4th of July, 2014

MASTER THESIS

A PLUG BASED MICRO SOLID PHASE EXTRACTION (μSPE) MICROFLUIDIC CHIP FOR THE ISOLATION AND PURIFICATION OF DNA

ing. H.W. (Henk-Willem) Veltkamp

Faculty of Science and Technology (TNW, Technische Natuurwetenschappen)
Mesoscale Chemical Systems (MCS)

Exam committee:
Prof. dr. J.G.E. (Han) Gardeniers
Dr. ir. R. (Roald) Tiggelaar
Dr. ir. S. (Séverine) Le Gac
M.C. (Matthijs) Zuidberg M.Sc.

UNIVERSITY OF TWENTE.

"DNA TECHNOLOGY COULD BE THE GREATEST SINGLE ADVANCE IN THE SEARCH FOR TRUTH,
CONVICTION OF THE GUILTY,
AND AQUITTAL OF THE INNOCENT SINCE THE ADVENT OF CROSS-EXAMINATION."

Judge Joseph Harris
in People vs Wesley
140 Misc. 2d 306, 533 N.Y.S. 2d 643 (Co. Ct. 1988)
Quoted by Lorne T. Kirby in "DNA Fingerprinting- An introduction" (Stockton Press), 1990

Voor papa, mama, Teun-Christian, en Linda

Abstract

This Master's thesis describes the research that is done for the development of a plug-based microfluidic DNA extraction chip. The investigated method relies on a micro solid phase extraction method that is based on the electrostatic interaction between protonated amino groups and the negatively charged DNA.

Chapter 1 starts with a global introduction into the field of microfluidics and based on this introduction it will point out the importance of the research question. From the point of this research question, a literature study is performed and the results of how the state-of-the-art nowadays is, is given. There are three main approaches: beads-filled columns, monolithic columns, and one-piece columns. Each of these approaches is discussed and examples are given. Based on this literature study, an approach for this thesis is developed.

Chapter 2 is the more theoretical orientated chapter with useful and relevant information. It starts with the theory behind the chip layout and design aspects. After that, a mathematical description of the velocity profile inside the chip is given and the use and importance of a finite element methods based software package for computational fluid dynamics research are described. The velocity profile equation is derived from the well-known Navier-Stokes equations and all the important assumptions are explained. This paragraph is followed with an introduction into the field of emulsions and surfactants, which are important in droplet/plug systems. Then, a paragraph about DNA detection is given. This final paragraph gives a method of detecting low concentrations of DNA with high linearity. This method uses a specially composed high sensitivity assay kit for dsDNA and shows much better results than measuring the concentration with conventional fluorescence measurements.

Chapter 3 shows the main method that is designed for this thesis research. It starts with a global overview of the clean room work (a detailled process flow can be found in appendix C). The next step is the functionalization of the chip, and therefore, this method is also given. The extraction can be performed once the functionalization is done, but it also needs to be analysed. The methods of extraction and analysis are described in the third and fifth paragraph of this chapter. The fourth paragraph is dedicated to the connection between the micro world and the macro universe.

Chapter 4 gives all the results and the discussion of these result, which are collected during this thesis research. As can be seen here, not every result is as expected as was thought on beforehand. The fabrication of the chips and the functionalization of test substrates was without significant problems, but the functionalization of the chip was troublesome. Pumping normal aqueous solutions into the chip can be done, because of the low viscosities. Mineral oil on the other hand has a higher viscosity and therefore it was not possible to pump it into the chip. The high viscosity created a too high pressure drop. The chip is also very sensitive for particle contamination. Effort is put into finding a way of doing the functionalization and extraction without getting the channels clogged with contamination. However, these attempts were not successful. This, and all other findings are presented in the fourth chapter.

Chapter 5 gives the conclusion of this research. The chosen method has proven to be unsuccessful. This is mainly due to the chosen design. The fabrication and extraction tests on the other hand showed promising results.

Chapter 6 lists the recommendations that have the potential to improve the results of this research. This list contains fabrication improvements, recommended characterization steps and a promising method for channel cleaning and activation. This method used a single phase corona discharge plasma, which is guided into a microfluidic channel via an electrode at the end of the channel. Oxygen plasma is one of the better methods for the activation of a native oxide surface, as is shown in the results. However, this method can only be used if the device is completely made out of silica.

Keywords: DNA extraction, μSPE, lab-on-a-chip, microfabrication, forensics

Preface

Last academic year was the climax of my Master's degree, namely the Master's thesis. About 15 months ago I started looking for a research group where I wanted to do my thesis research. That group was found quite quickly. Already two years back I sort of decided that I wanted to do my Master's thesis research in the Mesoscale Chemical Systems research group of the MESA$^+$ Institute for Nanotechnology, after doing my University of Applied Sciences internship there. After discussing some possible topics I have chosen for the forensic/DNA related topic.

During my Master's thesis, I learned a lot. The field of forensics and DNA related analysis was new for me, so it was a real challenge to learn the basics of it in the shortest period of time possible. But once this was done, I had a good basis to work with. The literature study learned me a lot about the different on-chip extraction methods used for DNA extraction. During the design part of this thesis research, I learned to work with both COMSOL MultiPhysics and CleWin 5 mask designing software. The practical work can be divided into two parts, the clean room work and the work that is done in the chemical lab of the Mesoscale Chemical Systems research group. During the clean room work, I followed as much clean room courses as possible. This resulted in a skill set with almost every important step inside the MESA$^+$ clean room. This skill set is very valuable in my future career. A complete overview of all the followed courses can be found in appendix L. During the practical work in the chemical lab, I also helped to move our chemical lab from the Meander building to the Carré building. This change of labs was necessary because of the shortage of space due to new group members. This learned me a lot about safety in the lab and chemical waste disposal.

Now, I have almost finished my Master completely and I am looking back on a wonderful time. This wonderful time resulted in the now following thesis and I hope that you will have as much fun as I had writing it.

ing. Henk-Willem Veltkamp
Enschede, 30-Jun-2014

Contents

List of Figures

List of Tables

Abbreviations

General

Abbreviation	Description
μSPE	micro solid phase extraction
μTAS	micro total analysis system
ARCA	advancing and reducing contact angle
BC	boundary condition
BF	borofloat
bioMEMS	biological microelectromechanical system
BMP	bacterial magnetic particle
CFD	computational fluid dynamics
DRIE	deep reactive ion etching
DSP	dubble side polished
FEM	Finite element method
HS	high sensitivity
I.D.	inner diameter
LHS	left hand side
LoC	lab-on-a-chip
NFI	Nederlands Forensisch Instituut
NS	Navier-Stokes
O.D.	outer diameter
PCR	polymerase chain reaction
RIE	reactive ion etching
RHS	right hand side
SA-V	surface-area-to-volume
SAM	self assembled monolayer
SEM	scanning electron microscope
STR	short tandem repeat
UV	ultra violet
XPS	X-ray photoelectron spectroscopy

Chemicals

Abbreviation	Description
AEEA	3-[2-(-aminoethylamino)- ethylamino]-propyltrimethoxysilane
Al_2O_3	alumina
AMPA	aminomethylphosphonic acid
APTES	3-aminopropyltriethoxysilane
COC	cyclic olefin copolymer
DI	deionized water
DMSO	dimethyl sulfoxide
dsDNA	double stranded deoxyribonucleic acid
GPTMS	(3-glycidoxypropyl)methyldiethoxysilane
H_2O_2	hydrogen peroxide
H_2SO_4	sulphuric acid
HNO_3	nitric acid
OH	hydroxyl
MES	2-(N-morpholino)ethanesulfonic acid
NH_4OH	ammonium hydroxide

Abbreviation	Description
O/W	oil in water
PANAM	poly-amidoamine
PC	polycarbonate
PCI	phenol/chloroform/isoamyl alcohol
PDMS	polydimethylsiloxane
PEEK	polyether ether ketone
PETG	polyethylene terephthalate
PMMA	poly(methylmethacrylate)
PS	polystyrene
PTFE	polytetrafluoroethylene
RNA	ribonucleic acid
Si	silicon
TEOS	tetraethyl orthosilicate
TMOS	tetramethyl orthosilicate
TRIS	tris(hydroxymethyl)methylamine hydrochloride
W/O	water in oil

Symbols

General

Symbol	Description
$[DNA]_{initial}$	initial DNA concentration in sample
A	area
A_{ch}	channel area
A_p	pillar area
Bo	Bond number
Ca	capillary number
D_H	hydraulic diameter
E	electrical field
Eo	Eötvös number
$\overrightarrow{\boldsymbol{f}}$	other body forces vector
g	gravity factor
h	height
$\overrightarrow{\boldsymbol{g}}$	gravity vector
L	length
L_H	hydrodynamic entrance length
n	integer
P_w	wetted perimeter
p	pressure
QF_{value}	value given by the Qubit fluorometer
Re	Reynold's number
Re_{cell}	local Reynold's number of a FEM cell
V	volume
V_{ch}	channel volume
V_p	pillar volume
$V_{pipetted}$	pipetted volume of sample into PCR tube for Qubit assay
v	velocity
$\overrightarrow{\boldsymbol{v}}$	velocity vector
w	width
We	Weber number
x, y, z	Cartesian coordinates

Greek letters

Symbol	Description
η	dynamic viscosity
θ_{adv}	advancing contact angle
θ_{red}	reducing contact angle
θ_{stat}	static contact angle
ν	kinematic viscosity
ρ	density
ρ_{el}	electrical density
σ	surface tension

Chapter 1

Introduction

This chapter gives first general background information about microfluidics and the lab-on-a-chip concept, followed by the Master's thesis problem description, the approach used to solve this problem and a literature survey of the state-of-the-art.

1.1 Microfluidics and the lab-on-a-chip concept

The start of microfluidics, *i.e.* the handling and studying of fluids in the nanolitre to attolitre (10^{-9} to 10^{-18} L) range (length scales less than a millimetre, hence the name microfluidics), was in the early 1950's when the basics were established for the modern ink-jet technology. The real revolution came when the first miniaturized gas chromatograph was realized by Terry *et al.*[1], which is shown in figure 1.1. A little bit more than a decade later, in 1990 to be precise, Manz *et al.* introduced for the first time the term micro total analysis system (μTAS)[2], together with a microfluidic liquid chromatography device, fabricated using Si-Pyrex technology[3]. A photograph of this device is also shown in figure 1.1. The term which is nowadays more common is lab-on-a-chip (LoC). The use of this word started in 1995 when Moser *et al.* published an article about glutamate and glutamine biosensors[4]. This broad term covers a range of special classes of miniaturized devices: lab-on-a-chip, biochips, bio-micro-electro-mechanical systems (bioMEMS), microreactors, and point-of-care devices, just to name a few. They all have the same aim, namely to control concentrations of molecules in time and space. All these different classes are the result of a highly interdisciplinary field of research. This multidisciplinary character is visible in the broad range of scientific journals publishing about microfluidics, μTAS, and LoC (*e.g.* Lab-on-a-Chip, Sensors and Actuators, Analytical Chemistry, Journal of Micromechanics and Microengineering, and Applied Physics Letters). The development of number of publications per year on the topics of microfluidics, micro total analysis system, and lab-on-a-chip is shown in figure 1.2. These graphs clearly indicate that it is a development of the last 15 years. The start of this development can be coupled to the Defence Advanced Research Projects Agency (DARPA) of the US Department of Defence. This agency supported in the 1990's the development of field-deployable microfluidic systems that can be used for the detection of chemical and biological threats[5].

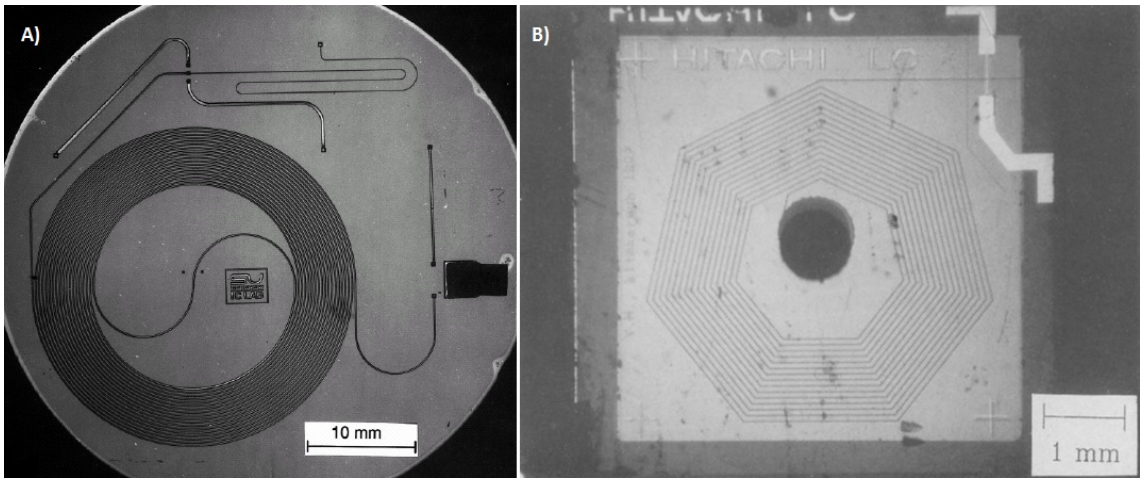

Figure 1.1: First chromatography systems on chip, with A) The 1.5 m spiral capillary column and GC system on a Si wafer with a diameter of 5 cm, which is made by Terry *et al.*. Picture taken from 1. B) Photograph of the liquid chromatography chip made by Manz *et al.*. Picture taken from reference 3.

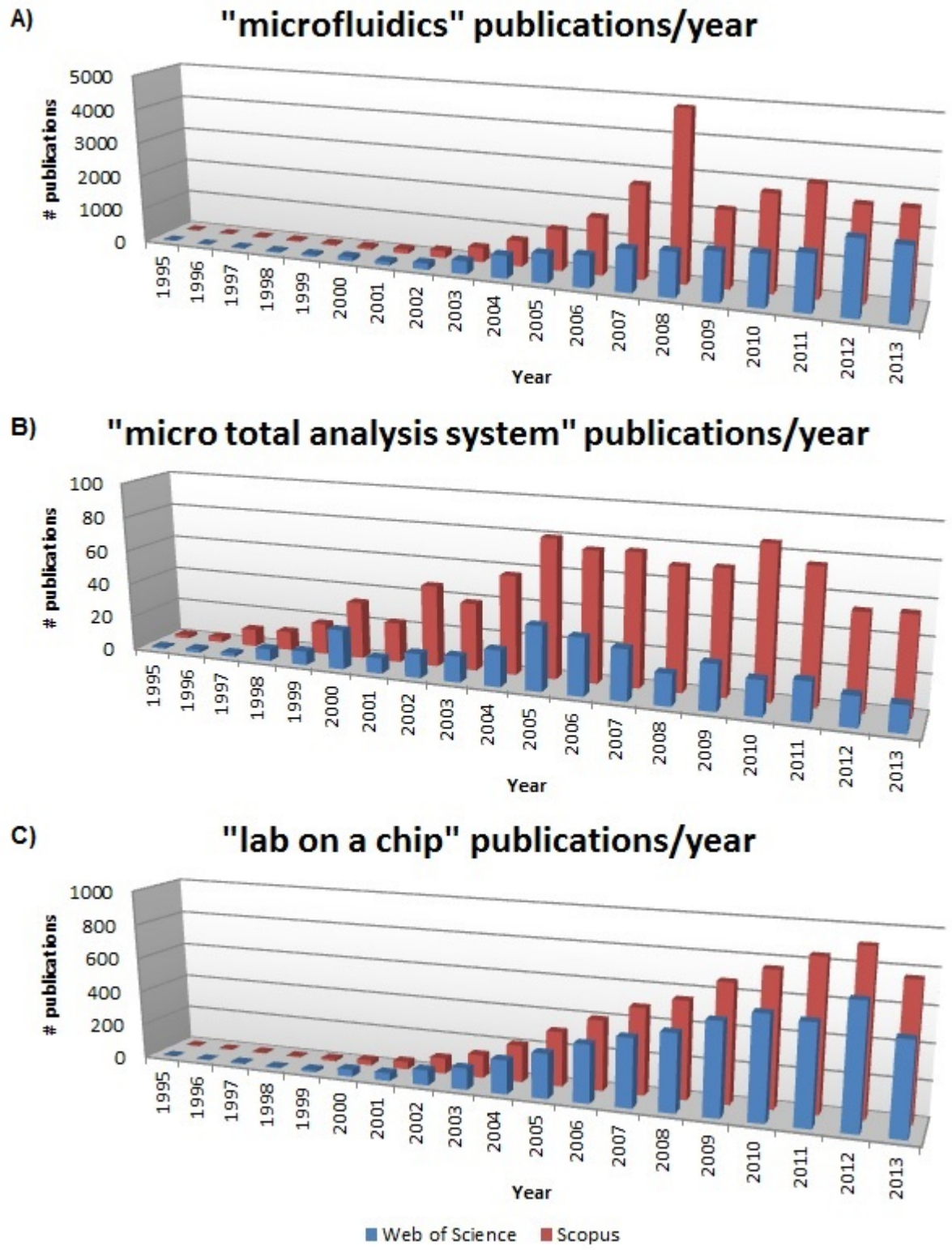

Figure 1.2: The amount of publications per year on A) microfluidics, B) micro total analysis system, and C) lab on a chip, lab-on-a-chip, lab on chip, lab-on-chip found in the renowned databases of Elsevier's Scopus[6] and Thomson Reuters' Web of Science[7].

A variety of other microfluidic devices and structures, such as microvalves[8] and micropumps[9], have been realized during the late 1980's and early 1990's. The combination of all these different microfluidic compounds, together with microelectronics, can form complex microfluidic systems. These chips can contain sample preparation structures, analysis structures, reservoirs, detection structures, etc. An example of such a sample-in-answer-out system is a DNA multiplication and detection chip[10–12]. A comprehensive review about the development of μTAS is written by Reyes *et al.*[13] and worthy to read.

All these different structures are mainly made in silicon or glass. Because of this material choice, well established fabrication techniques of the semiconductor industry and micromachining, like photolitho-

graphy, etching, and deposition can be used. This is directly a big drawback. The fabrication process for the silicon and glass structures requires an expensive conditioned cleanroom facility and sophisticated micro-mechanical fabrication tools. Also the substrates themselves are rather expensive. Therefore alternative materials are developed, such as polymer materials, like poly(dimethylsiloxane) (PDMS)[14], poly(methyl methacrylate) (PMMA)[15], polycarbonate (PC)[16], polystyrene (PS)[17], polyethylene terephthalate (PETG)[18], cyclic olefin copolymer (COC)[19] and cyclic olefin polymers[20], and others[21]. But sometimes the production process or the desired structure does not allow the use of polymers. For example high aspect ratio structures are rather difficult with polymer materials without special release coatings[22] and channels of nanometre scale, ideally less than 50 nm, often need rigid walls[23]. Nevertheless, sometimes polymers are more desirable than glass or silicon, for example their gas permeability is applied in structures that are used for living mammalian cells[5]. Another disadvantage is that it cannot be a fully automated process[24].

The miniaturization has several benefits for the performance. The first application of microfluidic technology, *i.e.* analysis, has benefit of some of the useful capabilities. The ability to use very small quantities of sample an reagents, to carry out separations and detections with high resolution and sensitivity, its low costs, short analysis times, and small footprint are some of the most important benefits for analysis[5]. The advantages can be further enhanced by switching to the even lower volumes of droplet based systems. Such a system uses (sub-)nanolitre droplets in a immiscible continuous phase. This has the advantage that dispersion of reacting volumes by shear forces on the contained fluid, imparted by the channel walls (*i.e.* the no-slip boundary condition of hydrodynamic pressure driven flows creating the Taylor-Aris dispersion of the Poiseulle flow) is suppressed[25,26]. Such dispersion generates a residence-time distribution, which can cause significant variation in the efficiency of the LoC device[27]. A droplet system localizes the reagents within discrete volume elements, which have, when the geometry and flow rate are optimal, no contact with the channel wall and thus the no-slip boundary condition cannot be established. This phenomenon is shown in figure 1.3. Other advantages of these systems are reduced cross-contamination, and enhanced mass and heat transfer[28]. This precision and the well-definable droplet size make droplet-based microfluidic systems an ideal platform for different "-omics" approaches and other fields where minute quantities of samples are available. There are already some different droplet-based systems available for (bio)chemical screening[29,30], enzymatic kinetic assays[31], DNA multiplication[32–38] and sequencing[39], and proteomics[31,40–43]. For more extensive details on different facets of microdroplet-based systems the reader is referred to a number of excellent review papers[27,40,44–47].

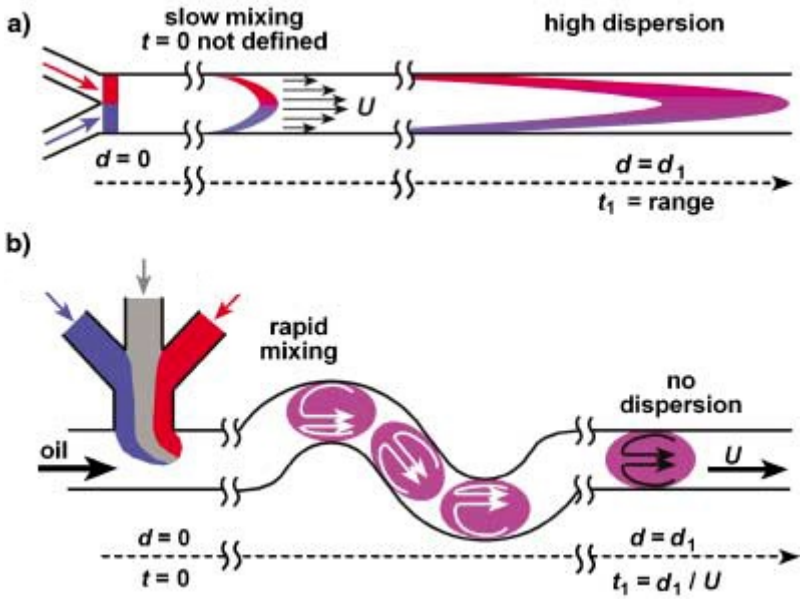

Figure 1.3: A comparison between reactions in A) a hydrodynamic pressure driven single-phase flow and in B) a droplet-based hydrodynamic pressure driven two-phase flow. Picture taken from reference 29.

After reading this all, one conclusion that can be made regarding the miniaturization of analytical equipment to chip sizes and that is really significant for such systems, is that reduction in size of analytical equipment often translates to a reduction in analysis time and costs[48]. This introduction can only be closed with a citation of one of the pioneers in the LoC world, George Whitesides[5], which he made in 2006. The developments of the last eight years clearly moved the microfluidics from adolescence to

early adulthood:

"HOWEVER, ITS IMPACT ON SCIENCE HAS NOT YET BEEN REVOLUTIONARY. REVOLUTIONS IN TECHNOLOGY REQUIRE BOTH A BROAD RANGE OF DIFFERENT TYPES OF COMPONENT AND SUBSYSTEM, AND THEIR INTEGRATION INTO COMPLETE, FUNCTIONAL SYSTEMS.THE FIELD OF MICROFLUIDICS IS IN EARLY ADOLESCENCE, AND STILL LACKS BOTH THESE ESSENTIAL REQUIREMENTS, IN ADDITION TO THE INTEGRATION OF COMPONENTS INTO SYSTEMS THAT CAN BE USED BY NON-EXPERTS. AS A FIELD, IT IS A COMBINATION OF UNLIMITED PROMISE, PIMPLES AND INCOMPLETE COMMITMENT. THIS IS A VERY EXCITING TIME FOR THE FIELD, BUT WE STILL DO NOT KNOW EXACTLY WHAT IT WILL BE WHEN IT GROWS UP."

1.2 Assignment description

The problem investigated in this master thesis is the problem of analysing forensic samples found on the crime scene. The current method is that a crime scene investigator collects every potential interesting sample and sends this to the Dutch Forensic Institute (Nederlands Forensisch Instituut, NFI) in The Hague (NL). Once the samples are there, they start to work up the samples, *i.e.* purifying the sample, performing cell lysis, collection of DNA, performing a multiplication reaction on the DNA, and finally making a short tandem repeat (STR) profile of the DNA. A general DNA analysis scheme is shown in figure 1.4.

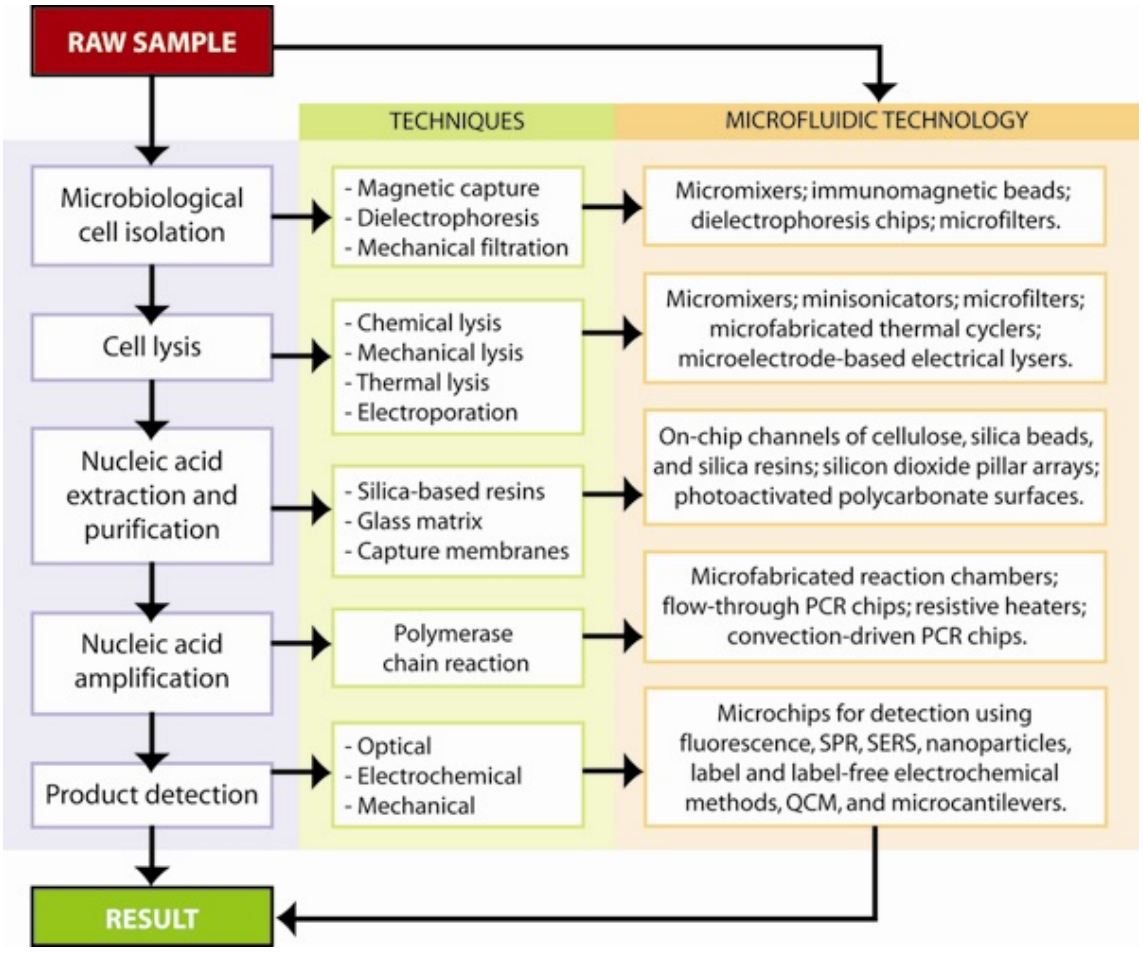

Figure 1.4: Flow-chart of chip-based DNA isolation, extraction, amplification, and detection. The name of the step is on the left, the traditional method steps are in the middle, and the translation to microfluidic technology is in the right column. Picture taken from reference 49.

All these steps need time, sometimes even tens of days[50,51]. This waiting time is undesirable because the results can become irrelevant or outdated, even before they reach the police. Also, during this period of waiting on results, the perpetrator has the time to hide or destroy important evidence, to flee, or to commit another crime. This waiting period also increases because of samples that do not contain DNA at all. These samples are not filtered out before the analysis, so they take precious time and money away from other samples and they delay the important samples. The numbers show that

the NFI investigated 47,700 human biological trace samples in 2013[52]. A more detailed overview of the amount of DNA samples per year can be found in the graph in figure 1.5. In this graph it is clearly visible that the amount of samples doubled in the past five year. An investigation of cases from police department Kennermerland shows that 30% of the serious crime samples does not contain DNA and that for high volume crimes 17% does not contain DNA[50]. This difference can be explained by the fact that for high volume crimes only samples with a high change for DNA profiling, like blood and saliva samples, can be send to the NFI. It is therefore important that "empty" samples will be eliminated as fast as possible in the analysis process and that the important and relevant information becomes available as fast as possible. More information about the time needed for different steps of the process can be found in the Master's theses of Mapes[50] and de Wolff[51]. This lack of time is also visible in the United States. In the United State there is a backlog of $\pm$ 800,000 samples in 485,000 crimes, which are awaiting analysis[53]. The worldwide forensic world would therefore be very interested in a LoC system that can do a screening for important samples.

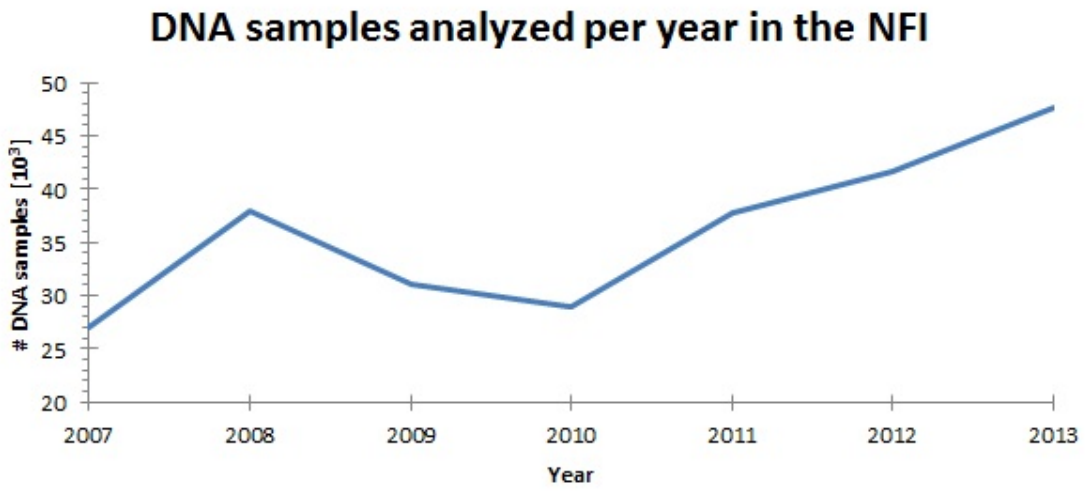

Figure 1.5: The amount of human biological trace (DNA) samples per year in the period of the last five years. Data is taken from references 52,54–58.

The collection of crucial samples, analyse them for important information, and the elimination of "empty" samples should be possible with the LoC technology. The benefits listed in the previous section make this technology very suitable for fast DNA analysis. Such a DNA LoC will consist of different parts, *i.e.* a part for the DNA extraction from the lysed sample, a droplet generator for the formation of drops containing sample DNA and amplification chemicals, an amplification reactor, and a detection part. These steps are also listed in the flowchart of figure 1.4, where a translation is made between conventional techniques and microfluidic technology. A project involving all these steps is too much for a Master's thesis, so in this project the focus was set on the DNA extraction and purification part. It is important that this part can be implemented with the other downstream processes[10,59].

The chip can, for example, be coupled to polymerase chain reaction (PCR) chips[60–64] for amplification and/or electrophoretic separation chips for detection[60,65–70]. If these technologies are combined into one system or chip[12,71], it can give results of the DNA analysis in a short period of time. Besides these subsequent steps, there are also other techniques that require purification of DNA. Examples of these steps are northern blotting and microarray assays[72]. The addition of a μSPE chip is valuable for PCR chips since PCR needs DNA samples that are free of contaminants and inhibitors[73,74]. Crime scene samples are often collected from tissue, blood, food, or other environments. This makes the samples a mixture of potential interesting cells, worthless cells, and contaminants. These contaminants can also be PCR inhibitors, which can both be endogenous and exogenous[75]. Examples of inhibitors with their corresponding forensic source are haemoglobin (blood), urea (urine), bile acids (faeces), humic acids (soil), polysaccharides (faeces), melanin (tissue and hair), and indigo dyes (denim clothes)[48,76,77]. These inhibitors can result in delayed threshold cycles, reduced density of detection for larger amplicons, or even complete PCR amplification failure[74]. The well-established DNA isolation and extraction procedures, for example those involving the phenol/chloroform/isoamyl alcohol (PCI) method[74], the Chelex method[74], and density gradient centrifugation[78], have proven to be efficient in the removal of interfering species, but the main problem is that they require relatively large reagent volumes, making the concentration of DNA dilute. These large volumes are not easily transferrable to microfluidic platforms[59]. Another problem is that these processes are complex and time-consuming[72].

Making the DNA concentration more dilute is undesired because 1 μL of a lysed blood sample typically contains only 35 ng of DNA[79]. In general, one mammalian diploid cell typically contains only 5 to 7 pg of DNA, which is 1.6-2% of the complete cell[75]. Besides this small amount of DNA there is also 150 µg of proteins present in this sample[79]. These proteins also need to be removed for the PCR[79] and is commonly done by purification using a silica-based resins, chaotropic salts*, and organic solvents (like isopropanol)[83]. However, chaotropic salts and organic solvents cannot be used in microfluidic SPE coupled with PCR, since it is known that these salts and solvents (especially isopropanol) are PCR inhibitors when PCR is performed in the small volumes of microfluidics[10,76,79,84–86].

The extraction part is thus an important part of the whole system. The most desired extraction system extracts as much as DNA possible, without any proteins, from the lysed sample and subsequently elute as much as possible of that DNA in an as small as possible amount of liquid. Therefore there is the idea to design a chip that can perform the elution of the DNA in a buffer plug. This plug can for example be formed in oil. From here on it is much easier to perform the PCR, since the DNA is already confined in a buffer plug/droplet. Some different strategies are already described in the literature. An review is given in the next paragraph.

1.3 State of the art

Conventional analyte extraction and preconcentration are well-known methods in all kinds of different laboratories. In the past decade, a lot of effort is put into the miniaturization of these methods with the help of microfabrication. An example of such an extraction method is solid phase extraction (SPE). The basic principle consists of three distinct steps[87]. The first step is based on affinity chromatography, where relevant analytes are retained on the surface of a solid phase. In the second step, the SPE column is rinsed/washed in order to remove all impurities, like solvents, PCR inhibitors and proteins. In the third and last step, the analyte is eluted with a small amount of elution liquid (often a buffer). The result is an analyte solution in which the analyte exists in a purified and more concentrated state. SPE is therefore used to overcome detection-limit problems and to eliminate a potential inhibitor. SPE is one of the predominant methods which are used by researchers in the field of microfluidics/LoC devices[72]. Other methods that are used are solid phase reversible immobilization[88,89], which works mainly with magnetic particles or polycarbonate structures, and liquid/liquid extraction[90], which works with a phenol/chloroform mixture. The SPE of an analyte can be beneficial not only for analyte preconcentration, but also for removal of other impurities or changing solvent conditions[91]. In the past, capillaries with SPE material were coupled to a microfluidic chip[92]. It is advantageous to put the SPE on-chip because of the elimination of the dead volume created by coupling the capillary to the chip,

*A chaotropic salt (chaotrope) is a salt of high ionic strength. The addition of such a salt, like guanidine hydrochloride, guanidine thiocynate, or sodium iodide to a silica-DNA system is an endothermic process, which induces a positive entropy change by binding water molecules and thus disrupting the hydrogen bonding network, van der Waals forces, and hydrophobic effects. For example, a guanidine hydrochloride molecule will bind up to 10 water molecules to itself[80], effectively dehydrating both the DNA and silica surface. The ions with a high ionic strength will form then a bridge between the negative surface charges of the silica and the negatively charged DNA, as is shown in the figure in this footnote[75,81].

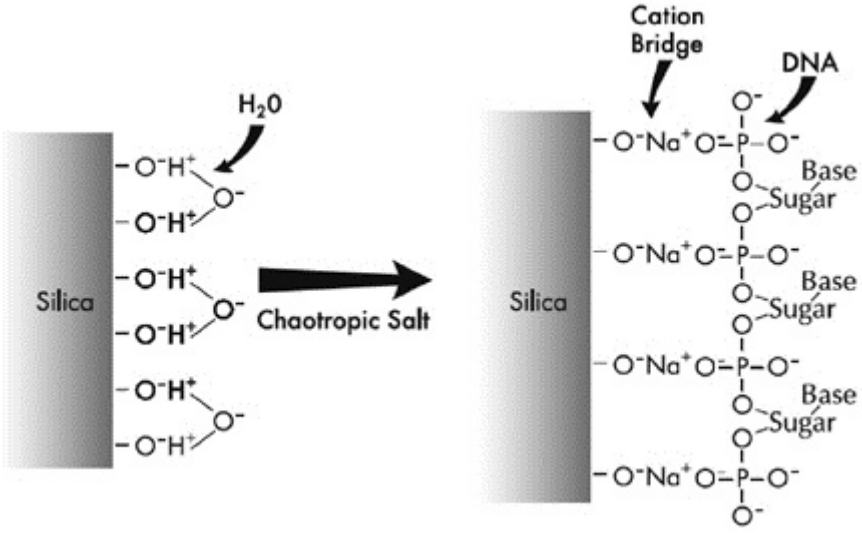

The dehydration of DNA also influences the conformation of DNA. B-DNA, for example, will bind up to 20 water molecules per nucleotide. The addition of the chaotrope induces a conformational change of helical B-DNA to either A-DNA or C-DNA. This results in a decrease in solvent-accessible surface area, a loss in bound water, and an entropy increase of the solution[82]. When the pH of the solution is lowered to a more acidic pH, for example from eight to five, the surface concentration of hydroxyl groups on the silica will increase. This increases the ability of hydrogen bond formation between the DNA and silica surface and it decreases the free hydroxyls that compete with DNA for hydrogen bonding sites on the silica surface[75].

sample handling losses, contamination by off-chip sample preparation, and it can simplify the production process of the device[91]. The SPE idea has already been translated to LoC technology. During this translation, different approaches have been put forward, which can be divided into three main categories (or a combination of these)[87]. The first approach uses beads with or without functionalization in an extraction chamber/column, for example the one designed by Oleschuk *et al.*[91]. The second approach uses a channel or column that is filled with a porous polymer (monolith), for example the devices designed by Yu *et al.*[93] and Stachowiak *et al.*[94]. The third approach uses a solid phase and column that are made out of one material and which are shaped by etching, for example the device of Sarrut *et al.*[95]. All these different approaches have a common goal, namely maximising the interactions between the analyte molecules in the solution and the solid phase constituting the device. The most common used substrates in these approaches are silicon, silica, or a silicon/silica hybrid substrate. The following examples all use one of these substrates, unless otherwise mentioned.

1.3.1 Beads-filled columns

The use of bead-packed microchannels was long and still is hindered by the packing of the microchannel with beads[75]. These beads can be with[91] or without[10,59,96,97] immobilized reagents as stationary phase. Oleschuk *et al.* reported a design that allows the user to exchange the beads[91]. This technique can be used to perform on-chip SPE and capillary electrochromatography. For this method, they etched a reaction chamber with a width of 200 μm and a depth of 100 μm into a glass substrate. The inlet and outlet were created by leaving an interstice of 1 μm between the top of the chamber side wall and the glass lid. Previously functionalized beads were added into the chamber via a side channel. The small inlet and outlet also immobilized the beads within the chamber. This device is capable of preconcentrating the sample by a factor of at least 100 times. A schematic representation of this device can be found in figure 1.6.

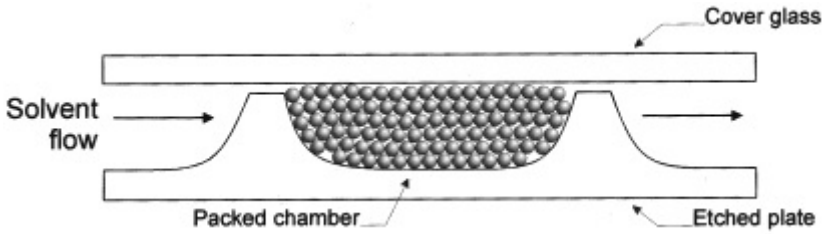

Figure 1.6: Schematic cross-section of a bead-packed microfluidic structure, showing the beads packed in a chamber like structure with an inlet and outlet. Picture taken from reference 91.

The systems without functionalization of the beads work mostly with chaotropic salt buffers[73,96]. These high ionic strength solutions allow that DNA will adsorb to the silica surface inside the microfluidic structure, while other macromolecules, like proteins and lipids, remain free and unbound in solution[48,98]. These contaminants can be removed by an ethanol or isopropanol-based washing step[98]. In order to overcome the difficulty of the filling of the column, these beads can be loaded into the column via a sol-gel method. With this method, the channel is first filled with an aqueous slurry that contains the silica beads. After filling, the beads are rinsed with hydrochloric acid in order to hydrolyse the bead and channel surface. Then, the channel is rinsed with a with HNO_3 hydrolysed tetraethyl orthosilicate (TEOS) solution (the sol). The sol reacts with the silica beads inside the channel and the channel walls, creating the gel[73]. This sol-gel method by Breadmore *et al.* has the potential to be useful for purification of DNA. However, Wolfe *et al.* found in their research that sol-gels alone did not yield good extraction efficiencies[99]. These low extraction efficiencies can be attributed to the low reproducibility of the sol-gel reaction. It is hard to control the pore size and it has the tendency to form cracks between the gel and the channel wall due to shrinkage of the sol-gel[72]. The sol-gel reaction can be improved, as is shown by Wu *et al.*. They used a tetramethyl orthosilicate (TMOS)-based sol-gel with polyethylene glycol as the porogen[†]. This device has an extraction efficiency of 68 $\pm$ 3% for DNA from whole blood. However, this device still works with chaotropic conditions.

This method can also be done off-chip in a capillary. This approach is described by Tian *et al.*[48]. They implemented silica particles in between two capillaries and used chaotropic conditions for the extraction of the DNA from the solution. A schematic representation of this set-up is shown in figure 1.7. The outlet capillary can be directly coupled to a CE instrument. The achieved DNA recovery from the solution is around 70% to 80%.

[†] A solvent that provides pores ranging from nanometre to micrometre size with a continuous interconnected network of channels[100].

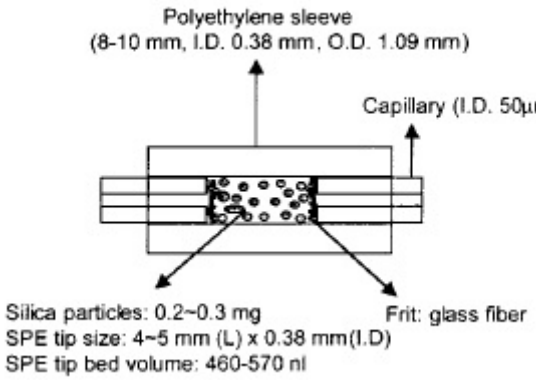

Figure 1.7: Schematic representation of a capillary-based μSPE device. Picture taken from reference 48.

1.3.2 Monolithic columns

The porous polymer approach uses capillaries or columns that have been filled with a porous polymer structure. Such chromatographic supports are called monoliths[101]. These type of supports were introduced in the late 1980's and early 1990's[102,103]. The use of a monolith in a μSPE device is proposed by Yu *et al.*[93] and is based on the work of Svec *et al.*[104–106]. In order to fill the capillary or column with the porous polymer, a solution of monomers and initiator in a porogenic solvent is injected into the capillary and these monomers are polymerised by photo-initiation by UV exposure[93,100] or thermal initiation[100]. The monomer choice determines the final properties of the porous structures. Examples of these properties are the hydrophobicity, surface charge, and functionalization possibilities[107,108]. Two of the largest advantages of such a monolithic porous structure is the high surface-area-to-volume ratio and the accurate placement of the monolith matrices within the microfluidic device due to local polymerization by UV or heat[93,100,109]. A scanning electron microscope (SEM) image of such a porous polymer-filled column is shown in figure 1.8. However, the extraction efficiencies of DNA purification and separation performed in such systems is low and it requires high salt and pH buffer for the DNA release[101]. These low extraction efficiencies can most probably be addressed to the low reproducibility of the polymerization reaction, the same problem as with the sol-gel reaction described before. Moreover, the required buffers are not suitable for PCR amplification because of their high salt concentration[100].

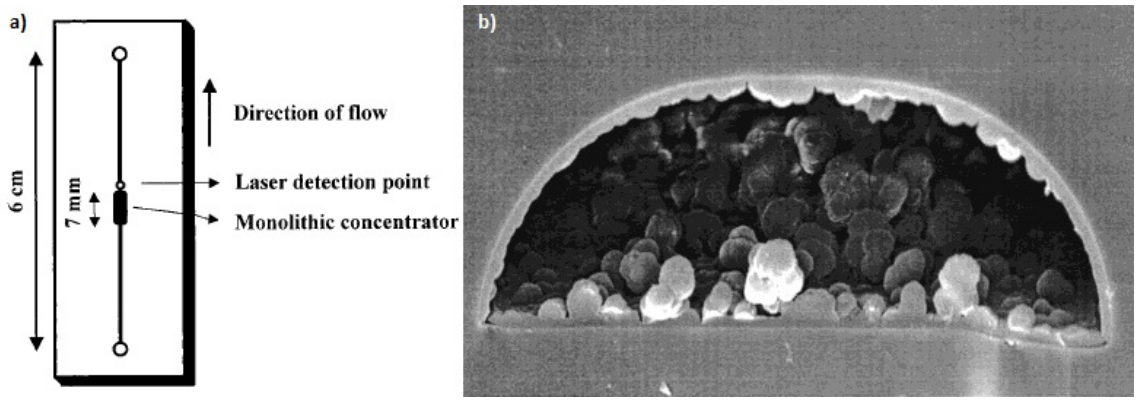

Figure 1.8: A porous polymer-filled μSPE column, with a) microfluidic chip layout, and b) SEM image of a monolithic ion-exchange concentrator (μSPE column). Picture taken from reference 93.

This method is not only limited to silicon or glass capillaries. Stachowiak *et al.* fabricated such monolithic porous structures inside a plastic microfluidic device[94]. The main disadvantage of this method is the device-to-device reproducibility of the monolith.

Wen *et al.* designed a μSPE chip with two regions, a protein binding C18 reversed phase column and a monolith made out of the monomer 3-(trimethoxysilyl)propyl methacrylate, which was functionalized with TMOS[79]. The C18 reversed phase column captures most of the, mostly hydrophobic, proteins from whole blood samples, such as haemoglobin, while having a minimal binding with DNA. This ensures a more effective extraction of DNA in the μSPE column. They achieved an extraction efficiency of 69 $\pm$ 1% for their combined system. However, the TMOS functionalization requires chaotropic conditions in order to perform its function, making it not suitable for PCR on chip[10,76,79,84,85]. This is a

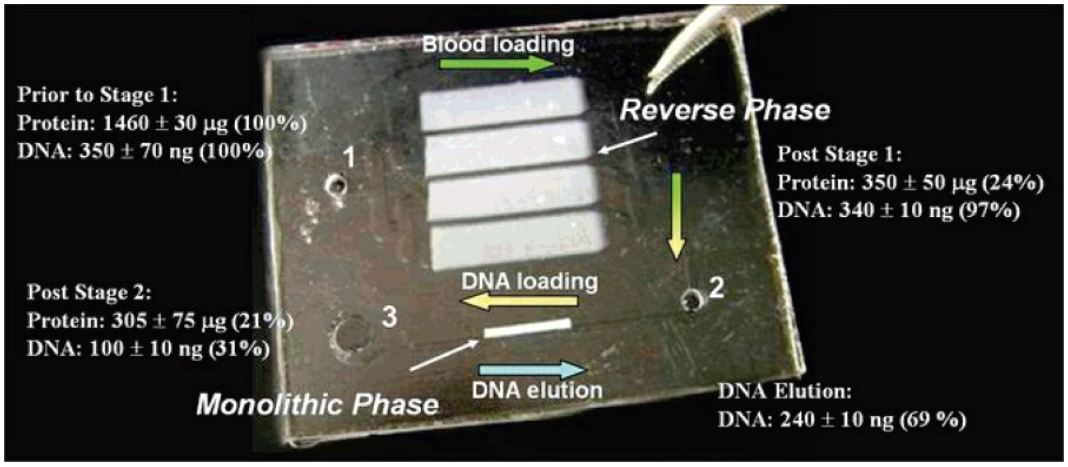

Figure 1.9: The integrated protein capturing C18 reversed phase column and the DNA μSPE column. The arrows show the flow direction for the different steps in the process and the percentages show the mass balance through the system. Picture taken from reference 79.

problem Wen *et al.* encountered during their research. The chip designed by Wen *et al.* is shown in figure 1.9.

1.3.3 One-piece columns

This method has the most simple production process of the three different methods. Here, the solid phase is shaped directly into the substrate material by etching. A surface functionalization can be done afterwards, but is not always necessary, for example in the case with DNA extraction with silica surfaces and chaotropic salts[83]. The two most typical structures for this kind of extraction are an array of micropillars, which can be present in all kinds of shapes (see figure 1.11 and 1.12[95,98] and one[110] or multiple parallel channels[111] (see figure 1.10). Pillars are in this case used to increase the surface-area-to-volume (SA-V) ratio of the column. The concept of using pillars for DNA extraction was firstly demonstrated by Christel *et al.* in 1999[112]. The direct etching of the solid phase into the substrate circumvents the problems that are associated with the filling of the channels with binding matrices, which needs to be done after the fabrication of the device[49].

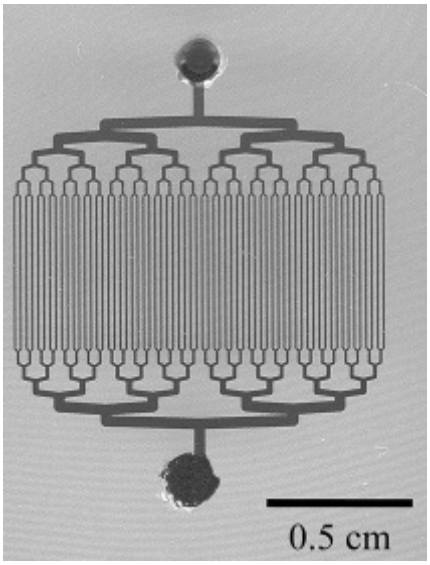

Figure 1.10: Picture of a SPE device based on parallel channels. Picture taken from reference 111.

The method demonstrated by Cady *et al.*[83] is based on the increase in surface area by adding pillars in the microfluidic channel. With these pillars, they increased the surface area within the channel with 300-600%. The silica surface of the pillars and channels allowed DNA extraction with the use of a chaotropic salt. A binding capacity of approximately 82 ng cm^{-2} has been reported, but only 10% of the loaded DNA was eluted.

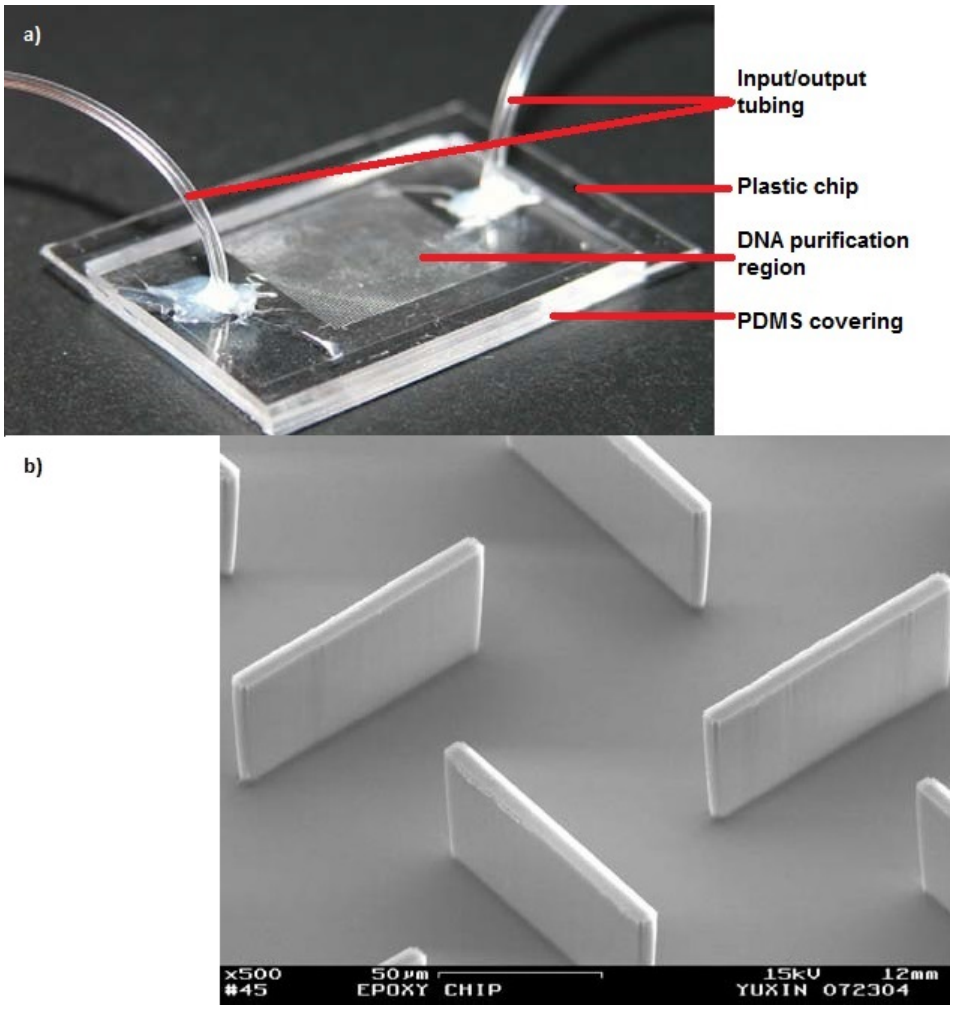

Figure 1.11: An polymer-based extraction chip, with a) photograph of the complete chip, with PDMS covering and tubing, and b) SEM image of the epoxy-based pillars in the DNA purification region. Picture taken from reference 98.

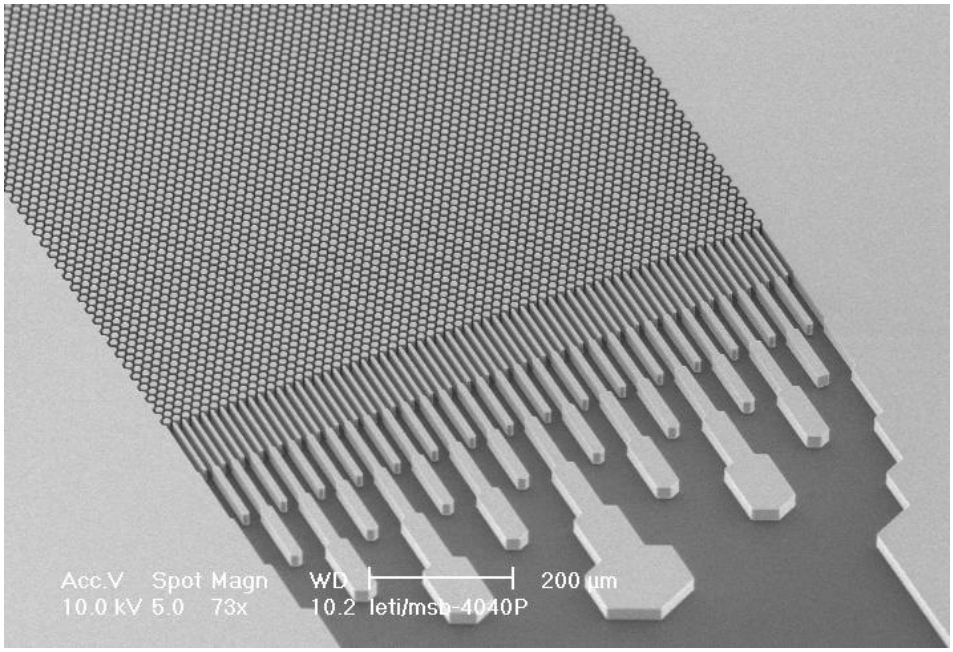

Figure 1.12: SEM image of an array of micropillars etched in silicon. Picture taken from reference 95.

Another approach in the one-piece column method is the use of a pH sensitive amine surface coating for extraction based on electrostatic interaction between DNA and the pH sensitive moiety, the so-called ion exchange method. Binding of DNA to the pH sensitive layer occurs when the amine group of this pH sensitive layer becomes protonated at an acidic pH, as DNA is negatively charged. Binding is thus based on electrostatic interactions. A simple increase in pH releases the DNA[76]. The pK_a value of this pH sensitive layer determines which pH is necessary for the DNA release. If a proper layer is chosen, the DNA can be released with a buffer that has the proper pH for PCR amplification.

This method is originally proposed by Yoza *et al.*[113,114]. They used bacterial magnetite particles (BMPs)[‡] as a solid substrate for the amine coating and performed bead-based extractions. Nakagawa *et al.*, who are of the same group as Yoza, used the same approach, but they applied SAMs of 3-aminopropyltriethoxysilane (APTES) and 3-[2-(-aminoethylamino)- ethylamino]-propyltrimethoxysilane (AEEA) in microfluidic channels without structures inside them, instead of on BMPs[110]. Both of these self-assembled monolayer (SAMs) contain amino end groups, which is a pH sensitive moiety with a pK_a value in the pH 9.5 range[111]. However, some authors mention other values for the pK_a value of APTES. For example 7.6[116]; 6.55 ± 0.73, 7.3 ± 0.8, or 9.94 ± 0.19[117]; 4[118]; and 10[119]. This means that the extraction of DNA can be accomplished without the use of organic solvents and chaotropic salts[86,111]. The binding capacity of these SAMs are 82 ng cm^{-2} and 194 ng cm^{-2} for APTES and AEEA, respectively. The recovery of DNA (eluted amount) for these SAMs is 45%. This method looks promising, although there is a minor disadvantage. The buffers to extract and elute the DNA are of a pH of 7.5 and 10.6, respectively[110]. The pH of the elution buffer is too high for optimal PCR[111]. So APTES is still of interest for a pH-based extraction method. The PCR amplification with Taq polymerase (one of the most widely used polymerase enzymes) prefers a pH of $\sim$9 for optimal amplification[120]. If extraction needs to be done at higher pH values, post-extraction dilution of the mixture is possible to lower its pH.

There is another approach for the ion exchange method. This one is introduced by Cao *et al.* and uses a chitosan functionalization on silicon as pH sensitive layer to reversible bind DNA[111]. It can also be used for RNA purification[84]. The pH sensitivity is due to the amino group, which chitosan possesses. This amino group has a pK_a of 6.3[75,84,111,121] and is the only type of protonatable functional moiety in the biopolymer molecule. This ensures strong electrostatic interaction between the DNA and the chitosan. The amino group is cationic below its pK_a and neutral above it. Cao *et al.* therefore use a MES buffer of pH 5 for the extraction of DNA and a TRIS buffer of pH 9 for the elution. This condition is more optimal for subsequent PCR amplification. The use of a chitosan solid phase is clearly advantageous over a silica, not only for the elimination of reagent-based PCR inhibitors, but also for enhanced extraction efficiencies, which are typically $47 \pm 4.2\%$ for silica with chaotropic conditions and $65 \pm 1.9\%$ for chitosan and aqueous conditions[84,111]. The hydrophilic character of chitosan reduces hydrophobic interactions with proteins, leading to lower nonspecific adsorption of proteins. This ensures a better purification of DNA.

An ion-exchange layer is necessary because the silica surface is also negatively charged over a wide range of different pH values. This is because of the weak acidic silanol groups on the surface of silica. These groups have a pK_a of 5 to 7[122]. DNA is a polyelectrolyte, containing two fixed negative charges in the phosphate backbone per one base pair over a wide range of pH values[101,111]. Thus, a negatively charged surface facilitate electrostatic repulsion of the fixed negative charges on the DNA, and therefore inhibits adsorption on bare silica if no chaotropic conditions are applied.

It is also possible to implement the chitosan phase in a μSPE column made of PMMA, as is shown by Reedy *et al.*[85]. Such a device is shown in figure 1.13. The advantage of this approach is that PMMA is photoresist. The fabrication process is therefore simplified because it omits an etching step. However, they use X-ray lithography in order to make the deep channels because with X-ray lithography it is possible to make high-aspect ratio structures in resist[22].

Another way of performing pH induced extraction does not work with organic monolayers. Hashioka *et al.* fabricated a column with micropillars and coated these with alumina (Al_2O_3)[123]. This coating facilitates electrostatic immobilization of DNA under acidic conditions (pH 4.7) and elution under alkaline conditions (pH 10.1). This elution pH is too high for PCR amplification[111], however, post-extraction dilution is also a possibility here to lower the pH before PCR.

Both APTES and chitosan will be discussed more in-depth, since they both look promising as an ion exchange coating for the solid phase of the plug-based μSPE column that can be used for the extraction and purification of DNA.

[‡]BMPs are magnetic Fe_3O_4 nanoparticles with a single Weiss domain. These particles are produced by bacteria and in the size range of 50-100 nm[115].

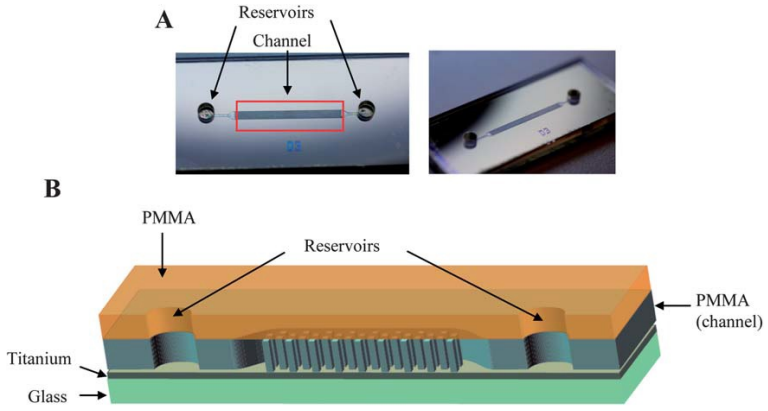

Figure 1.13: A μSPE column fabricated out of PMMA, with a) a photograph, and b) a schematic of the PMMA μSPE device. Picture taken from reference 85.

APTES

APTES is an aminosilane, having a propyl chain chain in between the electron-rich amino group and the silane group (see figure 1.14). The surface chemistry of APTES on silica is well-defined and common practice in laboratory, making it one of the most frequently used organosilanes for the preparation of amino-terminated surfaces on silica. These surfaces are especially attractive for applications like DNA microarrays[124,125], protein arrays[126], sol-gels[127], and other biotechnological applications. The surface functionalization of silica with APTES is as simple as making an APTES solution, for example in ethanol[128], ethanol with 5% water[129], toluene[130], or phosphate-buffered saline[130] and bringing it in contact with the silica surface. The general understanding of APTES film formation is that the silanization starts with the hydrolysis of the ethoxy groups, a process catalysed by water[131]. This leads to the formation of silanol groups (Si$-$OH). The physisorbed layer of water on the silica surface is already enough to catalyse this reaction[132]. The APTES silanol groups then condense with the surface silanol groups of the piranha cleaned and activated silica surface, creating an aminopropyl silane self-assembled monolayer (SAM). The two side-directed silanol groups of APTES can form a siloxane network via condensation with side-directed silanol groups of other APTES molecules, which are in close proximity[130]. This horizontal polymerization can be enhanced with several different methods. For example with *in situ* heating (heating up the substrate to 70 ℃ during the deposition of the SAM[133]) or *ex situ* (curing the substrate and deposited film afterwards at 150 ℃[134]). This sounds pretty straightforward, however, the actual process is far more complex and sensitive to reaction conditions than this general understanding suggests[134–145].

This complexity is mainly due to the reactive amino group in APTES. It has the propensity to react in competing reactions. The amino group of adsorbed APTES can interact via hydrogen bonding or electrostatic interactions with the silanol groups on the silica surface and/or the silanol groups of hydrolysed APTES, which are in close proximity[136–138,146,147]. These competing mechanisms reduce the available silanol groups on the silica surface as well as in the APTES for further siloxane condensation[130]. Another mechanism that causes complexity is the possibility that APTES polymerizes. This mechanism gives rise to the formation a multilayer system. The structure and reactivity of a multilayer of APTES is different from a monolayer[130]. This sensitivity to solvents and conditions was already pointed out and investigated by Vandenberg *et al.* in 1991[134].

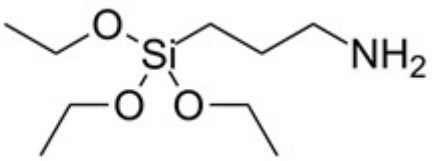

Figure 1.14: Chemical structure of 3-aminopropyltriethoxysilane.

Chitosan

Chitosan is a linear copolymer of 2-acetamido-2-deoxy-D-glucopyranose and 2-amino-deoxy-D-glucopyranose, which are joined by $\beta(1\rightarrow4)$ glycosidic bonds[148]. This creates a poly((1$\rightarrow$4)-2-amino-2-

deoxy-β-D-glucan)[149], which is a mucopolysaccharide. Chitosan is the second most abundant biopolymer in nature, close to cellulose, and is derived chemically by the N-deacetylation of chitin (poly((1$\rightarrow$4)-2-acetamide-2-deoxy-β-D-glucose)[150], which also is a derivative of glucose and can be found in, for example, the exoskeleton of arthropods (*e.g.* crab, lobster, and other animals from the group of crustaceans) and insects[151,152] (see figure 1.15). Chitin becomes soluble in aqueous acidic media (pH $<$ 6) when the degree of deacetylation reaches roughly 50%, the percentage from which on it is called chitosan[153,154]. Chitosan is an inexpensive, non-toxic, hydrophilic, biocompatible, and biodegradable polymer[155]. It shows also promises as bioactive material for implants, drug delivery vesicles, and tissue engineering[149,156–158]. In order to bind it to a silica (native oxide) surface, a linker molecule needs to be used. Cao *et al.* used (3-glycidoxypropyl)methyldiethoxysilane (GPTMS) as linker molecule and acidic conditions. GPTMS is a silane, and its chemistry with silica is common practice. According to Cao *et al.* the epoxy group of GPTMS will react with the hydroxyl group of chitosan, since they nowhere mention the possibility of the reaction of the epoxy group with the amino group. The epoxy-hydroxyl reaction forms an amino-terminated monolayer.

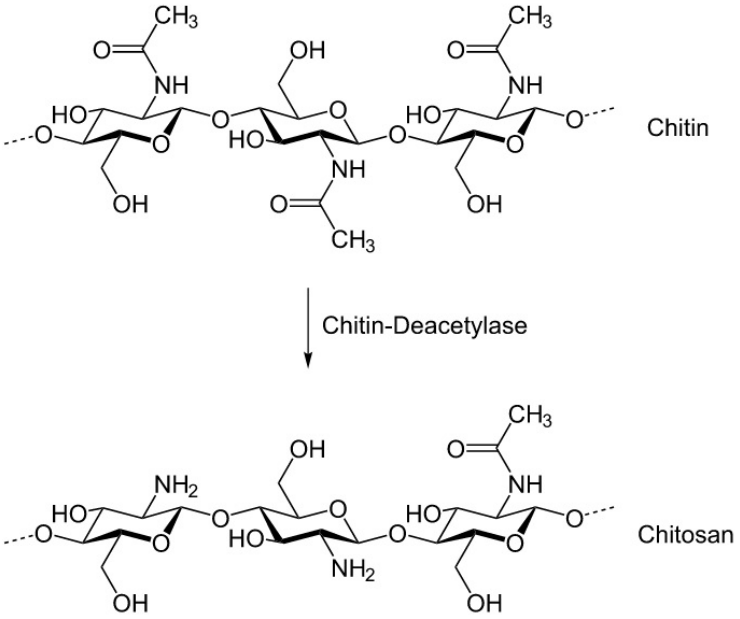

Figure 1.15: N-deacetylation of chiton to chitosan.

The reaction of chitosan with GPTMS is unclear. The part that is clear is that the oxirane group of GPTMS can undergo a nucleophilic S_N1 reaction in acidic conditions, for example with a nucleophilic group on a polymer chain[159]. The acidic conditions (for example in an acitic acid environment) protonate the oxirane and form an alkoxide[160], making it more electrophilic, and thus more reactive towards weak nucleophiles. The protonated oxygen of the oxirane will form the leaving group, a neutral alcohol. Then, the nucleophile can react with the most substituted carbon atom of the oxirane. This position is favoured because the C$-$O bond to the more substituted centre is weaker than the less substituted one. This reaction would form the most stable, and therefore preferred, carbocation[161]. The reaction mechanism of this step is shown in figure 1.16.

After this part it becomes more vague. The worldwide known study book "Organic Chemistry" of Carey describes alcohols, amines, and water as weak nucleophiles[161]. So all three can react with the oxirane. Several mechanisms for the coupling between GPTMS and chitosan are proposed in the literature and listed below. However, some of them are exclusively for sol-gel reactions and not for surface reactions, but they are still listed just to give an indication of the complexity and vagueness of the reaction between GPTMS and chitosan:

- Covalent bond formation between the epoxy ring and the primary amine, which forms a secondary amine group[162–165].
- Covalent bond formation between the hydroxyl groups of chitosan and the epoxy ring[111,166].
- Condensation reaction between the silane groups and hydroxyl groups[167,168].
- Ionic bonding between the positively charged amine groups (due to the weak acidic conditions) and the negatively charged silanes[163,169].

- Ionic bonding between the positively charged amine groups and the negatively charged oxygen resulting from the epoxy group[160].

- Hydrogen bonding between the amine, amide, and hydroxyl groups[160]. To make it even more complex, these formed covalent bonds are present in matrix where hydrogen bonds are also present[167,170].

To conclude this list, there is still a lot of uncertainty and unclarity about this reaction, so future studies have to show what kind of reactions truly occur.

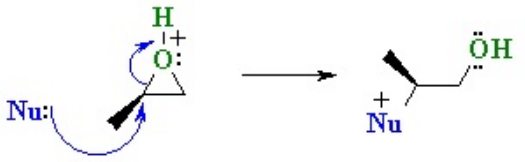

Figure 1.16: Reaction mechanism of the nucleophilic S_N1 reaction between the oxirane and the nucleophile

1.3.4 Combined approaches

The different approaches can also be combined to a so-called dual-phase device. This approach is demonstrated by Reedy *et al.*[76]. They used two orthogonal placed SPE processes, a chaotrope-driven μSPE column with silica surface and an anion-exchange μSPE column with chitosan phase, as reported by Cao *et al.*[111], which uses a total aqueous chemistry. The idea behind this coupled system is that the first step substantially reduces the volume of the sample, making it a more concentrated solution, and that the second step performs a more stringent extraction, removing all the PCR inhibitors (mainly guanidine hydrochloride and isopropanol, and possibly indigo). Although this looks like a promising method, the extraction efficiencies are lower than the ones of the individual methods, namely around the 30%[76].

1.3.5 Other methods

Besides these on-chip methods, there are also off-chip microfluidic methods. One type of such an off-chip method is already discussed. This is the method where two capillaries are coupled with beads in between them[48]. Other off-chip methods are often droplet systems that work with individual droplets on a digital microfluidic platform. Such a system is described by Lehmann *et al.* and uses magnetic silica beads and chaotropic salts to extract DNA from a droplet[171]. Magnetic fields direct the magnetic beads out of the droplet, isolating the DNA from proteins, cell debris, and other contaminants. These droplets are not confined in a microfluidic channel, making it less suitable for coupling it to a PCR chip.

Another off-chip bead-based method uses the BMPs and is designed by Yoza *et al.*[113,114] and Nakagawa *et al.*[86]. Yoza *et al.* They both use[86,113] APTES and AEEA functionalizations. The APTES and AEEA functionalized BMPs achieved an extraction efficiency of roughly 60%. Yoza *et al.* also used a dendrimer as functionalization layer for the BMPs, namely poly-amidoamine (PANAM)[114]. The PANAM functionalized BMPs achieved an extraction efficiency of roughly 85% when elevated elution temperatures are used. Although, functionalization of these beads is time-consuming and labour-intensive[86], the extraction procedure is rather simple. However, the extraction requires typically large volumes of reagents and washing solutions[172]. This make the off-chip magnetic bead method not suitable for portable equipment. The principle of the pH sensitive amine functionalization is already discussed before, so it will not be discussed again.

It is possible to use magnetic particles inside an µSPE chip. Such particles, coated with silica, are used by Reedy *et al.*[173]. These particles need chaotropic conditions in order to extract the DNA from the solution. Achieved extraction efficiencies are in the order of 25% to 30%. In their paper, they also recommend the use of an additional purification step in order to make it more amendable for the integration of a PCR step. This step is based on the chitosan method developed by Cao *et al.*[111]. More information about these and non-related microfluidic purification techniques can be found in the review of Wen *et al.*[75].

1.4 Approach in this thesis research

The approach chosen in this research is based on pH-induced extraction via an ion exchange functionalization inside an etched column. This approach is chosen primarily because of the fact that a complete aqueous based method can be established, removing the use of chaotropic salts and other exogenous PCR inhibitors. Also, this approach has a better fabrication reproducibility when compared to beads-filled columns and monolithic columns. The idea is to design a μSPE column that can extract DNA and subsequently elute it in a plug of aqueous buffer. This buffer plug is the smallest amount of buffer needed to extract the DNA from the column. For this it is necessary to have a straight plug profile inside the column, such that the DNA gets eluted over the whole width of the column, more or less at the same time. This plug profile can be established with the use of a flow distributor before the column. The substrate of choice is a hybrid substrate with a silicon and a silica layer. These substrate are chosen because of their robustness, reproducibility, and available equipment in the MESA$^+$ clean room. A more detailed theoretical description can be found in chapter 2.

Chapter 2

Theoretical aspects

The second chapter of this thesis introduces the reader into all design aspects for the μSPE chip developed in this project. This chapter starts with the theoretical design of the chip. This paragraph is followed by a paragraph about the mathematical aspects of microfluidics and finite element methods-based computational fluid dynamics. Then, a short paragraph about surfactants and their role in water-in-oil emulsions. This theory is related to the buffer plug formation in the oil stream. The chapter closes with a paragraph is dedicated to the used DNA detection method. Measuring low concentrations of DNA is often quite troublesome[174], so it is good to spend a small paragraph on this matter. The choice is made to not discuss the theoretical aspects of the different fabrication steps here, since it is considered basic knowledge. The interested reader who wants more information on this subject can read appendix A.

2.1 Design aspects

The chosen design is a 1 cm long straight column with a width of 300 μm. This shape is chosen in order to eliminate the racetrack effect. Here, band distortion is caused by the fact that the inner portion of a liquid plug is travelling less distance in a turn than the outer portion of the plug. This effect skews the bands, resulting in a more diluted profile in the shape of a parallelogram. These parallelograms eventually form a rectangular shape again due to the collapse of the parallelogram by radial diffusion. This is an additional efficiency loss[175]. A visual representation of this distortion in the concentration is shown in figure 2.1. A more detailed study of this effect and the resulting dispersion model can be found in the paper of Baidya *et al.*[176].

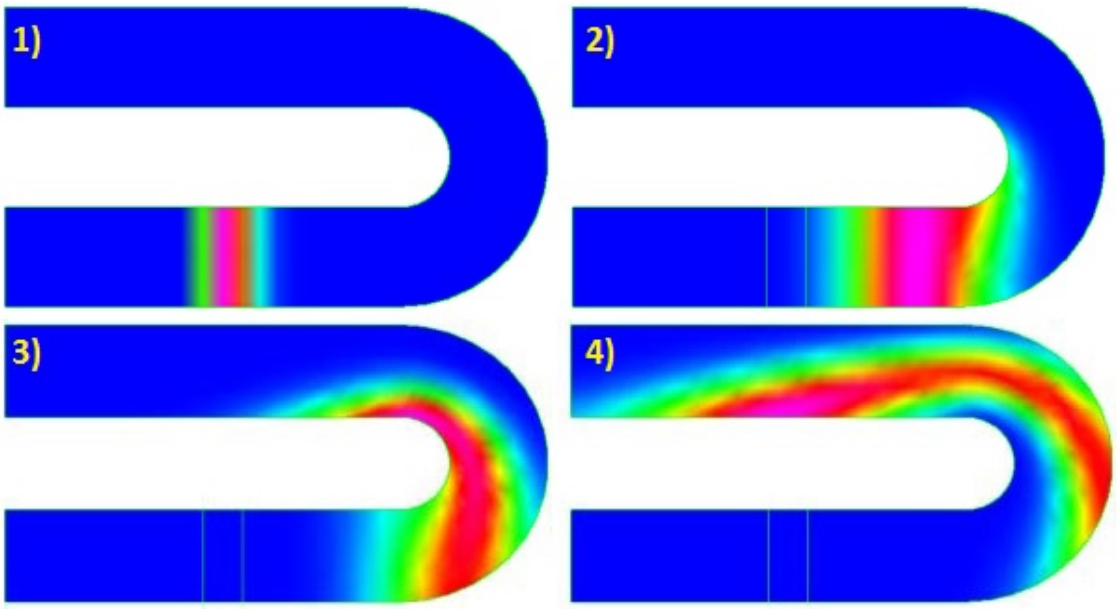

Figure 2.1: Simulated racetrack effect. Picture taken from reference 177.

The designs of the chips are shown in figure 2.2. As can be seen here, there is chosen for a design with 2 and a design with 3 inlets. The chip with 2 inlets can be used for extractions that are not plug-based. One inlet can be used for the DNA solution and the other inlet can be used for the elution buffer.

The chip with 3 inlets has an additional inlet for the oil. The working principle of the chip with 3 inlets is shown schematically in figure 2.3. The chip with 2 inlets works almost the same. This one does not have the oil inlet.

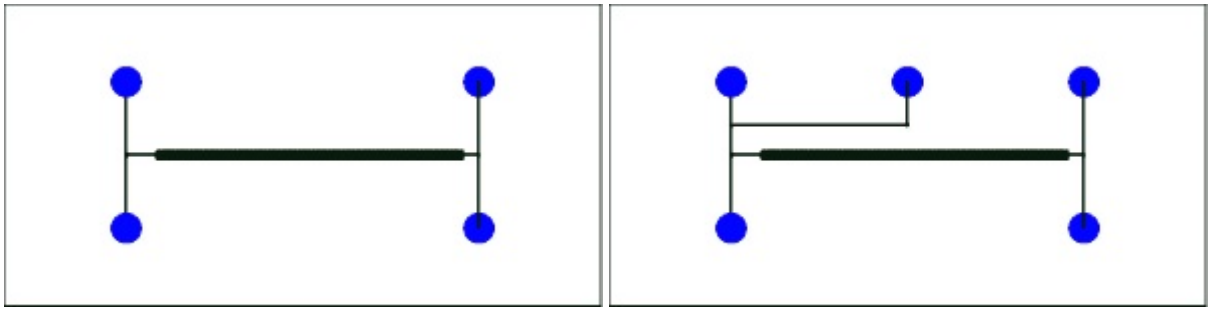

(a) Chip design with two inlets. (b) Chip design with three inlets.

Figure 2.2: Chip designs with two and three inlets.

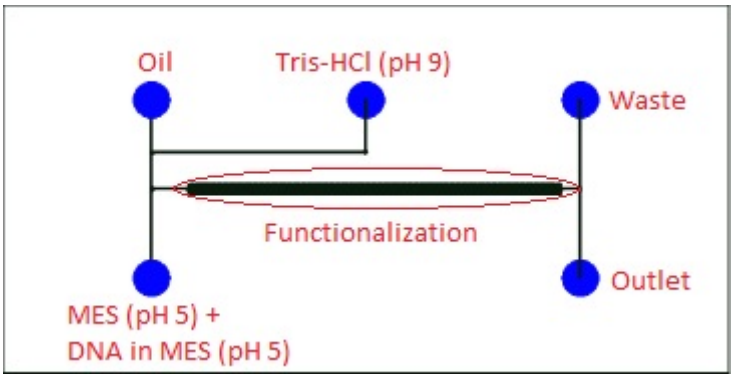

Figure 2.3: Schematic representation of the working principle of the designed chip.

The column is much wider than the inlet channels, as can be seen in the pictures of figure 2.2. The entrance channel before the column and the exit channel after the column have a width of 50 μm. The column itself has a width of 300 μm. This gives a problem with the transition from entrance channel to column. The increase in width disturbs the profile of the liquid, which is really disadvantageous when the DNA needs to be eluted in a plug. The plug will form a parabolic profile as soon as the plug leaves the entrance channel[178]. In order to solve this problem, bifurcating channels are designed[179]. Such a channel is shown in figure 2.4(a). As is visible, the channel divides every time in two new channels and with every separation, the width is divided by 2 in order to maintain a constant flow velocity. The total amount of inlets into the column is 2^n, where n is the amount of separation generations, which is 6 in figure 2.4(a). However, it is proven that these kind of flow distributors do not work optimal. The resulting band of the plug is not completely smooth, having rounded edges and the band volume is also relatively large, meaning longitudinal diffusion[180,181]. This is all due to the large volumes of the channels[178]. Another drawback of the bifurcating channels is their sensitivity to local etch errors or obstructions. When one of the channels is obstructed, the flow resistance will change locally, making that the liquid at that point cannot mix with the liquid in the other channels and therefore it will leave the distributor at a different time than the rest of the liquid[180,181].

Vangelooven *et al.* designed therefore a radially interconnected flow distributor with better performances[181]. Such a flow distributor is also shown in figure 2.4. The band profile of these kind of distributors are proven to be more straight, without rounded edge and they are less sensitive to local etch error or obstructions since all channels are interconnected with each other. Vangelooven *et al.* investigated different aspect ratios and found that an aspect ratio of 15 (axial width of 5 μm and a transversal length of 75 μm) is the best choice for a design with single distributor region[181]. Such flow distributor will be implemented before and after the column.

The designed channel will be filled with pillars in order to increase the surface-area-to-volume (SA-V) ratio. The dimensions for these pillars are 10$\times$10 μm for square pillars and 10 μm diameter for round pillars. The round pillars are put in a more dense geometry and a less dense geometry. Close-ups of the flow distributors and pillar geometry and placement are shown in figure 2.5. The whole masks are

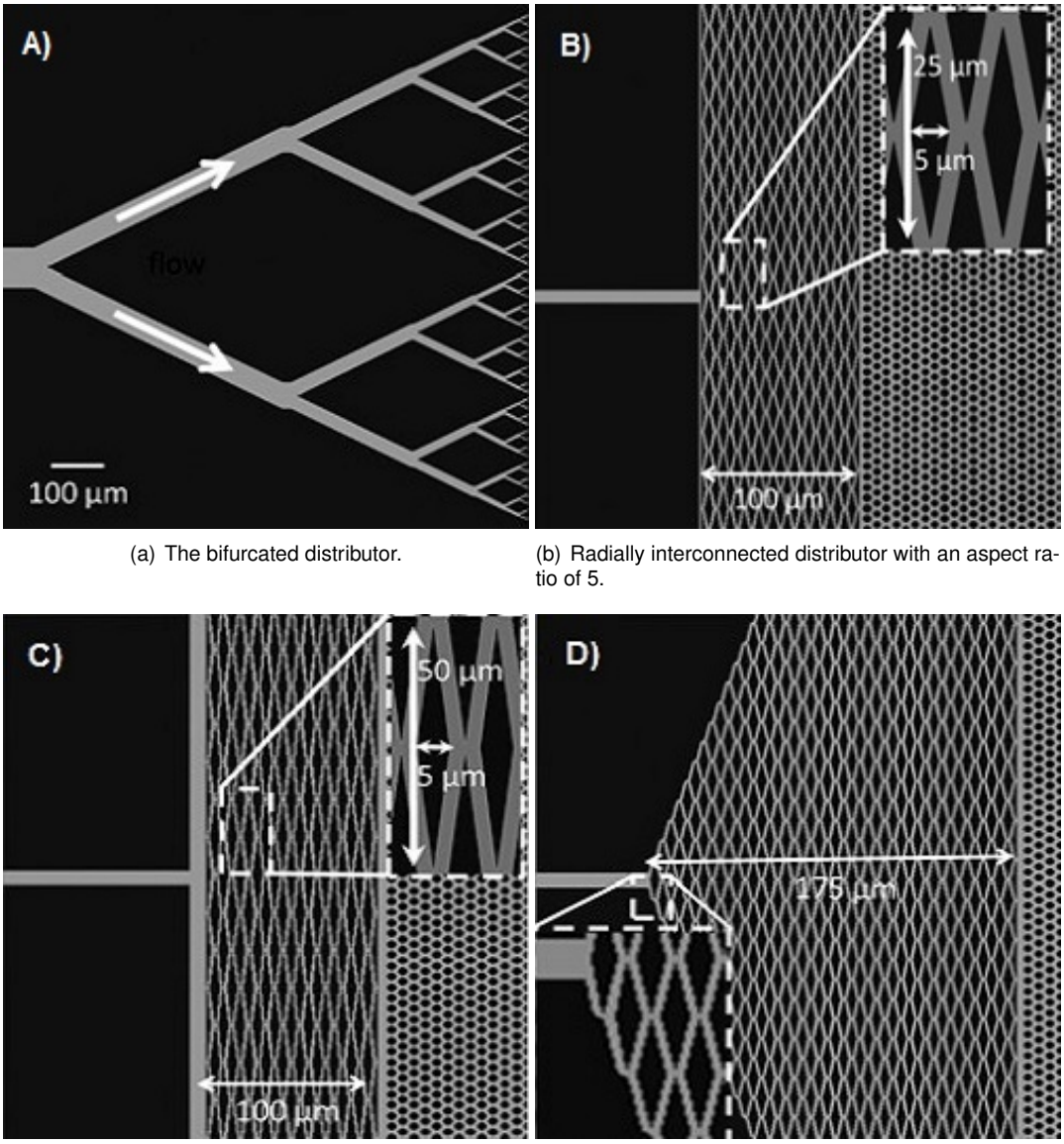

(a) The bifurcated distributor.

(b) Radially interconnected distributor with an aspect ratio of 5.

(c) Radially interconnected distributor with an aspect ratio of 10.

(d) Diverging radially interconnected distributor with an aspect ratio of 5.

Figure 2.4: Different flow distributor designs. Pictures taken from reference 182.

shown in figure B.1(a) and B.1(b) in appendix B.

All channels and column are 25 μm deep, making that the channel area without any columns for a 1000$\times$300μm column is 7 mm^2. Placing pillars in the column will remove a small part of that area (the bottom and top of the pillar), but it will give a significant surface area back (the side of the pillars). These values vary with the different pillar geometries. This leads to an average surface area increase of $\sim$100%. The volume on the other hand will decrease. An empty column has a volume of 0.075 μL. The pillars occupy a certain volume of the column, decreasing the effective volume of the column. A summary of these values, together with the SA-V ratio are shown in table 2.1.

Table 2.1: Channel (ch) and pillar (p) areas (A) and volumes (V).

Array	**# of pillars**	A_{ch} **[mm^2]**	A_p **[mm^2]**	A_{ch+p} **[mm^2]**	**Area increase [%]**	V_{ch} **[μL]**	V_{ch+p} **[μL]**	**SA-V [m^{-1}]**
Square	7,444	7	7.4	12.5	77.9	0.075	0.056	223,214
Round	10,005	7	7.9	12.7	80.9	0.075	0.055	230,909
Round dense	14,985	7	11.8	15.7	124.7	0.075	0.045	348,888

The amino functionalization of the ion exchange SAM on the inside of the column will be done with

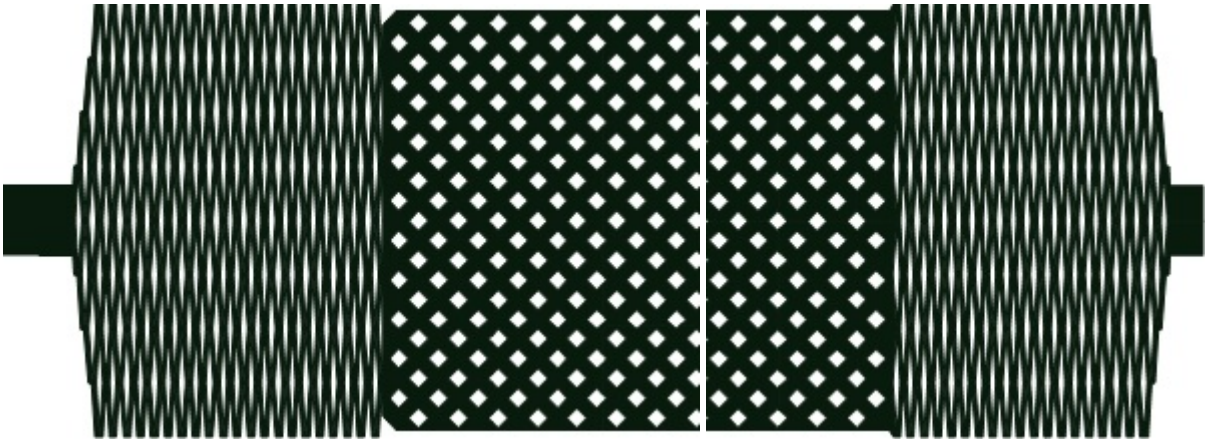

(a) Column design with square pillars.

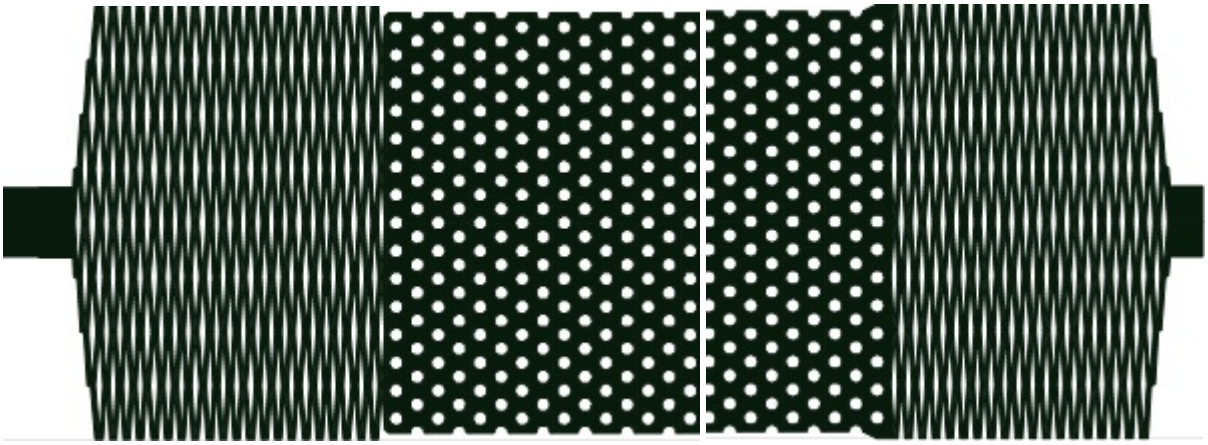

(b) Column design with round pillars.

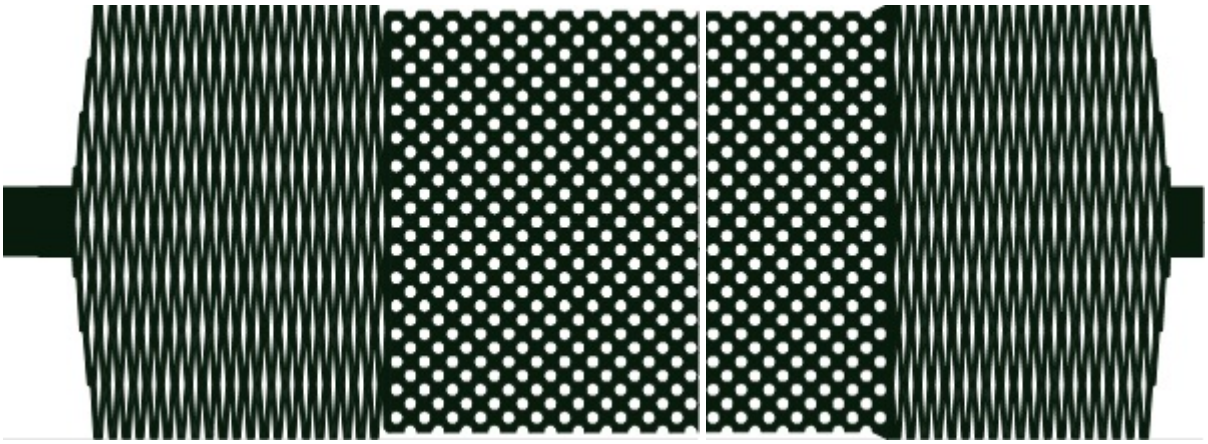

(c) Column design with round and densely packed pillars.

Figure 2.5: Different column designs with square, round, and round and densely packed pillars.

APTES and chitosan. Both molecules are already described in chapter 1 and literature has proven that both functionalizations are suitable for ion exchange μSPE. The protocol for the functionalization is given in chapter 3.

After functionalization with an amino-terminated SAM, the column is prepared by flushing it with a 2-(N-morpholino)ethanesulfonic acid (MES) buffer of pH 5. This buffer will protonate the amino end-groups. Then, DNA dissolved in the same buffer will be flown through the column. The DNA will bind electrostatically with the protonated amino groups. After binding, the channel is flushed with the MES buffer in order to remove any proteins and other contaminants and PCR inhibitors. The next step is the elution step. This will be performed with a tris(hydroxymethyl)methylamine hydrochloride (TRIS, pH 9) buffer plug in an oil stream. The volume of the plug will be determined on basis of the elution profile and is the smallest amount of buffer needed to elute a significant part of the extracted DNA. The operating principle is schematically represented in figure 2.3.

2.2 Theory on microfluidics and computational fluid dynamics

It is important to study the microfluidic structures also theoretically, since all kinds of phenomena exist in the micro- and nanofluidic regime. The microfluidics regime is dominated by low velocity flows with low Reynolds numbers, often in the order of unity or even smaller. This makes the convective terms of the Navier-Stokes equations the most important part of the equation (see below). A consequence of this is that laminar flow is established[26]. Other physical phenomena that can occur in microfluidic channels are described in the review written by Stone, Stroock, and Ajdari[26] and in the book "Theoretical microfluidics", written by Bruus[183].

The Navier-Stokes (NS) equations are equations that describe the mechanics of fluids and are nowadays used as the standard equation for simulating and calculating fluid mechanics. These equations describe the conservation of mass (continuity equation), momentum (impulse equation), and energy for Newtonian fluids*. The NS equations were formulated almost 200 years ago by Navier (1827)[185] and Poisson (1831)[186]. The confirmation of the NS equations came roughly a decade later and was done by Saint Vernant (1843)[187] and Stokes (1845)[188]. The only problem back then was that only a few simple geometries could be solved[183].

A derivation of the NS equations will not be given here because this is general fluid physics and therefore it can be assumed to be basic knowledge. Derivations can be found on numerous places, for example in chapter 6 of "Fundamentals of fluid mechanics" by Munson *et al.*[189]. The result of this derivation is the NS equation in vector format and Cartesian coordinates for irrotational ($\boldsymbol{\nabla} \times \overrightarrow{\boldsymbol{v}} = 0$) flow (all explenations for the used symbols can be found in the beginning of this thesis):

$$\rho \left(\partial_t + \overrightarrow{\boldsymbol{v}} \cdot \boldsymbol{\nabla}\right) \overrightarrow{\boldsymbol{v}} = -\boldsymbol{\nabla} p + \eta \nabla^2 \overrightarrow{\boldsymbol{v}} + \rho \overrightarrow{\boldsymbol{g}} + \rho_{el} \overrightarrow{\boldsymbol{E}} + \overrightarrow{\boldsymbol{f}} \tag{2.1}$$

If we look closer to equation (2.1) we can address the individual terms on the left hand side (LHS) and right hand side (RHS). At the LHS is inertia:

$\partial_t \overrightarrow{\boldsymbol{v}}$	Unsteady acceleration
$\left(\overrightarrow{\boldsymbol{v}} \cdot \boldsymbol{\nabla}\right) \overrightarrow{\boldsymbol{v}}$	Convective acceleration

And on the RHS are the divergence of stress (pressure and viscosity), gravity, and other body forces:

$-\boldsymbol{\nabla} p$	Pressure gradient
$\eta \nabla^2 \overrightarrow{\boldsymbol{v}}$	Viscosity
$\rho \overrightarrow{\boldsymbol{g}}$	Gravity
$\rho_{el} \overrightarrow{\boldsymbol{E}}$	Electrical force
$\overrightarrow{\boldsymbol{f}}$	Other body forces

The beauty of hydrodynamic phenomena is spawned in the non-linear mathematical term of the NS equation ($\rho \left(\overrightarrow{\boldsymbol{v}} \cdot \boldsymbol{\nabla}\right) \overrightarrow{\boldsymbol{v}}$). On the other hand, this non-linear term is also responsible for making the mathematical treatment of this equation a complex and difficult job. But as mentioned earlier, micro- and nanofluidics are dominated by low Reynolds numbers because of the low flow velocities. This limit is highly relevant, making that the non-linear term can be neglected. This is the regime of the so-called Stokes flow or the regime of creeping flow. After neglecting the non-linear term, it is possible to find analytical solutions to flow problems[183,190].

Other terms that can be neglected in this study are the electrical forces and other body forces. This is allowed because a pressure driven flow is used and no other external forces are applied. Gravity can also be neglected, since we are working with minute quantities. This can be demonstrated by taking a microchannel ($h = 25$ μm) and filling this with, for example, water. The pressure created by gravity is:

$$p_g = \rho g h = 1000 \times 9.81 \times 25 \cdot 10^{-6} = 0.245 \text{ [Pa]} = 2.45 \cdot 10^{-6} \text{ [bar]} \tag{2.2}$$

However, the viscosity cannot be neglected and is really important in micro- and nanofluidics. This can be demonstrated with the Reynolds number[191]. This has to be lower than unity, otherwise the inertia will dominate viscosity. As example the channel of 50 μm wide and 25 μm deep is taken. This are the dimensions of the fluidic channels before and after the column, as is described in the first paragraphs of this chapter. A fluid flow of 1 μL min^{-1} is taken:

$$Re = \frac{\rho D_H v}{\eta} = \frac{\rho \frac{2A_{ch}}{P_w} v}{\eta} = \frac{1000 \times \frac{2 \times 1250 \cdot 10^{-12}}{(25+50) \cdot 10^{-6}} \times 0.0133}{1.002 \cdot 10^{-3}} = 0.44 \ll 1 \tag{2.3}$$

*Newtonian fluids are fluids for which the shearing stress is linear related to the rate of shearing strain: $\tau = \eta \left(du/dy\right)$, in which τ is the shearing strain, η is the shear rate, and du/dy is the velocity gradient. This means that their viscosity is independent of the shear rate[184].

The LHS of equation (2.1) contains the continuity equation, which is the material derivative of the density:

$$\frac{D\rho}{Dt} = \partial_t \rho + \left(\boldsymbol{\nabla} \cdot \overrightarrow{\boldsymbol{v}}\right) \rho \tag{2.4}$$

This term can also be neglected because the system is steady state ($\partial_t \rho = 0$) and the fluid is incompressible, meaning mass conservation: mass = volume ($\boldsymbol{\nabla} \cdot \overrightarrow{\boldsymbol{v}} = 0$). All these assumptions simplify the NS equation (equation (2.1)) into the Stokes equation:

$$0 = -\nabla \overrightarrow{\boldsymbol{p}} + \eta \nabla^2 \overrightarrow{\boldsymbol{v}} \tag{2.5}$$

Which can be rewritten because there is a laminar flow ($Re \ll 1$) in the x-direction, which is dependent on y and z:

$$-\frac{\Delta p}{\eta L} = \left(\partial_y^2 + \partial_z^2\right) v_x\left(y, z\right) \tag{2.6}$$

In lab-on-a-chip, and micro- and nanofluidic devices it is common to have microchannels with a rectangular cross-section. These channels can for example be made with deep reactive ion etching (DRIE) of silicon or polymer (for example SU-8 or PDMS) techniques. The channels show often a high degree of symmetry, *i.e.* rectangular cross-section, which can be seen in figure 2.6. Despite of this symmetry, there are no analytical solutions known to the Poiseuille-flow problem in microchannels with a rectangular cross-section. However, it is possible to find a Fourier sum that represents the solution[183]. In the case of a microchannel where the width is larger than the height ($w > h$), the following boundary conditions (BC) can be established[183], where the last one is known as the no-slip BC.

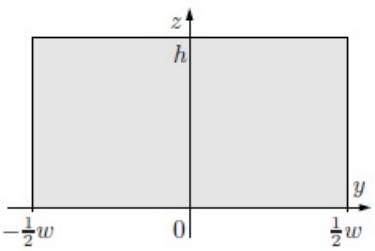

Figure 2.6: Schematic cross-section of a rectangular microfluidic channel, showing its symmetry. Picture taken from reference 183.

BC1 $\quad -\frac{\Delta p}{\eta L} = \left(\partial_y^2 + \partial_z^2\right) v_x\left(y, z\right) \quad$ for $\quad \begin{matrix} -\frac{1}{2}w < y < \frac{1}{2}w \\ 0 < z < h \end{matrix}$

BC2 $\quad v_x\left(y, z\right) = 0 \quad$ for $\quad \begin{matrix} y = \pm\frac{1}{2}w \\ z = 0 \\ z = h \end{matrix}$

The first step in solving the Stokes equation (equation (2.6) for rectangular microchannels is to expand all functions as a Fourier series along the short vertical z-direction. Here we have to use the terms that are proportional to $\sin\left(n\pi z/h\right)$ (where n is a positive integer) in order to fulfil the no-slip BC. The Fourier expansion of the constant on the LHS of BC1 gives us a series containing only odd integers for n:

$$-\frac{\Delta p}{\eta L} = -\frac{\Delta p}{\eta L}\frac{4}{\pi}\sum_{n,odd}^{\infty}\frac{1}{n}\sin\left(n\pi\frac{z}{h}\right) \tag{2.7}$$

And the Fourier expansion of BC2 in the z-coordinate of the velocity gives us a term with coefficients $f_n\left(y\right)$ which are constants in z, but functions in y:

$$v_x\left(y, z\right) \equiv \sum_{n=1}^{\infty} f_n\left(y\right)\sin\left(n\pi\frac{z}{h}\right) \tag{2.8}$$

Now we can combine these expansions (equation (2.7) and (2.8)) and the BCs in order to get a new version of the Stokes equation:

$$\left(\partial_y^2 + \partial_z^2\right) v_x\left(y,z\right) = \sum_{n=1}^{\infty}\left(f_n^{''}\left(y\right) - \frac{n^2\pi^2}{h^2} f_n\left(y\right)\right)\sin\left(n\pi\frac{z}{h}\right) \tag{2.9}$$

A solution of this version of the Stokes equation must satisfy that for all values of n, meaning that the nth coefficient in the pressure term must equal the nth coefficient in the velocity term. Therefore we can establish new BC's:

BC3 $\quad f_n\left(y\right) = 0 \quad$ for $\quad n$ is even

BC4 $\quad f_n^{''}\left(y\right) - \frac{n^2\pi^2}{h^2} f_n\left(y\right) = -\frac{\Delta p}{\eta L}\frac{4}{\pi}\frac{1}{n} \quad$ for $\quad n$ is odd

BC4 is a second order inhomogeneous differential equation, which can be solved via finding the inhomogeneous and homogeneous solutions in order to determine n:

$$f_n\left(y\right) = f_n^{inhom}\left(y\right) + f_n^{hom}\left(y\right) \tag{2.10}$$

Where $f_n^{inhom}\left(y\right)$ is a particular solution to the inhomogeneous equation and $f_n^{hom}\left(y\right)$ is the general solution to the homogeneous equation (RHS is put equal to zero). It is fairly easy to find one particular solution. This solution can be found by inserting the trial function $f_n^{inhom}\left(y\right) = constant$ and solving the resulting algebraic equation for n is odd:

$$f_n^{inhom}\left(y\right) = \frac{4h^2\Delta p}{\pi^3\eta L}\frac{1}{n^3} \tag{2.11}$$

The general solution to the homogeneous equation must satisfy the linear combination:

$$f_n^{''}\left(y\right) - \frac{n^2\pi^2}{h^2} f_n\left(y\right) = 0 \tag{2.12}$$

The solution to the homogeneous equation (2.12) is:

$$f_n^{hom}\left(y\right) = A\cos\left(\frac{n\pi}{h}y\right) + B\sinh\left(\frac{n\pi}{h}y\right) \tag{2.13}$$

Insert in equations (2.11) and (2.12) in (2.10) gives the solution $f_n\left(y\right)$ that satisfies the no-slip BC $f_n\left(\pm w/2\right) = 0$, for n is odd[183]:

$$f_n\left(y\right) = \frac{4h^2\Delta p}{\pi^3\eta L}\frac{1}{n^3}\left(1 - \frac{\cosh\left(n\pi\frac{y}{h}\right)}{\cosh\left(n\pi\frac{w}{2h}\right)}\right) \tag{2.14}$$

Which leads to the velocity field for the Poiseuille-flow in a rectangular channel[183]:

$$v_x\left(y,z\right) = \frac{4h^2\Delta p}{\pi^3\eta L}\sum_{n,odd}^{\infty}\frac{1}{n^3}\left(1 - \frac{\cosh\left(n\pi\frac{y}{h}\right)}{\cosh\left(n\pi\frac{w}{2h}\right)}\right)\sin\left(n\pi\frac{z}{h}\right) \tag{2.15}$$

Equation (2.15) is slightly different than the result of Oosterbroek[190], but this is due to the choice of another origin. He used the centre of the rectangular cross-section as origin for his derivation, as can be seen in figure 2.7. He also left out the physical parameters:

$$v_x\left(y,z\right) = \frac{16\left(0.5w\right)^2}{\pi^3}\sum_{n,odd}^{\infty}\frac{1}{n^3}\left(-1\right)^{\frac{n-1}{2}}\left(1 - \frac{\cosh\left(n\pi\frac{z}{w}\right)}{\cosh\left(n\pi\frac{h}{2w}\right)}\right)\cos\left(n\pi\frac{y}{w}\right) \tag{2.16}$$

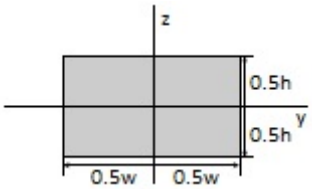

Figure 2.7: Schematic cross-section of a rectangular microfluidic channel, showing the point of symmetry chosen by Oosterbroek. Picture taken from reference 190.

The above mentioned equations are for straight channels. Complex 3D geometries, like turns/meanders, surface corrugations, etc., lead to new questions regarding the detailed flow profile and associated transport properties. Such geometries are not analytically solvable, so numerical methods need to be used. In order to solve these series numerical, computational fluid dynamics (CFD) programs are used.

These programs are based on finite element methods (FEM), meaning that the equations are solved for discrete points in time and space. For this, the model must be discretisised into a mesh, like the one in figure 2.8. The accuracy of the solution depends on the resolution of the chosen mesh, but this resolution (and the scale and complexity) also determines the needed computational power. Modern computers have enough power, which allows them to be used for solving NS equations for geometries of moderate to high complexity[180]. There are different CFD programs available on the market. The one chosen here is COMSOL Multiphysics 4.3b (Burlington, MA, United States) with the creeping flow physics package. The modelling temperature of the fluid in the channel is set at 293.15 K. Other physical parameters, like density and viscosity are set equal to the ones of water. So a density of $\rho = 1000$ kg m^{-3} and a viscosity of $\eta = 10^{-3}$ Pa s is used in the computations. These assumptions are valid for this project because the used buffers are all aqueous solutions. However, a plug-based system uses also an oil. The viscosity of oils is often higher than the viscosity of water, making the pressure drop to increase. This is visible in equation (2.17)[192], where the pressure drop for rectangular channels ($w \ll h$) is given. But it is decided that no effort is put into simulating an plug-based system because the focus of this project are not the simulations but the experimental part and the first experiments are done without the use of an oil.

$$\Delta p = R_{hyd} Q \qquad \text{with} \qquad \frac{1}{R_{hyd}} = \frac{w^3 h}{12 \eta L} \left(1 - \frac{192}{\pi^5} \frac{w}{h} \times \sum_{n,odd}^{\infty} \frac{1}{n^5 \times \tanh\left(n\pi \frac{h}{2w}\right)} \right) \tag{2.17}$$

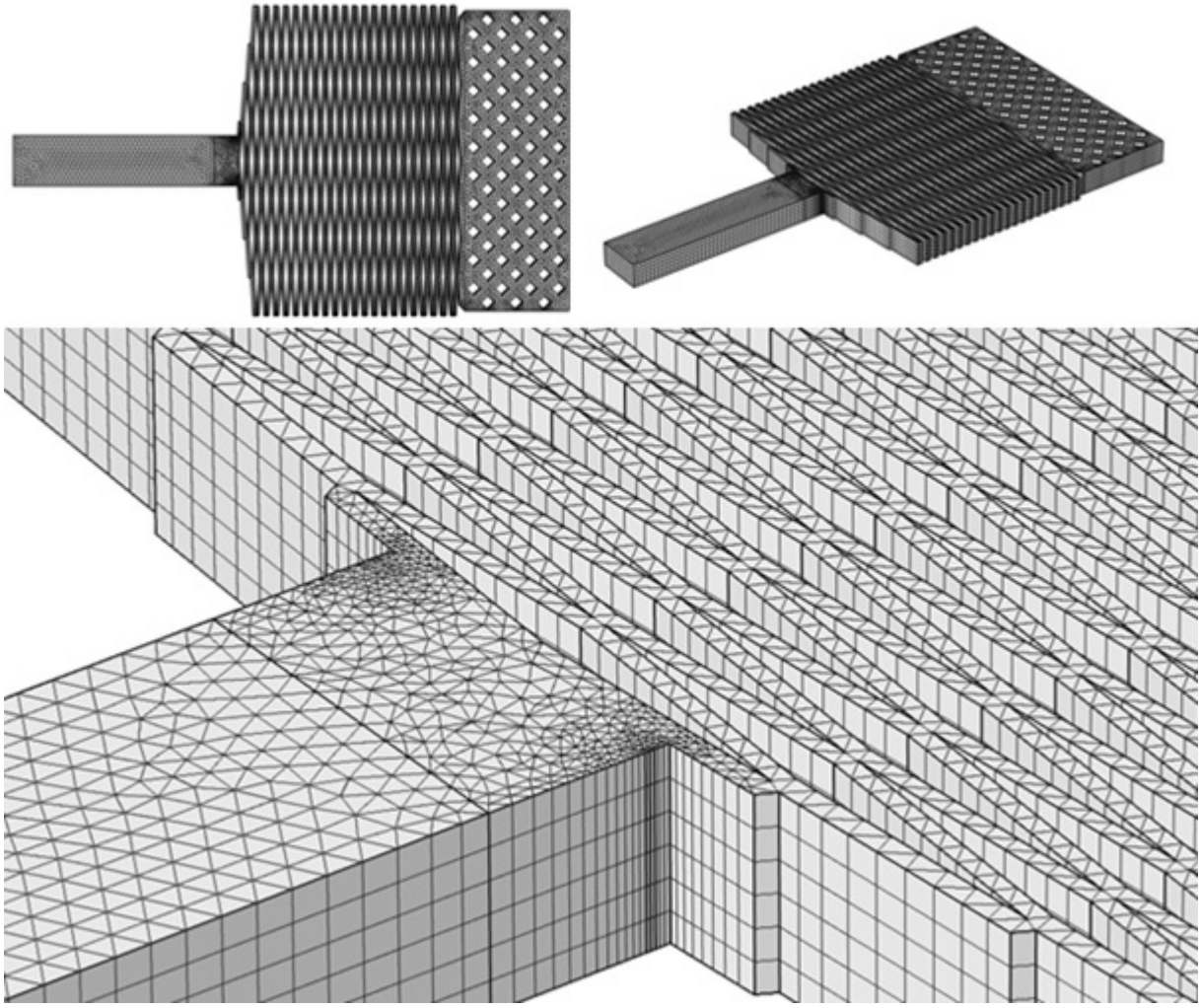

Figure 2.8: A discretisised microfluidic structure made in COMSOL Multiphysics 4.3b.

The creeping flow physics package also needs an hydrodynamic entrance length. This length can be neglected because the well-accepted equation for the hydrodynamic entrance length for laminar flow in rectangular microchannels (shown in equations (2.18)[193]) evidences that L_H is small.

$$L_H = 0.05 D_H Re \qquad \text{with} \qquad D_H = (4A_{ch})/P_w = 2hw/(h+w) \tag{2.18}$$

For rectangular microchannels of 25 μm deep and 50 μm wide, and assuming the Re of equation (2.3) this means:

$$L_H = 0.05 \times \frac{2hw}{h+w} \times Re \approx 7.33 \cdot 10^{-7}[\mu\text{m}] \tag{2.19}$$

The hydrodynamic entrance length is only 0.1 pm (as can be seen in equation (2.19). This is of no significance since the channel and column lengths are in the order of 10 to 100 μm. Therefore it also does not matter if the hydrodynamic entrance length is set at 1 μm, since the channels are at least an order of magnitude longer. Besides these assumptions, the assumption of no-slip is made in the simulations.

2.3 Emulsions

Emulsions are mixtures of two or more immiscible liquids with a clear interface between the different liquids. Generally, an emulsion has an aqueous phase (water for example) and an oil phase[194]. These kind of emulsions can be naturally divided into two possibilities, a water-in-oil (W/O) emulsion and an oil-in-water (O/W) emulsion. The behaviour of such a mixture can be described by dimensionless numbers. These dimensionless numbers give a comparison between the importance of different physical parameters of the fluids. The first number is the Reynolds number (equation (2.20)). This number compares inertia with viscous forces. In microfluidics $Re \ll 1$, making viscosity the dominant force.

$$Re = \frac{\rho D_H v}{\eta} \tag{2.20}$$

The second number is the Bond (Bo) number or Eötvös number (Eo) (equation (2.21)) and compares the gravitational forces and surface forces. A Bo of below unity ($Bo \ll 1$ means that gravity effects can be ignored, which is generally the case in microfluidics.

$$Bo = Eo = \frac{\Delta\rho g D_H^2}{\sigma} \tag{2.21}$$

The third dimensionless number is the Weber number (We). This quantity compares inertial forces and surface forces, as can be seen in equation (2.22). Again, in microfluidics it is often the case that $We \ll 1$, making inertia negligible again.

$$We = \frac{\rho v^2 D_H}{\sigma} \tag{2.22}$$

From this all it follows that inertia is unimportant in microfluidics for most of the cases. Interfacial and viscous forces are the leading forces in determining the behaviour of a fluid on the micrometre scale. There are some cases in which inertia plays a significant role. Examples are high-speed flows and the moment of droplet breakup[195]. When the interfacial and viscous forces are compared, the dimensionless capillary number (Ca) can be established, as can be seen in equation (2.23). For this, the viscosity of the most viscous fluid has to be taken.

$$Ca = \frac{\eta v}{\sigma} \tag{2.23}$$

The interfacial tension reduces the interfacial area and this is important for both the droplet formation and subsequent stability. However, the viscous forces tend to extend and stretch the interfacial area in many different flow situations[195]. If Ca is below unity, the interfacial forces play the dominant role and spherical droplet are formed. If Ca is above unity, the viscous forces dominate and deformed droplets are formed or sometimes asymmetric droplets can be formed. It is even possible to get a stratified flow at high Ca numbers[196]. However, these equations are for two continuous flows of liquid. In this research two alternating flows are used to form the buffer plug. The oil flow is stopped, after which the TRIS buffer is started. This flow is stopped again when the plug contains enough buffer, at which moment the oil flow is started again to transport the buffer plug to the column. Therefore, the given equations are not directly useable for this system, but they give a rough idea of how easily the plug is formed.

The techniques for droplet formation can be divided into two categories, active and passive[197]. The first category uses activated external fields on places where droplets need to be formed (electrowetting)[198,199]. This category is beyond the scope of this report, so it will not be discussed here. The passive method does not require the use of an applied external field. This method produces an uniform and evenly spaced stream of droplets. The polydispersity† of the droplets can be as small as 1-3%[195,197]. The two most used passive structures to create a continuous stream of droplets are

† The standard deviation of the size distribution divided by the mean droplet size.

T-junctions, introduced by Thorsen *et al.*[200], Y-junctions, studied by Steegmans *et al.*[201–203], and flow focussing geometries (Ψ-junctions), introduced by Anna *et al.*[204] and Dreyfus *et al.*[205]. In general, both work with two independently driven pressure-driven flows of fluid. The dispersed phase is brought into a carrier fluid. At the point where the two flows meet (at the junction), the interface is deformed. This deformation is dependent on the junction geometry[206,207], the flow rates[200], the flow ratios[208,209], viscosities[210–212], and possible present surfactants[213]. In a T-junction, the two flows can meet each other via two orthogonal channels[200] or via one channel from opposite directions[214]. The Y-junction combines the two liquids at the two diagonal channels[201–203]. The flow focussing device uses three inlet channels, one for the dispersed phase and two for the carrier liquid. These channels are combined into a main channel *via* a narrow orifice. The pinch-off of the droplets, which occurs due to a free surface instability, can be seen as a competition between viscous forces, which deform the liquid interface, and the the capillary (interfacial) forces, which try to resist the deformation. Exactly this competition is expresses by Ca.

2.3.1 Surfactants

As mentioned above, surfactants can be added to emulsions[213]. Surfactants (abbreviation for surface active agents) are amphiphiles, molecules that interact with both polar and non-polar solvents. In the case of emulsions, these surfactants are called emulsifiers. They have a hydrophilic, polar head group that interacts strongly with polar solvents, often via hydrogen bonds, and a hydrophobic (oleophilic) tail that favours interaction with non-polar solvents. This makes that these molecules are preferably adsorbed the interface between a water–vapour interface, a water–oil interface, or a polar–non-polar interface[194]. Once at the interface, surfactants play two roles in the emulsion[46]. Firstly, they reduce the interfacial tension and secondly, they reduce droplet coalescence. The first role facilitates the droplet deformation and rupture, while the second role ensures droplet stability. More in-depth information about emulsions and their stability can be found in the excellent review with the applicable name "Emulsions: basic principles", written by Bibitte *et al.*[46]. The working principle of surfactants in emulsions is shown schematically in figure 2.9.

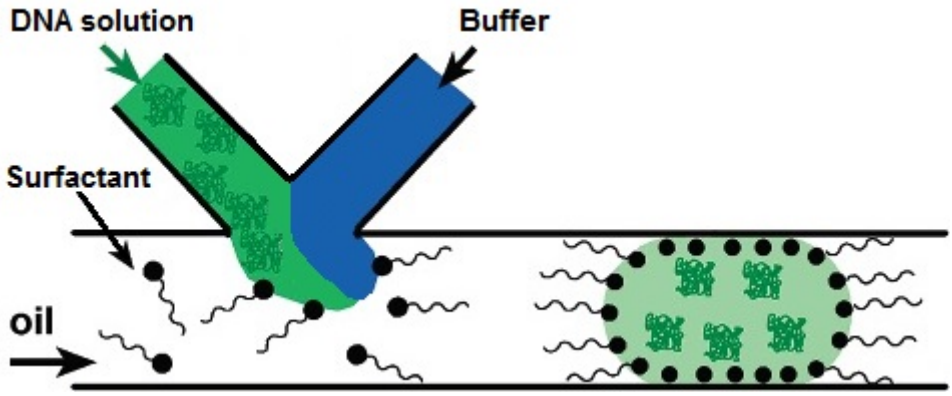

Figure 2.9: Schematic of surfactant molecules at the interface of an aqueous plug in a microfluidic channel. Picture modified from reference 215.

There are four classes of surfactants: anionic, cationic, zwitterionic, and non-ionic. The main difference between these different classes is the electric charge of the hydrophilic head group. Anionic surfactants have a negative charge as head group, like sulphates, sulfonates, phosphates, and carboxylates. Cationic surfactants have a positive charge, like amines and ammonium cations. The class of zitterionic surfactants have both a positive and negative charge in the head group. Examples of this class are molecules where amines/ammonium cations are combined with sulfonates, sultaines, betaines, and phosphates. Non-ionic surfactants have a neutral head group. Common used examples are fatty alcohols with a C_8 to C_{20} chain as hydrophobic tail[216]. A schematic representation of the different classes is shown in figure 2.10. The surfactants that are chosen for this research are non-ionic because of the electrostatic-based DNA extraction. Anionic, cationic, and zwitterionic surfactants have electrical charges in their molecules.

2.4 DNA detection

Fluorescence is the method of primary interest because of the ease of detection and broad range of dyes and methods available. These dyes can be divided into different classes, which are shown in figure 2.11. Intercalating dyes are of interest for easy DNA detection since they "react" (go into the

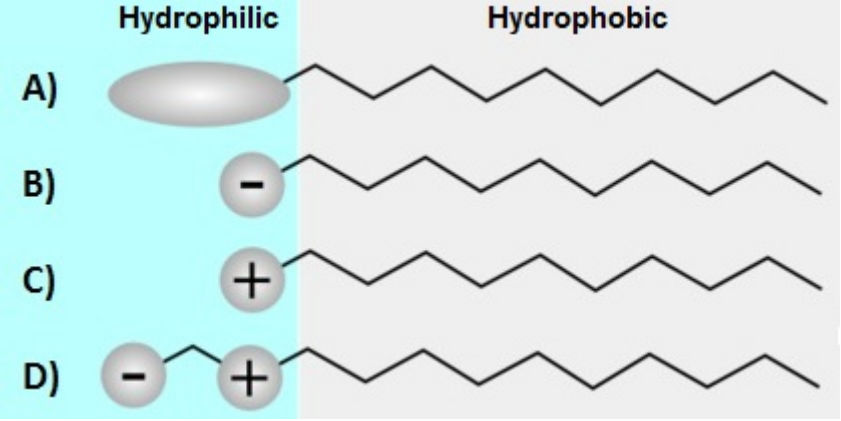

Figure 2.10: Schematic representation of the different surfactant classes, with A) non-ionic, B) anionic, C) cationic, and D) zwitterionic. Picture taken from reference 217.

spaces between the base pairs) easily and they do not need any PCR step to incorporate them into the structure. There is little known about the involved chemistry of intercalation[218], but the fact that they can bind between every base pair makes them the most interesting dye for the quantitation of low DNA concentrations.

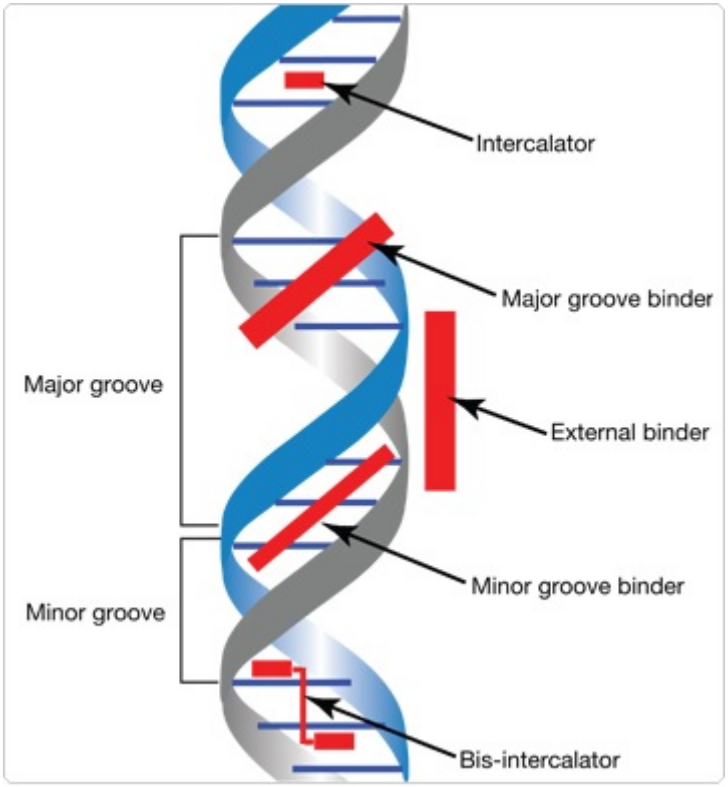

Figure 2.11: Schematic representation of the different fluorescent dyes available for DNA detection. Picture taken from reference 219.

However, in general it is quite difficult to measure low concentrations of DNA accurately with fluorescence. Low concentrations of DNA do not show linear behaviour when measured with fluorescence[174]. This nonlinear behaviour was recently again demonstrated by Bruijns in the Mesoscale Chemical Systems research group of the MESA$^+$ Institute for Nanotechnology. These results are not published, but a graph is kindly made available by Bruijns and shown in figure 2.12. The measurements are done on a Tecan Infinite 200 Pro microplate spectrophotometer with 1.0X Evagreen as fluorescent dye (100 μL 2.0X EvaGreen and 100 μL DNA solution). The extinction is done at 500 nm and the emission is measured at 530 nm. This EvaGreen dye is, together with SYBR Green the most widely used fluorescent dye for DNA quantitation.

The most easy DNA detection method is an off-chip method, which does not need to be incorporated into the chip. This simplifies the fabrication process significantly. This choice is made because a proof-of-principle of the chip needs to be shown, so the focus is not on on-chip detection.

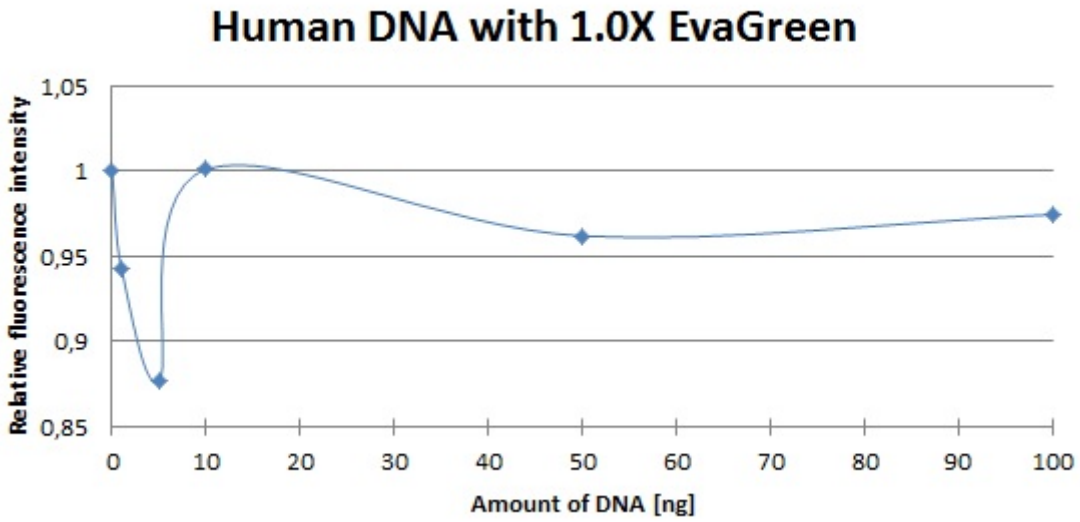

Figure 2.12: Low amounts of DNA measured with a Tecan Infinite 200 Pro spectrophotometer and 1.0X EvaGreen. Excitation is done at 500 nm and emission is measured at 530 nm.

The used detection method is the Qubit high sensitivity dsDNA assay kit with the Qubit fluorometer of Invitrogen. This especially formulated assay kit comes with ready-to-use dilution buffer solution, concentrated assay reagent solution with fluorescent dye (SYBR 32 in DMSO[220]), and pre-diluted DNA solutions (one of 0 ng/μL and one of 10 ng/μL). The measurements are as easy as following the next steps (a complete protocol can be found in appendix D):

1. Dilute the reagent with the provided buffer;
2. Add the sample (any volume between 1 and 20 μL);
3. Incubate for 2 minutes;
4. Measure the concentration with the Qubit fluorometer.

The most significant advantage of this set is its linearity and selectivity[219]. UV absorbance based quantitation cannot be used for mixtures of DNA and RNA, where the Qubit assay can quantitate DNA and RNA separately in a mixture of both with the use of the Qubit DNA assay kit and Qubit RNA assay kit, respectively. This selectivity is shown in figure 2.13.

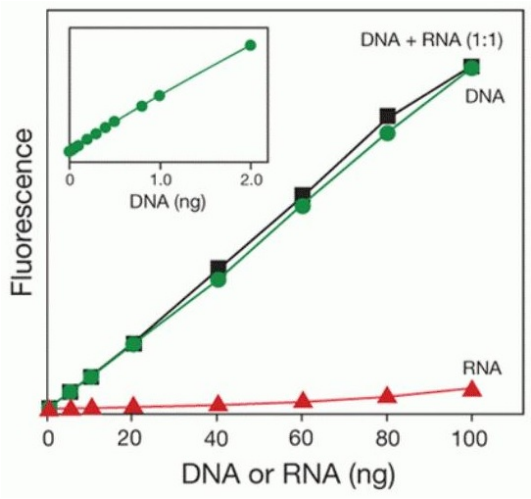

Figure 2.13: Performance of the Qubit dsDNA HS assay, showing its linearity in the range of 0.2-100 ng and selectivity for DNA, even in the presence of an equal mass of RNA. Picture taken from reference 221.

The Qubit HS dsDNA assay kit has a linear signal in the initial sample concentration range of 10 pg μL^{-1} to 100 ng μL^{-1}. The Qubit fluorometer gives values in µg mL^{-1} or ng mL^{-1}. This corre-

sponds to the concentration after dilution of the sample into the assay tube. The initial concentration ($[DNA]_{initial}$) in ng/mL can be calculated with equation (2.24). In this equation, the $QFvalue$ is the value given by the Qubit fluorometer and $V_{pipetted}$ is the number of microliters of sample added to the assay tube.

$$[DNA]_{initial} = QFvalue \times \frac{200}{V_{pipetted}} \tag{2.24}$$

The assay kit tolerates common contaminants, like salts, free nucleotides, solvents, detergents, and proteins. The assay signal is also stable up to three hours[219]. These advantages increase the ease of handling larger sample sets.

Chapter 3

Methodical

The chips are fabricated with different standard clean room techniques. The main steps are, in chronological order, wet oxidation, photolithography, reactive ion etching of the silicon oxide, directional DRIE (BOSCH process) of silicon, anodic bonding, and dicing. Then, the channels are functionalized with an amino termination via chemical surface modifications. The chips are ready to be used for the extraction, once the functionalization step is done. The extraction of DNA is analysed with the previous described Qubit dsDNA HS assay kit of Invitrogen. In the following paragraphs, global information about each of these steps is given. More detailed information can be found in appendix C and appendix D.

3.1 Fabrication process overview

The process flow with the fabrication steps of the chips consists of several standard clean room steps. These steps are, in chronological order, wet oxidation, photolithography, reactive ion etching (RIE) of silicon oxide, directional BOSCH DRIE of silicon, anodic bonding, and dicing of the silicon/borofloat stack into individual chips. A global overview of these steps with a cross section of the chip is given below. The cross-sections are made with CorelDRAW X6 (Corel Corporation, Ottawa, ON, United States). A detailed process flow, with the used equipment and parameters can be found in appendix C. In the clean room, Q-BASF sulphuric acid (96% VLSI Selectipur) and hydrogen peroxide (31% VLSIn Selectipur) are used.

3.1.1 Front side processing

Selection of a $<100>$ DSP Si DSP wafer

Standard cleaning

Wet oxidation

Dehydration bake

Primer spinning

	Photoresist spinning
	Alignment Exposure
	Development Quick dump rinsing Drying
	RIE of SiO_2
	DRIE (BOSCH) of Si
	Resist and primer stripping in O_2 plasma Piranha cleaning Quick dump rinsing Drying

3.1.2 Backside processing

	Dehydration bake Primer spinning
	Photoresist spinning

	Alignment Exposure
	Development Quick dump rinsing Drying Postbake
	RIE of SiO_2
	DRIE (BOSCH) of Si
	Resist and primer stripping in O_2 plasma Piranha cleaning Quick dump rinsing Drying
	Oxide stripping in 50% HF Quick dump rinsing Drying

3.1.3 Cover wafer processing

	Selection of Borofloat BF33 500 μm glass wafer
	Standard glass cleaning Quick dump rinsing Drying

Manually aligning

Prebonding

Anodic bonding

Applying UV dicing foil

Dicing

Flood exposure

Removing dicing foil

3.2 Micro world to macro universe a.k.a. fluidic coupling

During functionalization and extraction the chip is placed in a home-made chip holder (see figure 3.1). This chip holder also made it possible to connect the chip to the macro world. For this Upchurch Scientific NanoPort (IDEX Health & Science, Oak Harbor, WA, United States) connectors and capillaries of 50 μm I.D. and 360 μm O.D. from the Polymicro Technologies company (Phoenix, AZ, United States) are used. The capillaries are connected to the chip with F-123H polyether ether ketone (PEEK) fittings and N-123-03 perfluoroelastomer ferrules. The connection between the capillaries and syringes are made with P-662 Luer-to-MicroTight adapters. As mentioned before, the flow direction of the liquids in the chip is managed with off-chip valves. These valves are 1-way (EW-30600-00) and 4-way (EW-30600-04) male lock polycarbonate stopcocks from Cole-Parmer (Vernon Hills, IL, United States). The connection between the capillaries and the valves is made with P-656 Male Luer to 10-32 Female adapters, P-662 Luer-to-MicroTight adapters, and F-120X fingertight fittings (all of Upchurch Scientific).

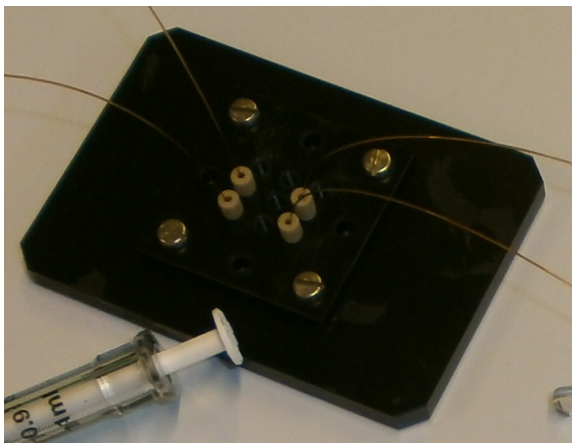

Figure 3.1: Photograph of the used homemade chipholder with connections for capillaries.

3.3 Functionalization

The functionalization starts with a cleaning and activation step. This is done with piranha solution. The standard recipe that is commonly used in (surface) chemistry and microfabrication consists of three parts sulphuric acid (Sigma-Aldrich, ACS reagent, 95.0-98.0%) and one part hydrogen peroxide (Sigma-Aldrich, Perdrogen, puris. p.a., 30 w/w %). This solution is brought into the chip via a home-made vacuum system, consisting of a Pyrex Bernoulli pump, Pyrex Drechsel gas trap, and polytetrafluoroethylene (PTFE) tubing. After cleaning and activation, the chips are rinsed with Milli-Q DI water, which is also brought into the chip with the vacuum system. After this, the functionalization is performed. All steps below use disposable 1 mL syringes with Luer-Lok (BD, Franklin Lakes, NJ, United States) and a Microdialysis CMA 120 syringe pump (Kista, Sweden) to bring the solutions into the chips.

The APTES functionalization of the column is done via standard surface chemistry methods. The APTES (Sigma-Aldrich, 99%) solution is made in ethanol (Merck, ACS, ISO, Reag. Ph Eur, Absolute) or dry toluene (Sigma-Aldrich, Chromasolv Plus, for HPLC, $\geq$ 99.9%). The toluene is dried with a 3 Å

molecular sieve (Sigma-Aldrich, pellets). Both solutions were 4 v/v %. The channels are functionalized by bringing the solution into the chip with a flow rate of 2 μL min^{-1}. The flow is stopped once the channels are completely filled. The functionalization lasted four hours and after every hour a new solution is brought into the channels with a flow rate of 0.5 μL min^{-1}. This low flow rate is used in order to minimize the induced shear stress on the newly formed monolayer of APTES. After four hours, the channels are flushed with ethanol or dry toluene, depending on the APTES solution, at a flow rate of 2 μL min^{-1}. Then, the channel is flushed with isopropanol (Sigma-Aldrich, 100%). This step is done with a flow rate of 2 μL min^{-1}. Subsequently, the chip is dried on a hotplate on 85℃ for 30 minutes.

The chitosan functionalization is done by first functionalizing the channel with the linker molecule GPTMS (Sigma-Aldrich, $\geq$98%). A solution of 0.5 v/v % is made in hexane (Sigma-Aldrich, Chromasolv, for HPLC, $\geq$ 95%) and brought into the channels with a flow rate of 2 μL min^{-1}. This functionalization also lasted four hours and after every 30 minutes new solution is brought into the channels with a flow rate of 0.5 μL min^{-1}. Then, the channels are flushed first with hexane and secondly with 0.1 M acetic acid (Sigma-Aldrich/Fluka Analytical, volumetric, 0.1 N), both at a flow rate of 2 μL min^{-1}. Then, a chitosan solution of 0.5 w/w % in 0.1 M acetic acid is brought into the channel with a flow rate of 0.5 μL min^{-1}. This solution is let to react for 20 hours (overnight), with bringing in new solution after 3, 15, and 18 hours after first bringing in the solution. After these 20 hours, the channels are flushed with 0.1 M acetic acid at a flow rate of 2 μL min^{-1}. Finally, the channel is flushed with isopropanol (Sigma-Aldrich, 100%) at a flow rate of 2 μL min^{-1} and the chip is dried on a hotplate on 85℃ for 30 minutes.

3.4 Extraction

Once the functionalization is finished, the chips are ready for the extraction. The amino groups on the silica surface are first protonated with a MES (Fisher BioReagents) buffer of pH 5. This buffer is flushed through the channels with a flow rate of 2 μL min^{-1}. This is done for only one minute, since the protonation of amino groups is instantaneous[222,223]. Then, a solution of DNA in the MES buffer is flowed through the channels with a flow rate of 2 μL min^{-1}. After flowing everything through the column, the valve is changed to solely the MES buffer and the channel is washed with this buffer at a flow rate of 2 μL min^{-1} for removing RNA, proteins, and other contaminants. Then, the DNA is eluted from the channel. This is done with a plug of TRIS (Fisher Chemical) buffer of pH 9.2 in a low viscosity oil. The volume of this plug will be determined by the elution profile of the chip. The elution step is started by closing the valve of the DNA solution and the MES buffer completely, while opening the oil valve. The oil flow is also set at 2 μL min^{-1}. This valve is closed again, once the oil reaches the column. At this point, the TRIS valve is opened in order to inject the TRIS buffer into the oil stream. This is done with a flow rate of 0.5 μL min^{-1}. This low flow rate is based on the equation for the capillary number (equation (2.23)). From this equation it is clearly visible that a low flow rate is advantageous for the formation of a well-defined plug. This valve is closed again after injecting the desired amount of TRIS buffer into the oil stream. Then, the oil valve is opened again and the plug is transferred to the column with a flow rate of 2 μL min^{-1}. The order of opening the valves is shown in figure 3.2. This plug elutes the DNA from the column and transfers it further to a downstream technique for amplification, for example PCR. This outlet and the waste outlet are also controlled with off-chip valves. The DNA that will be used for these experiments is personal DNA obtained via the Chelex isolation method (see chapter D for the protocol). This method not only lyses the cells, but also purifies the DNA[74]. The only disadvantage of this extraction technique is the fact that it produces single stranded DNA. Therefore it is only suitable for PCR-based testing procedures[74].

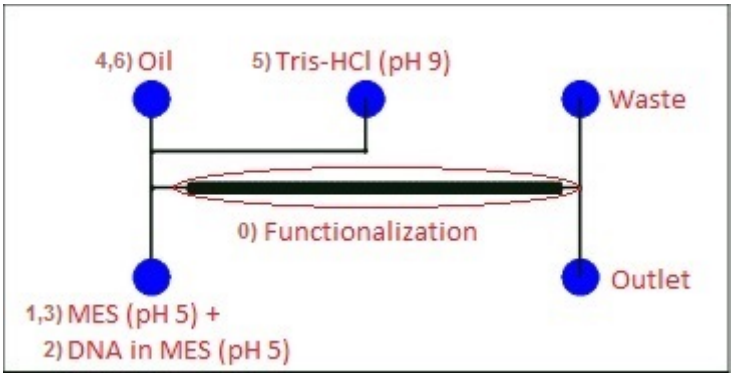

Figure 3.2: Schematic representation of the order of opening the valves. One valve is open at any given moment. As soon as one opens, the previous opened one closes.

3.5 Analysis method

The analysis of the extracted DNA is done with the Qubit dsDNA HS assay kit, the 500 μL thin-walled polypropylene assay tubes, and the Qubit fluorometer of Invitrogen (Carlsbad, CA, United States), as mentioned in the previous chapter. This kit requires a sample volume of anything in between 1 and 20 μL. This is filled to 200 μL with the working solution, which is made by combining the reagent and buffer of the assay kit in a 1:200 ratio. The fluorometer is calibrated with the two standards of the assay kit and after doing this, the samples can be measured. The working principle of this fluorescence method is schematically depicted in the flowchart of figure 3.3.

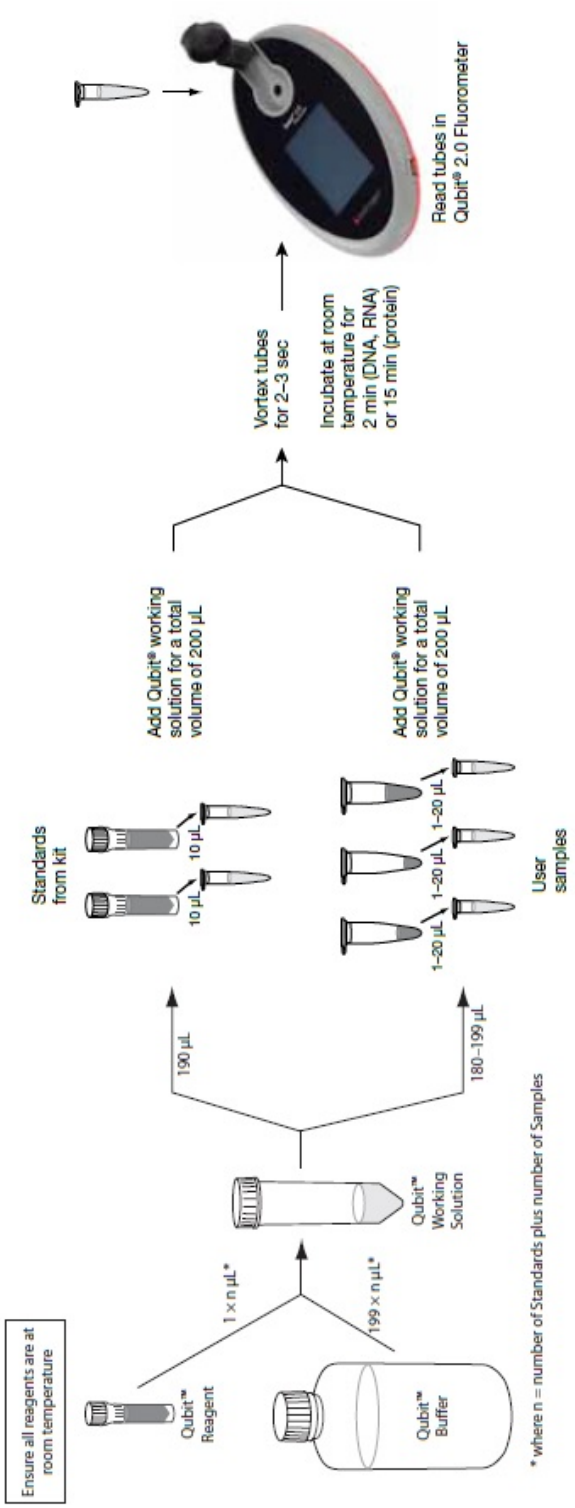

Figure 3.3: Work flow of the Qubit dsDNA HS assay kit. Picture taken from references 224 and 225.

Chapter 4

Results and discussions

In the now following paragraphs, the results of this research are discussed. The results are divided into different sections. First of all the results of the COMSOL simulations are discussed in the paragraph about CFD results. Then, results of the fabrication process are discussed. During the whole fabrication process, different techniques are used in order to monitor and check the different steps. After the fabrication process comes the functionalization of the chip. Different test methods are used in order to determine the best approach, and the results of these tests are discussed in the third paragraph of this chapter. The fourth paragraph discusses the results of the extraction, which are obtained with the Qubit dsDNA HS assay kit.

4.1 Computational fluid dynamics

In order to determine the best geometry of the column, COMSOL Multiphysics 4.3b is used. With this FEM software package, CFD analysis can be performed. The first analysis that is done was the determination of a good pillar geometry and orientation. Different geometries, namely square and round pillars, and different orientations of the squares, namely with the flat side perpendicular to the flow and the corner directed towards the flow direction. Besides this, the placement of the pillars is also investigated. Some are placed in a line grid, while others are placed in a hexagonal grid. An overview of the simulated pillars is shown in figure 4.1. Results of these analyses are shown in appendix E. The pitch of the square micropillar array is chosen to be 28.28 μm in both directions, the pitch of the round micropillars is 30 μm in the x-direction and 20 μm in the y-direction, and the pitches of the denser packed array with round micropillars is 20 μm in both directions. The hexagonal packed arrays have micropillars on the half of the pitches, and elevated by 45°. The pictures in figure 4.2 show the best results for the 3 different kind of pillar arrays. A flow rate of 1.0 μL min^{-1} is used for these simulations.

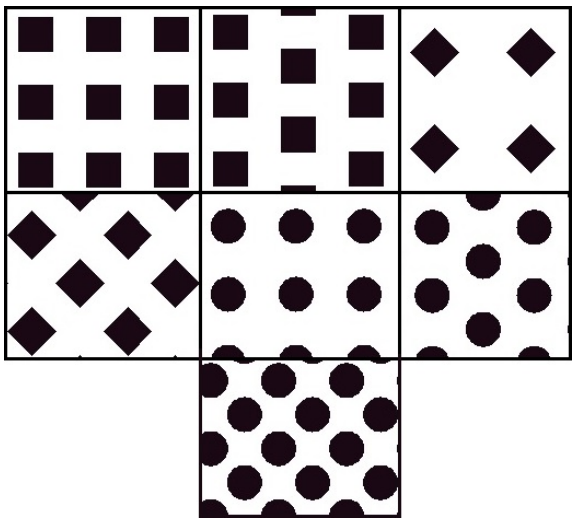

Figure 4.1: Overview of the different simulated pillar geometries. In these figures, the flow is going from the left to the right.

As can be seen in the results in figure 4.2, the hexagonal packing of micropillars shows the best results in terms of constant flow velocity. However, a higher velocity is observed in the spacing near the

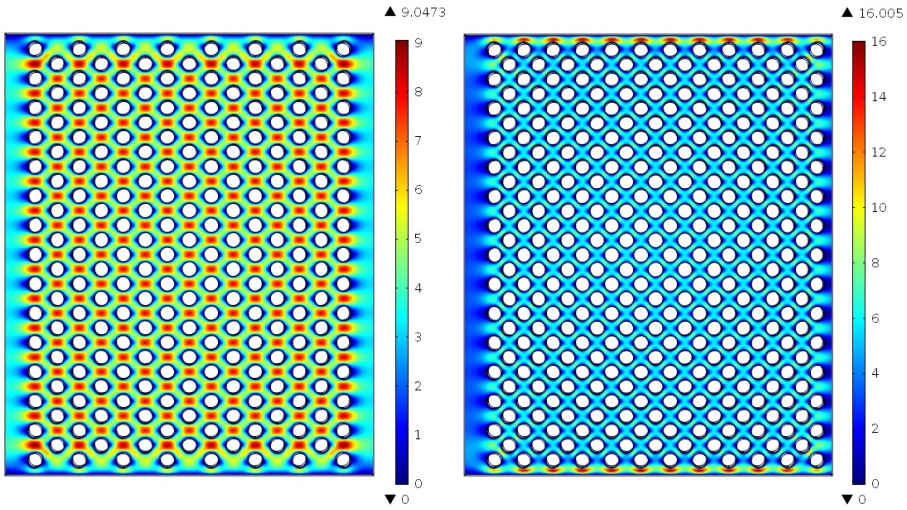

(a) Round pillars that are placed in a hexagonal grid.

(b) Denser packed round pillars that are placed in a hexagonal grid.

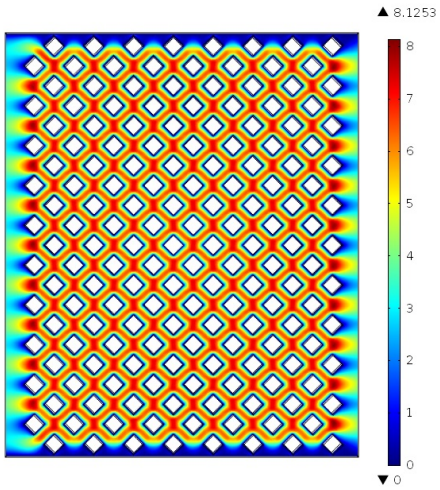

(c) Square pillars, corner directed to the flow and placed in a hexagonal grid.

Figure 4.2: Velocity profile in columns with different pillar geometries and placements. The simulations are performed with a flow rate of 1 μL min^{-1}. All values are in mm s^{-1}.

sidewalls of the channels with a densely packed array of round micropillars (see figure 4.3(a)). Therefore there are also simulations done with structures integrated in the sidewall of the channel. These results are shown in figure 4.3.

Based on these simulation it is clearly visible that the following columns would give the best results with respect to the requirement of constant flow velocity in the transversal direction of the column:

- The column needs to have micropillars which are placed in a hexagonal grid.
- The column needs to have round pillars or square pillars with a corner directed to the flow direction.
- The column needs to have structures integrated in the sidewalls.

In order to reduce the amount of simulations, the following simulation is only performed with a column that has a hexagonal packing of round pillars and structures integrated into the sidewalls. The pillars are packed in a dens manner. This simulation is done to investigate the effect of the chosen flow distributor[180–182]. The result of the simulation with a flow rate of 0.1 μL min^{-1} is shown in figure 4.4. As can be seen here, the distributor distributes the flow with a relatively high flow rate in transversal direction.

Besides this simulation, there are also other simulations done. At first is the pressure distribution inside the channel simulated. The result of this simulation is shown in figure 4.5. In here, it is visible that the largest pressure build-up is near the start of the flow distributor. This is as expected, since a channel with a cross section of 50$\times$ 25 μm^2 is splitted into two channels of 2.5$\times$ 25 μm^2. The next simulation is

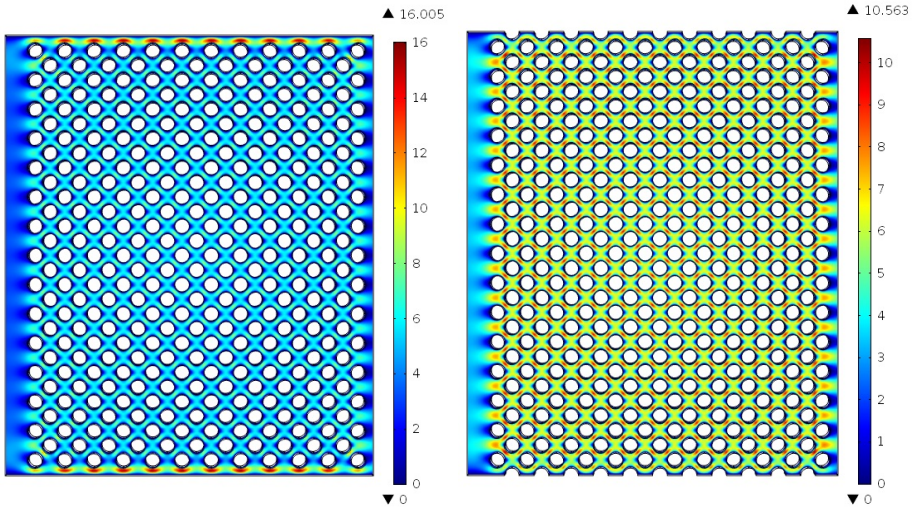

(a) A column without sidewall structures. (b) A column with sidewall structures.

Figure 4.3: Velocity profile in columns without and with sidewall structures. The simulations are performed with a flow rate of 1 μL min^{-1}. All values are in mm s^{-1}.

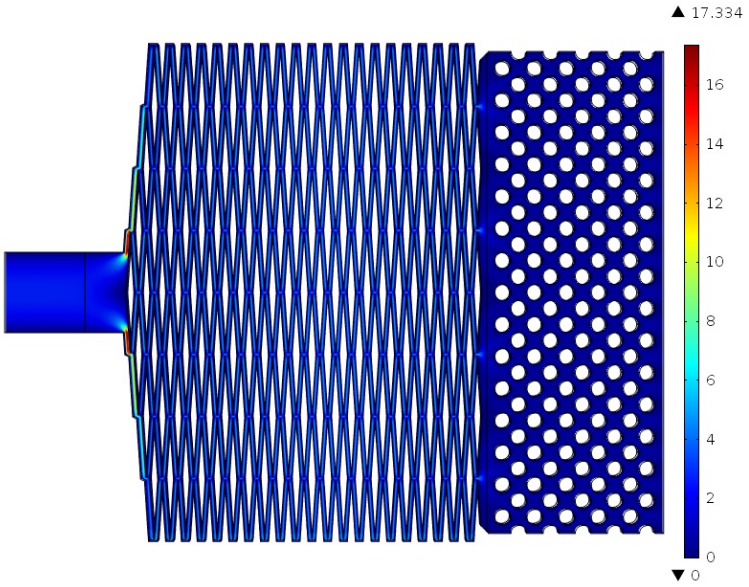

Figure 4.4: COMSOL simulation of the velocity profile in the flow distributor, performed with a flow rate of 0.1 μL min^{-1}. All values are in mm s^{-1}.

of the cell Reynold's number in the middle of the channel (figure 4.6). This is not completely the same as the Reynold's number in equation (2.20). COMSOL uses equation (4.1) and as can be seen here, there is a length scale involved. COMSOL uses the average mesh size for this, so it is the "local Reynold's number". This gives values roughly an order of magnitude lower than calculated analytically in equation (2.20) (also taking into account that a flow rate of 0.1 μL min^{-1} is used for the simulation). However, the simulation shows that there is still a laminar flow because the cell Reynold's number is lower than unity. The final simulated value is the shear stress, which is viscosity times shear rate for Newtonian fluids (see figure 4.7). This simulation is done in order to check whether the DNA will survive the flow distributor. As can be seen in the scale bar, the highest shear stress is 3.22×10^{-23} N pm^{-1}. Literature gives values of 6.3×10^{-23} N pm^{-1} for breakage induced by hydrodynamic shear stress[226], so DNA has a significant chance to survive this. If breakage still occurs, then this is not a big problem, since the next step downstream is PCR amplification and PCR also works with DNA fragments[227].

$$Re_{cell} = \frac{vL}{\nu} \tag{4.1}$$

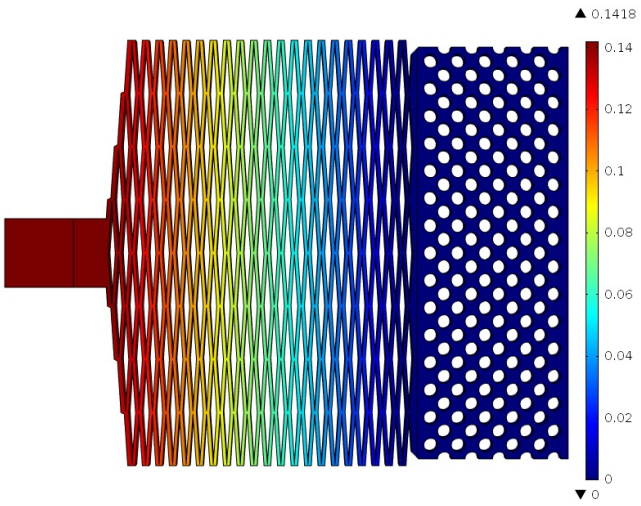

Figure 4.5: COMSOL simulation of the pressure distribution inside the column, performed with a flow rate of 0.1 μL min^{-1}. All values are in bar.

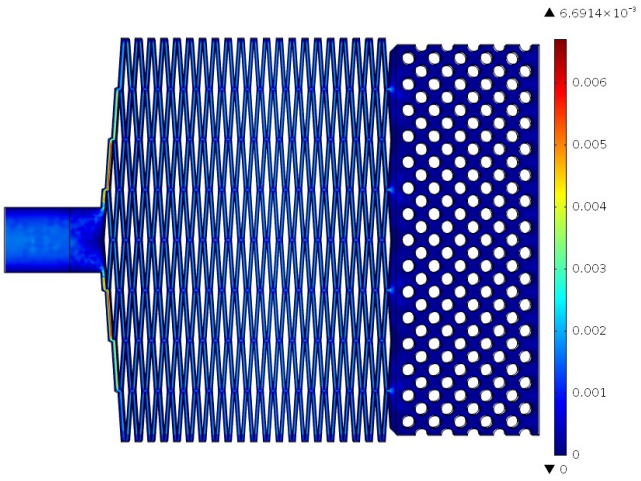

Figure 4.6: COMSOL simulation of the cell Reynold's number, performed with a flow rate of 0.1 μL min^{-1}.

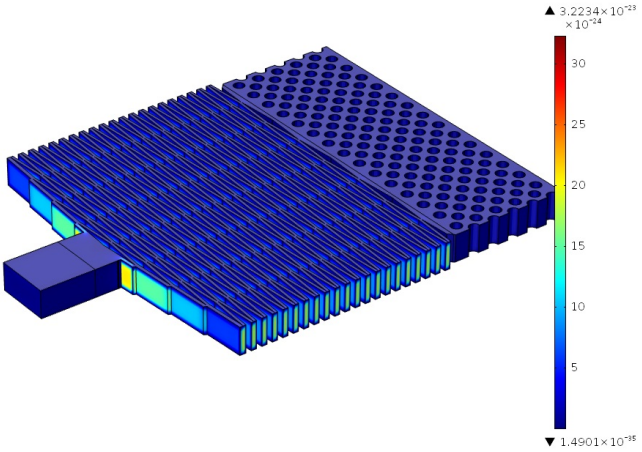

Figure 4.7: COMSOL simulation of the shear stress, performed with a flow rate of 0.1 μL min^{-1}. All values are in N pm^{-1}.

4.2 Fabrication process

The first step of the fabrication process is designing the photolithography mask. This mask is designed with CleWin5 mask designing software (PhoeniX Software, Enschede, The Netherlands). The resulted masks can be found in appendix B and close ups of the drawn in- and outlet can be found in figures 2.2 and 2.5 in chapter 2. After receiving the mask, an inspection by optical microscope is done. During this inspection a small error was found in the design. The backside of the last row of diamond-shaped pillars of the inlet flow distributor on the chip with square pillars was faulty drawn. This backside should not be flat, but pointy like all other diamond-shaped pillars. This mistakenly drawn chip, together with a correctly drawn chip is shown in the microscope image in figure 4.8. All other microscope images are shown in appendix F.

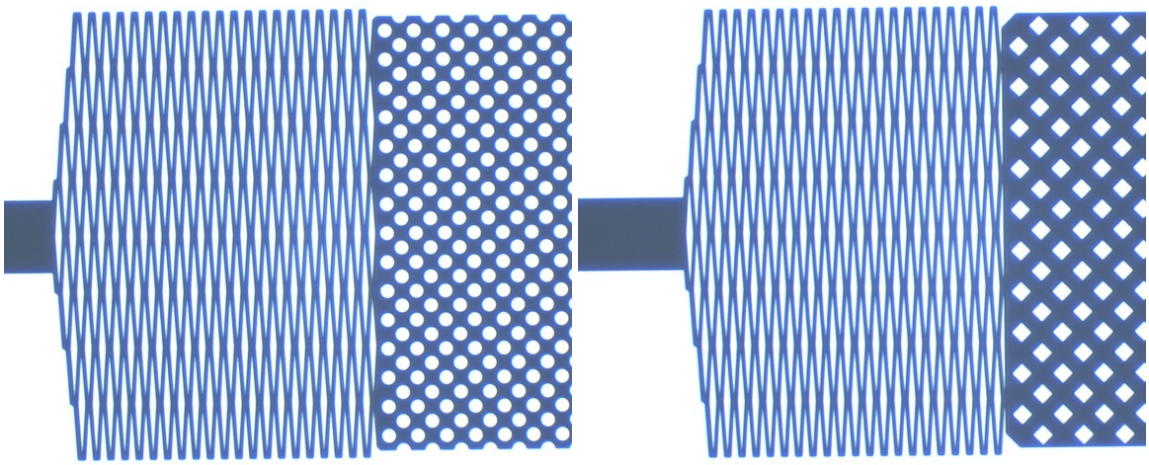

(a) The correctly drawn pillars. (b) The faulty drawn pillars.

Figure 4.8: Microscope images of a correctly and faulty drawn mask.

The first step of the clean room work is the wet oxidation step. This step is analysed with a Woollam M-2000UI ellipsometer (Lincoln, NE, United States). The aimed layer thickness was 1.2 μm and the ellipsometric analysis showed an average thickness of 1.213 μm. A complete scan is shown in appendix G.

The next step in the fabrication process is etching. As can be seen in the process flow in appendix C, this step is performed first with the Alcatel Adixen AMS100 DE (Annecy Cedex, France) etching tool and secondly with the Alcatel Adixen AMS100 SE (Annecy Cedex, France) etching tool. The first machine etched through the SiO_2 layer and the second one etches the structure into the Si. After 3 minutes of etching with the Adixen DE the discolouring caused by the oxide layer was gone, indicating that the etching step was successful. The etch rate of the B-HARS process of the Adixen SE is first determined by etching 4 minutes and then measuring the depth with the Veeco Dektak profiler (Plainview, NY, United States). This device measures with a 2.5 μm stylus a line on the surface of a substrate. The result of this is an etch rate of 4.8 μm min^{-1}, so an etching time of 5:10:88 minutes is applied. This etch time is rounded to the closest completely finished cycle of passivation and etching. These Alcatel etching machines are also used for etching the via-holes for the fluidic inlets and outlets, only now the B-UNIFORM recipe is used. This recipe has an etch rate of 18$\sim$22 μm min^{-1}, so an etching time of 30 minutes was first applied. But this was not enough for etching all via-holes completely through a 525 μm thick wafer. An additional etch time of 5 minutes was applied and this was enough to open all via-holes. After this step, the 1.2 μm oxide layer is removed and the etched structures are analysed. The first analysis is to check the channel depth. For this the Veeco Dektak profiler (Plainview, NY, United States) is used. The result of this step height measurement, which gave a depth of $\sim$22.5 μm is shown in appendix G.

Subsequently, SEM images are made with Jeol JSM 5610 SEM (Tokyo, Japan). As can be seen in these SEM images in 4.9 and especially in the birds-view image in figure 4.9(c), are the pillars and sidewalls perfectly vertical. Another observation is that the design error of the mask is transferred to the pillar structure, as can be seen in figures 4.9(a) and 4.9(d). The structure in figure 4.9(e) shows a known etch effect[180] and will not give any problems during later use.

The next step in the clean room process flow is the anodic bonding step. The standard recipe, which

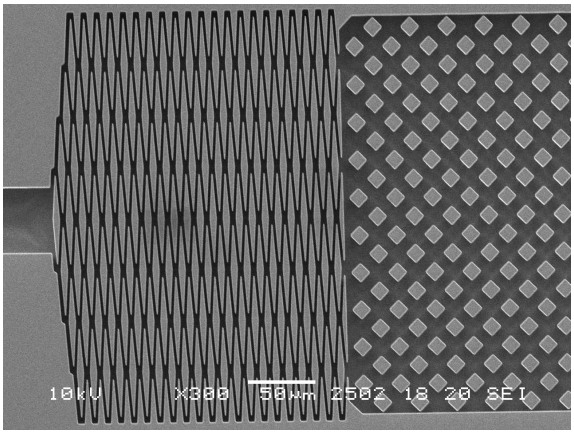

(a) SEM image of the column inlet.

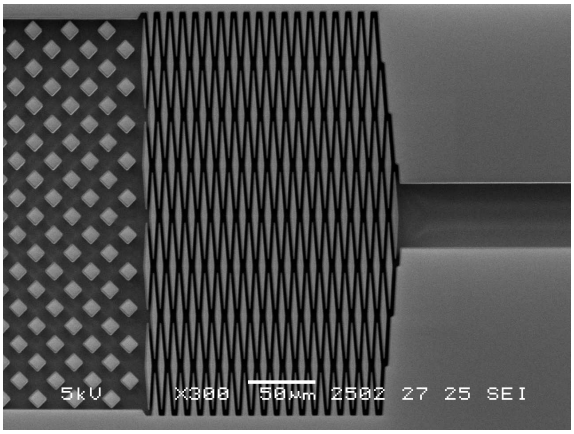

(b) SEM image of the column outlet.

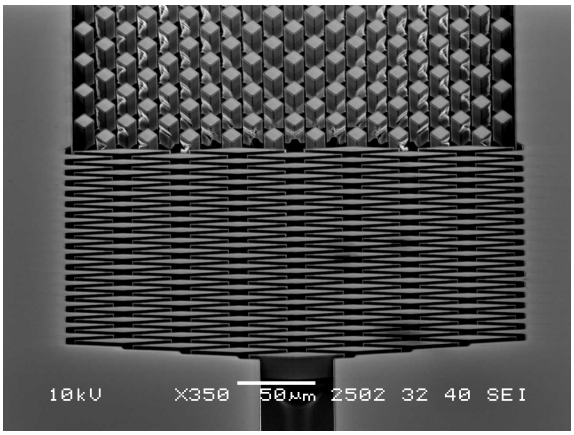

(c) SEM image of the straight square pillars.

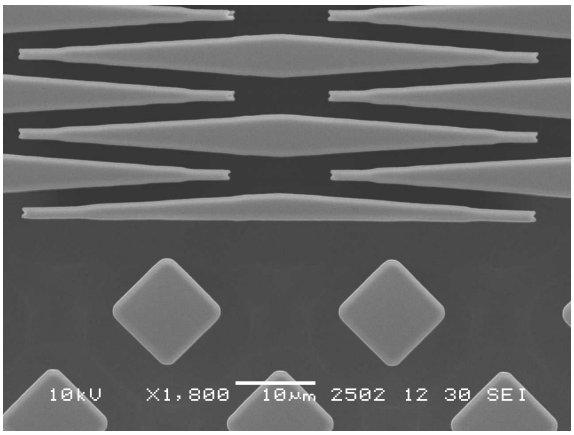

(d) SEM image of the design error.

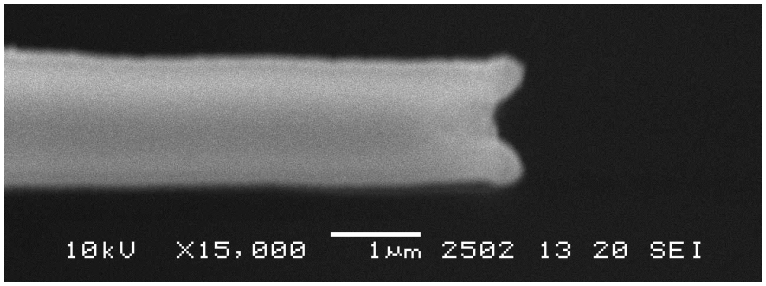

(e) SEM image of an etch effect.

Figure 4.9: SEM analysis of the μSPE column with square pillars.

is schematically depicted in appendix G, is performed with an EVG EV501 anodic bonder (St. Florian am Inn, Austria). Literature described anodic bonding of structures as small as 10$\times$10 μm[228], but the performances are often device dependent. In order to check if the pillars were also anodically bonded, cross-sectional analysis is done. Dicing of these cross-section is done with the Disco DAD-321 automatic dicing machine with TC-300 blade (Tokyo, Japan). The chip was covered with 80 μm thick STW T10 dicing foil of Nitto Denko Corporation (Osaka, Japan) in order to protect the single mounted chip against movement during dicing. The dicing depth is set at 400 μm deep into the chip, and dicing is done on both sides of the chip. After removing the dicing foil, the chip is manually broken with a pair of tweezers. This is done in order to protect the pillars against the brute force of the dicing machine. This cross-section is mounted into the FEI Sirion HR-SEM (Hillsboro, OR, United States) and SEM images of the bonded area and of the scallops of the cyclic BOSCH process at the sides of the pillars at different heights. The SEM images of the bonded area with the scallops on the top side of the pillars (h = 0 μm) are shown in figure 4.10. The SEM images of the scallops at other heights are given in appendix H. The SEM images in figure 4.10 and in appendix H reveal developed scallops on the top side of the pillars. However, deeper etching into the substrate causes that the gas composition in between the pillars to change from the optimal gas composition into a non-optimal gas composition. This is due to diffusion of the etched material. This material is removed from the surface and "contaminates" the etchant gasses in between the pillars, creating a non-optimal etch gas, hereby slightly altering the scallop pattern.

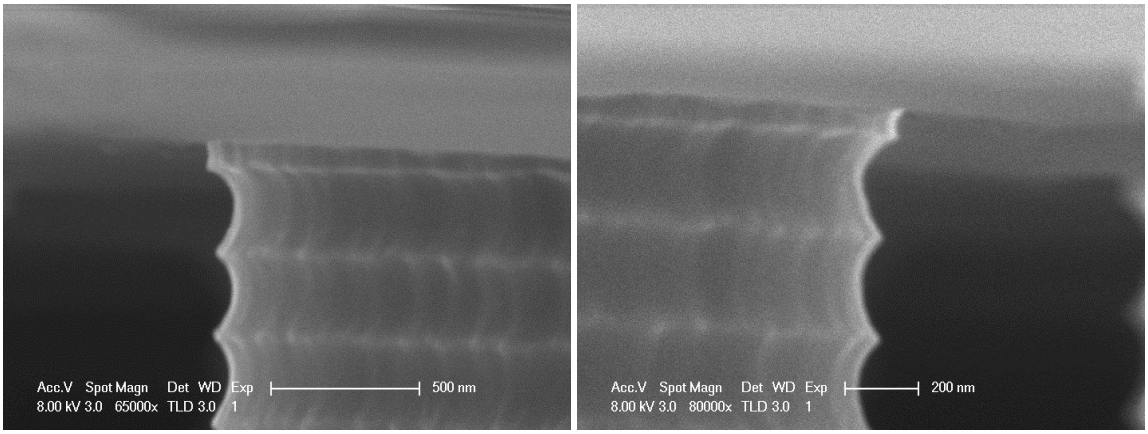

(a) SEM image of the top left side of a bonded pillar. (b) SEM image of the top right side of a bonded pillar.

Figure 4.10: SEM analysis of bonded round pillars.

4.3 Flow profile analysis

In microfluidics it is important to study the behaviour (especially the velocity profile) of the fluid inside the chip. The final operation procedure of the chip uses aqueous buffer solutions and an oil, therefore both are studied. The liquids are pumped into individual chips and the resulting flow profile is studied with the Leica DMI5000M inverted microscope with LAS 3.8.0 software (Wetzlar, Germany).

4.3.1 Aqueous solutions

The flow profile of aqueous liquid inside the chip is analysed with a 10^{-4} M fluorescein solution (Sigma-Aldrich/Fluka Analytical) instead of the buffer solutions because it is easier to visualize the velocity profile with fluorescence. This solution is pumped into the chip at different flow rates (0.1, 0.5, 1.0, and 2.0 μL min^{-1}) and subsequently the chip is flushed with DI water at a flow rate of 10 μL min^{-1}. This handling creates a water/fluorescein interface inside the channel, which shows the velocity profile of the liquid inside the chip. The behaviour of the liquid is studied by using the Leica microscope. The exposure is set at 1 s, the gain at 1x, the saturation at 1.5, the gamma at 0.61, and the histogram ranged from 0 to 255. Results of these analysis are shown in the figure 4.11. During these analysis, the working principle of the flow distributor was observed. The velocity profile, which was formed at the water/fluorescein interface was not as flat as previously reported in the literature[180,181]. A reason for this can be the relatively short channel before the column. The T-junction there disturbs the flow profile by creating a two-phase system, even when one of the flows is turned off. This can be observed in figure 4.12. This microscope image also clearly shows that there is no fluorescence in the upper left part of the distributor. But still there is a homogeneous fluorescent signal at the end of the distributor. Here it is clearly visible that the interconnected channels can distribute to all sides of the column when one of the channels is not working properly (transversal distribution of the flow), as is described before[180,181].

4.3.2 Oil

The behaviour of oil is investigated by pumping M5904 mineral oil (Sigma-Aldrich, BioReagent for molecular biology) into the chip. A flow rate of 0.5 μL min^{-1} is used because of the viscosity of the oil, which is higher than the viscosity of water (30 cp compared to a viscosity of 1 cp of water). After pumping the oil into the chip, it became visible that the viscosity is too high. The oil is not capable of entering the distributor part of the column, even after increasing the flow rate to 5 μL min^{-1}. The oil flow stopped before the distributor and formed two typical oil menisci, which can be seen in figure 4.13. These menisci are formed in this manner because of the hydrophobic interaction of the oil with the channel wall. The pressure inside the system increased, leading to leakage at the point where the capillary is connected to the chip. A solution can maybe be formed by heating up the chip. Viscosities tend to decrease when the liquid is heated up. However, this is not tested experimentally because this idea came at the end of this thesis research.

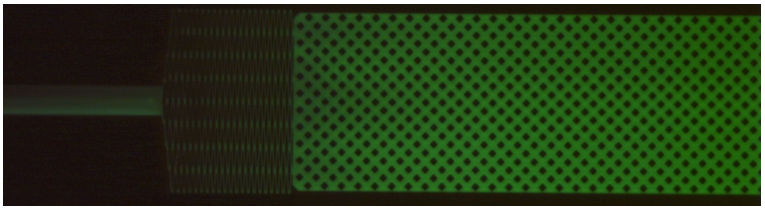

(a) At t = 0 s.

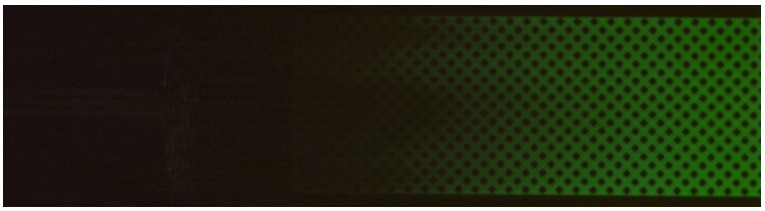

(b) At t = 1 s.

(c) At t = 2 s.

(d) At t = 3 s.

Figure 4.11: Fluid profile analysis of a liquid. The fluorescein is flushed away with DI water at a flow rate of 10 μL min^{-1}.

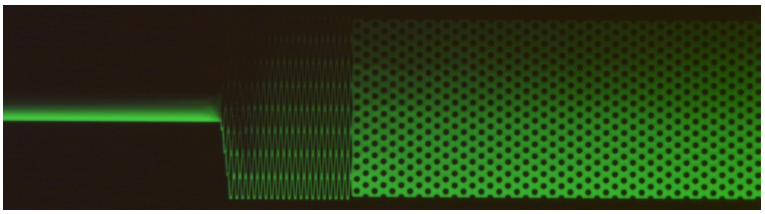

Figure 4.12: The strong transversal distribution in the flow distributor.

4.4 Functionalization

Functionalization of silicon with either chitosan or APTES is tested on 1.5$\times$1.5 cm $<$100$>$ Si samples, which are created by dicing a wafer. This is done in order to verify whether the functionalization process is effective or not. These samples are analysed with two distinct and well-established surface analysis methods. The first used method is X-ray photoelectron spectroscopy (XPS). This technique uses X-rays in order to extract Auger electrons from the atoms on the surface. These Auger electrons have distinct energy values for different elements. With this technique it is possible to measure the relative composition of the surface. The XPS spectra for both the chitosan functionalization as well as the APTES functionalization are given in appendix I. A summary of the results for the chitosan functionalization can be found in table 4.1.

These results show that a significant amount of carbon is present on the piranha cleaned SiO_2 surface. This contamination is extracted from the air and adsorbed on the surface. The amount of carbon is rather high because of the time between the cleaning and analysis. The samples were cleaned at the

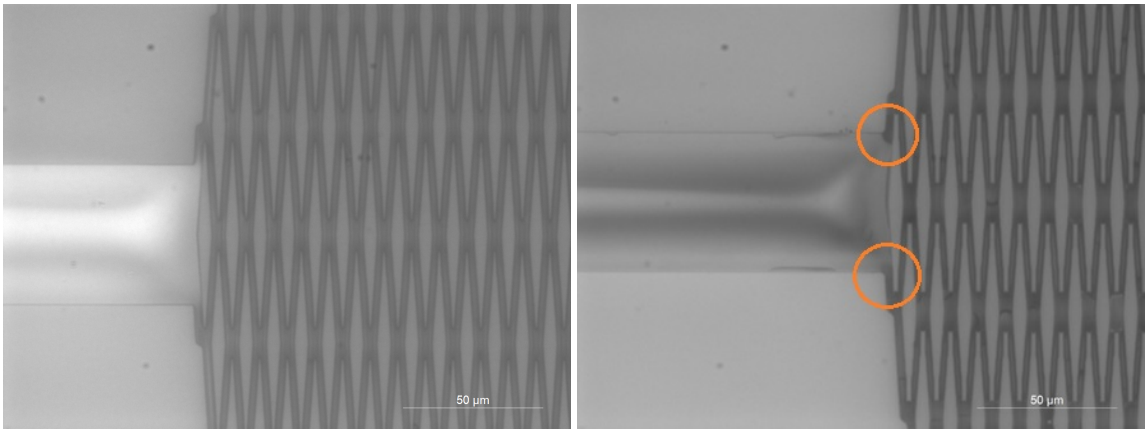

(a) Microscope image of an empty channel. (b) Microscope image of an oil filled channel.

Figure 4.13: Microscope images of velocity profile test with oil.

Table 4.1: XPS results chitosan functionalization.

	C [%]	**N** [%]	**O** [%]	**Si** [%]
Piranha cleaned SiO_2	12.38	-	46.96	40.66 (54% bare Si, 46% SiO_2
GPTMS	14.16	0.86	46.97	38.01 (54% bare Si, 46% SiO_2
Chitosan	26.22	2.11	42.88	28.79 (54% bare Si, 46% SiO_2

same time as the samples for the GPTMS and chitosan functionalization. The time between cleaning and analysis is therefore 27 h. The increase of carbon after the GPTMS functionalization is due to the carbon atoms present in the carbon backbone of GPTMS (a total of six carbon atoms is present in the chain, as can be seen in figure 4.14). This additional carbon decreases the amount of silicon in the results because the analysis depth of the XPS is limited[229]. This is also the reason why the percentage of silicon further decreased after the chitosan functionalization. Chitosan is a mucopolysaccharide (see figure 1.15) and therefore contains relatively a large amount of carbon. This is evidenced by the percentage of carbon measured. Also 2.11 % of nitrogen is measured, indicating the nitrogen of the amino groups. The 0.86% of nitrogen in the GPTMS layer is unexplainable. A guess is that it also is adsorbed from the air.

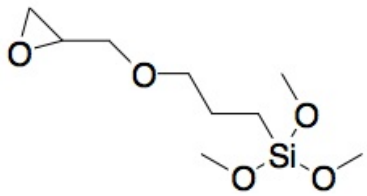

Figure 4.14: Structural formula of GPTMS.

The APTES functionalization is also analysed with XPS. A summary of these results can be found in table 4.2. From these results it is visible that the piranha cleaning is indeed effective. This effect decreases over time once the samples are taken out of the piranha because the surface starts to adsorbs organic compounds from the air. This is clearly visible when the XPS data of the piranha cleaning of the chitosan functionalizatin is compared with the data of the XPS measurement of the APTES functionalization. The time between cleaning and measurering was $\sim$27 h and $\sim$30 min, respectively. The C/N ratio for the APTES functionalization in ethanol is 9. This is not 3, as would be expected by looking at the APTES molecule (figure 1.14). This higher ratio can be addressed to incomplete crosslinking at the ethoxy groups and carbon contamination adsorbed on the surface. A very remarkable result is the presence of zinc. This element should not be present and is an unusual contamination. A reason for this contamination can be an unclean fumehood, glassware, or tweezers. The APTES functionalization in dry toluene gave a C/N ratio of 4 and it did not have the zinc contamination. However, visual inspection showed spots (see figure 4.15), which can be islands of (polymerized) multilayers. This is supported by the fact that the percentages of silicon and oxide are less and the carbon and nitrogen percentage

Table 4.2: XPS results APTES functionalization.

	C [%]	**N** [%]	**O** [%]	**Si** [%]	**Zn** [%]
Piranha cleaned SiO_2	3.81	-	46.06	50.13 (54% bare Si, 46% SiO_2	-
APTES in EtOH	25.77	2.91	34.57	36.23 (54% bare Si, 46% SiO_2	0.52
APTES in dry toluene	45.25	11.90	27.16	15.68 (54% bare Si, 46% SiO_2	-

are higher than for the functionalization in ethanol. The in ethanol functionalized samples did not show those islands.

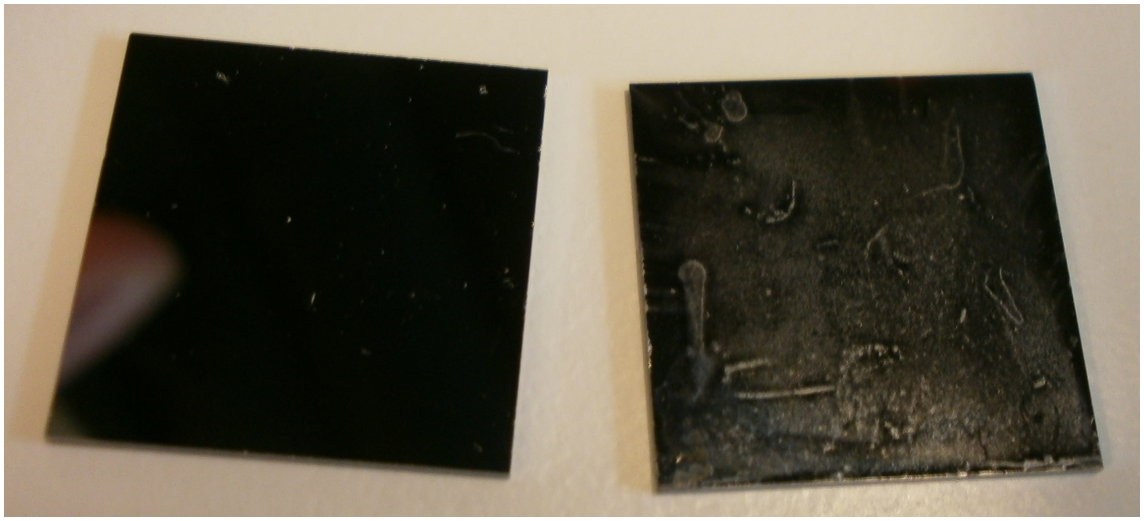

Figure 4.15: Photograph of substrates after APTES functionalization in EtOH (left) and dry toluene (right).

The second used surface analysis technique is contact angle measurements. These measurements are done with a DataPhysics OCA 15plus contact angle system (Filderstadt, Germany) in sessile drop operation. This device puts a drop of 25 μL water on the surface of the substrate and measures the contact angle of the drop with the surface. This is the so-called static contact angle. After this measurement, the drop is subsequently increased and decreased with 25 μL (rate: 3 μL s^{-1}), while continuously measuring the advancing and reducing contact angle (ARCA). This is done five times in one measurement, with after every increase or decrease of 25 μL a stabilisation period of 3 s. These measurements give an indication of the hydrophobicity/hydrophilicity of the surface. The results of these measurements are shown in table J.1 and appendix J. As can be seen in table J.1, there is a clear distinction between the different surfaces. The chitosan functionalization shows a clear trend of increasing contact angle. This is as expected by looking at the amount of carbon atoms in the monolayer. Although, the values are not corresponding to the values found in literature. The functionalized samples analyzed in this research all have contact angles that are lower than the ones found in literature. This can be explained by non-optimal covering of the sample due to non-optimal reaction conditions. This is in agreement with the XPS data, in which a C/N ratio of $\sim$12.5 for the chitosan functionalization can be observed, while a ratio of $\sim$6.5 (depending on the degree of deacetylation) is most optimal. The sample functionalization with APTES in ethanol shows a higher contact angle than the angles found in the literature. This can be explained by the incomplete crosslinking of the ethoxy groups, leaving more carbon on the surface. The carbon chains are hydrophobic, which thus increases the contact angle. This is also in agreement with the C/N ratio of 9, which is found during the XPS analysis. The functionalization of APTES performed in dry toluene showed contact angles which were in agreement with the literature. This is also strengthened by the XPS data. In these data, a C/N ratio of 4 is found, indicating almost complete crosslinking.

The functionalization inside the chip, however, gave problems. With the Bernoulli pump it was possible to get water into the chip, but the water only moved via the sidewalls of the channel. After 20 minutes of applying the vacuum, an inspection with the Leica microscope was made. These are shown in figure 4.16. The inlet of the column is shown in figure 4.16(c) and the distance started counting after the flow distributor. As can be seen here, the water advanced roughly 6.5 mm into the chip.

After 35 minutes, the water reached the second distributor on the other side of the column. At this

Table 4.3: Results of contact angle measurements. All angles are in degrees.

Substrate	**Static contact angle (θ_{stat})**	**Advancing and reducing contact angle (θ_{adv} / θ_{red})**	**Theoretical θ_{stat}**
Native SiO_2	38.6 $\pm$ 1.6 (n=2)	42.0 $\pm$ 2.8 (n=5) 17.1 $\pm$ 0.1 (n=4)	45 [230] 52 [231]
Piranha cleaned native SiO_2, with carbon contamination	30.5 $\pm$ 4.9 (n=14)	34.1 $\pm$ 2.9 (n=20) 14.5 $\pm$ 1.8 (n=20)	$<$20 [232] 34 [233]
GPTMS functionalization	38.7 $\pm$ 3.7 (n=10)	41.2 $\pm$ 2.6 (n=20) 16.0 $\pm$ 1.0 (n=20)	60 [234] 61 [235]
Chitosan functionalization	53.4 $\pm$ 18.3 (n=8)	53.0 $\pm$ 1.7 (n=20) 16.1 $\pm$ 0.5 (n=20)	87.5 $\pm$ 2.5 [236] 76.4 $\pm$ 5.1 [149]
Piranha cleaned native SiO_2	10.2 $\pm$ 6.3 (n=10)	19.1 $\pm$ 0.8 (n=14) 4.7 $\pm$ 0.5 (n=14)	$<$20 [232] 34 [233]
APTES functionalization in EtOH	71.6 $\pm$ 6.3 (n=8)	76.2 $\pm$ 2.2 (n=20) 39.2 $\pm$ 0.6 (n=20)	57 [128] 67 $\pm$ 1 (θ_{adv}) [237] 32 $\pm$ 1 (θ_{red}) [237]
APTES functionalization in dry toluene	61.0 $\pm$ 4.9 (n=8)	65.4 $\pm$ 2.8 (n=20) 27.8 $\pm$ 0.4 (n=20)	57 [128] 67 $\pm$ 1 (θ_{adv}) [237] 32 $\pm$ 1 (θ_{red}) [237]

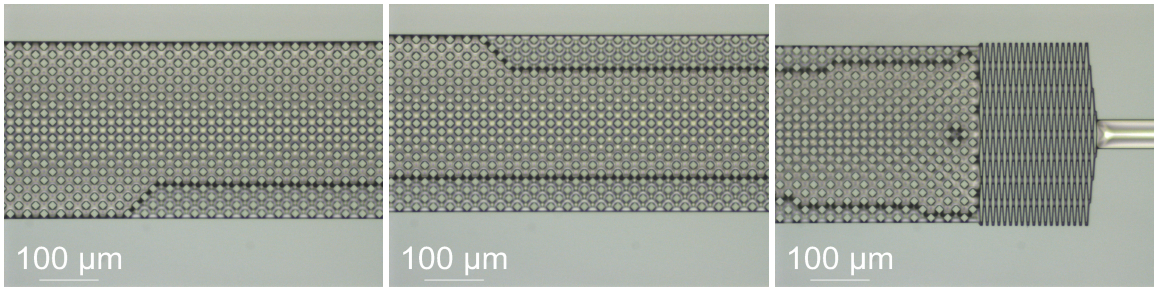

(a) ∼ 6.5 mm into the channel. (b) ∼ 5.7 mm into the channel. (c) 0 mm into the channel.

Figure 4.16: Microscope images taken after 20 minutes of applying a vacuum.

point, the pressure drop became too high and the Bernoulli pump came off from the water faucet (see figure 4.17. As can be seen in the microscope images in figure 4.18, the water continued to advance via the sidewalls of the channel until it reached the second distributor.

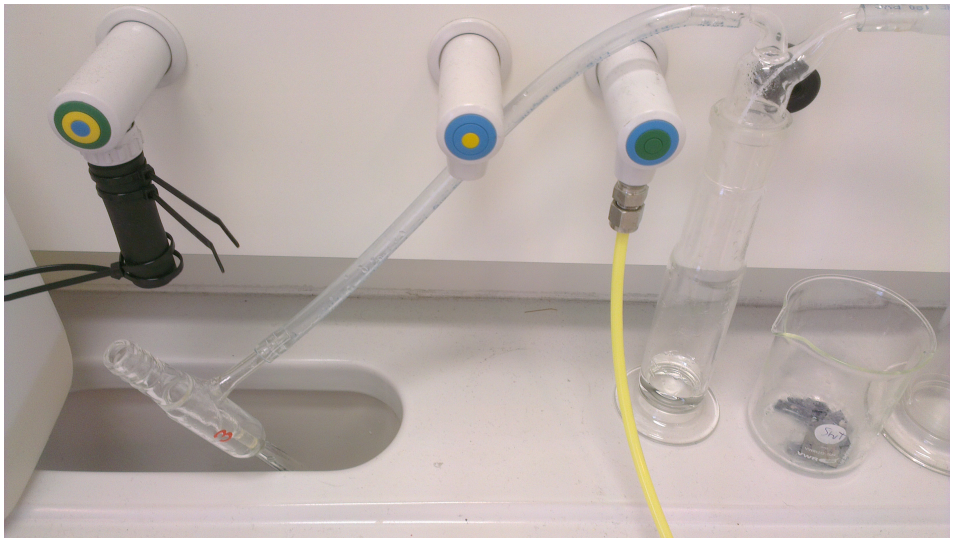

Figure 4.17: Bernoulli pump faillure due to a too high pressure drop.

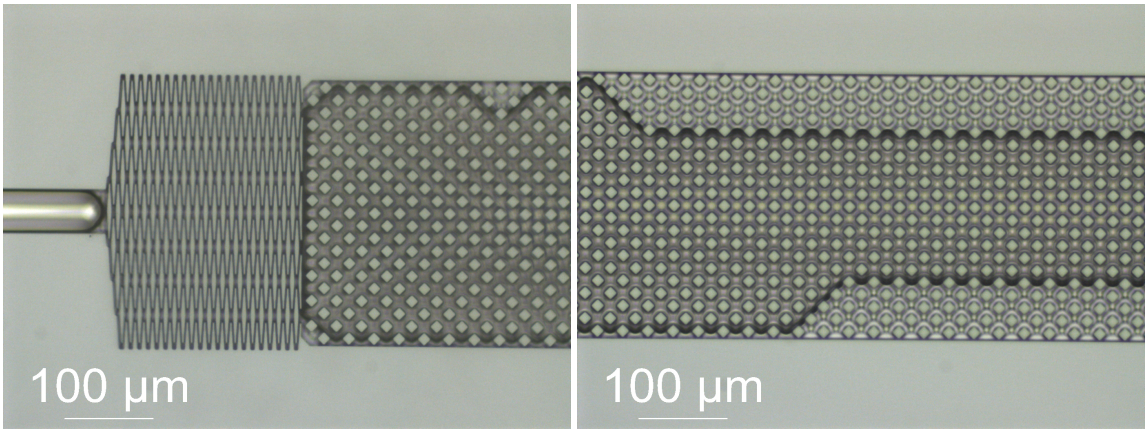

(a) 10 mm into the channel. (b) ∼ 6.0 mm into the channel.

Figure 4.18: Microscope images taken after 35 minutes of applying a vacuum.

Because the vacuum technique was already problematic for water, it was expected to be the same for a standard piranha solution, since the viscosity of H_2SO_4 is higher than that of water (26.7 cP compared to 1 cP of water). This is a lowered by adding the H_2O_2 (viscosity of $\sim$1.2 cp), but the viscosity stays higher than that of water, no matter which ratio is used. However, with this came the idea to investigate the effect of different piranha compositions on the hydrophilicity of the surface. This effect is studied with contact angle measurements. The same method as with the previous described contact angle measurements is used and the results of this are shown in the graph in figure 4.19. All values with standard deviations, and values for a non-cleaned substrate and a plasma cleaned substrate are given in table J.1 in appendix J. As can be seen here, there is a clear trend in hydrophilicity of the surface related to the different ratios of the piranha mixture, with a minimum in the hydrophilicity after cleaning with a 1:1 ratio of H_2SO_4:H_2O_2. This can be attributed to the following reactions in which H_2SO_4 and H_2O_2 react to Caro's acid, hydronium ions, bisulfate ions, and atomic oxygen:

$$H_2SO_4 + H_2O_2 \longrightarrow H_2SO_5 + H_2O$$

$$H_2SO_4 + H_2O_2 \longrightarrow H_3O^+ + HSO_4^- + O$$

This mixture is an aggressive cleaning agent due to Caro's acid. This is one of the strongest oxidizing agents. The mixture is able to dissolve even elemental carbon (for example photoresist residues). In a 1:1 ratio there is an optimal ratio, as can be seen in the chemical equation. However, this solution can only be used in small volumes ($<$ 50 mL) because several university handling procedures mention that a 50% solution of H_2O_2 in H_2SO_4 can be explosive (due to Caro's acid)[238,239]. A suggestion would be to investigate different solutions in small volumes in H_2SO_4:H_2O_2 ratios from 7:1 to 1:2 and also compare this with, for example, base piranha (ammonium hydroxide (NH_4OH) with H_2O_2).

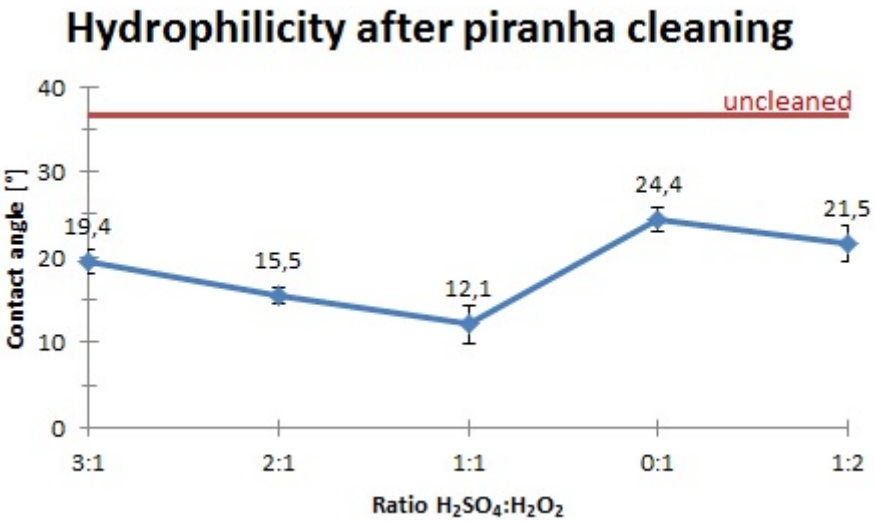

Figure 4.19: Hydrophilicity of the surface after cleaning with different ratios of piranha.

It is not tested to get the different piranha solutions in the chip. As can be seen in figures 4.16, 4.17, and 4.18 it was not possible to get water (which has, as mentioned before, a much lower viscosity than piranha solutions) into the chip with the use of a Bernoulli pump. Therefore, a different method is tried, one that uses an overpressure instead of a vacuum. In this method, a 25 mL Hamilton Gastight syringe (Bonaduz, Switzerland) and Teflon tubing with an inner diameter of 250 μm is used. A home-made plug is pressed manually on one of the inlet holes, and the other one is covered with a Teflon reaction tube stopper. However, it was not possible to manually make a leakage free connection on the two inlet holes. Therefore clamps are used, as can be seen in figure 4.20. But this did not improve the connection between the plugs and the inlet holes. The leakage that occurred (see figure 4.21) is very dangerous when piranha solutions are used, therefore it was decided to stop the trying to get piranha into the chip and put the focus on functionalization of the channels without piranha cleaning. Piranha also activates the surface by creating hydroxyl groups, but these are already present at the walls of the micropillars and the channel walls, although in a lesser amount than after piranha cleaning.

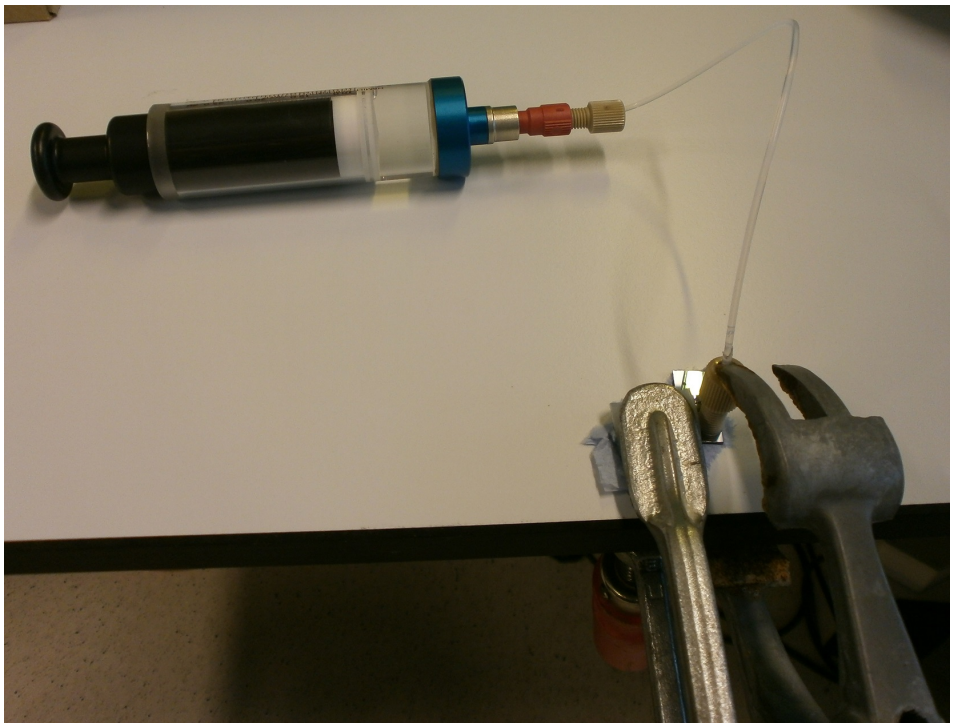

Figure 4.20: The home-made setup to get piranha into the chip.

Figure 4.21: The occurred leakage next to the inlet plug.

4.5 Extraction

The extraction performances of APTES and chitosan are first tested with flat samples. These samples are made of a <100> DSP Si wafer with native oxide. This wafer is diced in the x-direction with a pitch of 4 mm wide and in the y-direction with a pitch of 5 cm (wafer is diced into half), creating rectangular shaped strips of various lengths, but all with the same corners and edges on one side of the rectangular strip. These samples are functionalized according to the previously described protocols. The DNA extraction is done by putting 1 strip into a PCR tube of the Qubit dsDNA HS assay kit with a pH 5.0 MES buffer (for protonation of the amino group). After that, the strip is transferred to a PCR tube containing the MES buffer and DNA. After 15 minutes, the strip is taken out of the DNA solution and put into the pH 9.2 TRIS buffer for the elution of the DNA from the sample. Care is taken that an equal amount of liquid (400 μL) is present in all the PCR tubes. The test strips are therefore for 1.1 mm in the liquid. This makes the effective extraction surface 8.8 mm^2 (the functionalization is on both sides of the test strip). Every run is done with 3 test strips (in triplo). Samples are taken from every PCR tube and analysed with the Qubit dsDNA HS assay kit. The results in graphical format are given in appendix K. As can be seen, the APTES did not elute DNA with a TRIS buffer of pH 9.2. This is in accordance with the broad range of pK_a values found in the literature[116–119]. Therefore a TRIS buffer with a pH of 12.6 was made. The same extraction test procedure is performed with this buffer. The results of these extraction tests are summarized in table 4.4. A complete overview of the results can be found in appendix K.

Some differences can be found, when the results of the different functionalizations are compared. First of all it is clear that the chitosan functionalization does not have a high extraction efficiency when compared to both the APTES functionalizations. The chitosan layer was only capable of extracting 10.47% of the DNA from the solution. The APTES layer that was grown in ethanol was capable of extraction 77.02% and the APTES layer grown in toluene even 94.99%. These differences in quality is also evident in all the results of the functionalization analyses, *i.e.* the APTES layer grown in dry toluene had the best contact angle and the highest C/N ratio in the XPS data. Chitosan alway had the lowest performances in these analyses. The subsequent elution step on the other hand showed the opposite results. The elution efficiency of the APTES layer grown in ethanol (elution done with TRIS pH 9.2) is only a mere 0.12%. This was already increased by increasing the pH of the buffer to 12.6, but still only 4.23% of the DNA on the test strip was eluted. Chitosan and the TRIS buffer of pH 9.2 on the other hand, were capable of eluting 18.81% of the DNA from the test strip. These difference between the chitosan functionalization and the APTES functionalizatin in dry toluene balancing out, so both were capable of transferring almost the same amount of DNA from the MES buffer to the TRIS buffer.

The chosen DNA analysis method, the Qubit dsDNA HS assay kit, is also tested with several standard solutions of DNA (from different suppliers) and with fish DNA in order to test the accuracy and selectivity of the system. The results of these measurements are shown in table 4.5. As can be seen here, it is still difficult to measure low concentrations of DNA. The measured values are in the case of GenomiPhi $\sim$40% below the value of the supplier. However, it can be possible that the GenomiPhi control vial was not good anymore. It was not ordered new, but taken out of the freezer in the lab. On the other hand, th Qubit dsDNA HS assay kit shows a high specificity for human DNA. The calibration curve of fish DNA all had values which were $\sim$18% of the total amount that was in the sample.

The extraction is also tested on chip. This chip was functionalized without cleaning and activating the surface with piranha prior to the functionalization, since piranha could not be flushed into the chips.

Table 4.4: Summarized results of the extraction tests. All measurements are done in triplo (n=3).

Substrate	**DNA in solution** [ng μL^{-1}]	**DNA on strip** [ng]	**Extraction efficiency** [%]	**DNA in TRIS buffer** [ng μL^{-1}]	**Elution efficiency** [%]
Chitosan	0.50 $\pm$ 0.01	0.05 $\pm$ 0.00	10.47 $\pm$ 1.05	0.01 $\pm$ 0.00	18.81 $\pm$ 1.26
APTES, pH 9.2	1.55 $\pm$ 0.02	1.20 $\pm$ 0.12	77.02 $\pm$ 6.71	0.00 $\pm$ 0.00	0.12 $\pm$ 0.21
APTES, pH 12.6	0.41 $\pm$ 0.08	0.39 $\pm$ 0.08	94.99 $\pm$ 0.64	0.02 $\pm$ 0.00	4.23 $\pm$ 1.34

Table 4.5: Validation of the Qubit dsDNA HS assay kit.

Supplier	**Type of DNA**	**Concentration according supplier** [**ng μL^{-1}**]	**Measured concentration** [**ng μL^{-1}**]
Applied Biosystems	Humand DNA Male	10	8.47 $\pm$ 0.29 (n=9)
Applied Biosystems	Humand DNA Male	10	11.38 $\pm$ 0.66 (n=9)
GenomiPhi	Control DNA	10	5.96 $\pm$ 0.51 (n=9)
Invitrogen Qubit dsDNA HS assay Standard #2	Control DNA	10	9.80 $\pm$ 0.16 (n=9)
B.B. Bruijns	Fish DNA	1	0.08 $\pm$ 0.01 (n=3)
B.B. Bruijns	Fish DNA	2	0.12 $\pm$ 0.03 (n=3)
B.B. Bruijns	Fish DNA	3	0.17 $\pm$ 0.01 (n=3)
B.B. Bruijns	Fish DNA	4	0.24 $\pm$ 0.01 (n=3)
B.B. Bruijns	Fish DNA	5	0.29 $\pm$ 0.01 (n=3)
B.B. Bruijns	Fish DNA	10	0.34 $\pm$ 0.01 (n=3)
B.B. Bruijns	Fish DNA	100	5.36 $\pm$ 0.09 (n=3)

However, it is assumed that there are some active hydroxyl groups on the channel walls and pillars. The functionalization is performed by flushing a 4% v/v APTES solution in ethanol into the channel. Once the channel was filled, the flow was stopped. Fresh APTES solution was flushed with a flow rate of 1 μL min^{-1} into the channel after it reacted for 2.5 h. This fresh solution also stayed inside the channel for 2.5 h. Afterwards, the channel was flushed with ethanol and the MES buffer that is used to protonate the amino groups. Then, a DNA solution was flown through the chip. However, this was not successful because the channels became clogged. In an attempt to solve it, all solutions were filtered with a Nuclepore polyethylene filter with 2.0 μm pore size (Pleasanton, CA, United States). This filter membrane was placed directly on top of the chip and the connections are made with the membrane in between the chip and the outlet of the capillary. However, this method was not successful, as can be seen in figure 4.22. This can be an accumulation of dirt with dimensions smaller than 2.0 μm, which eventually blocked a channel of 2.5 μm width. A possible way of solving this is by filtrating the solution with a 0.45 μm syringe filter disk prior to injecting it into the channel. However, this is not a desired method because the filtrating can also capture some of the DNA, and this is not wished with forensic samples, which are low in DNA concentration.

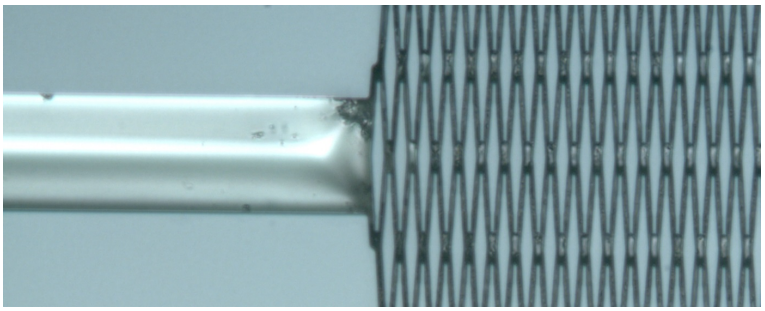

Figure 4.22: Accumulated contamination before the distributor.

Chapter 5

Conclusions

The performed Master's thesis research was focussed on the development of a plug-based μSPE system for the extraction and purification of DNA. The research was divided into separate steps and the conclusions of them will therefore be discussed in separate paragraphs.

5.1 Fabrication

The designed mask is based on a series of COMSOL simulations. The velocity profile through a column with different pillar geometries and placements were simulated. From these simulation it became evident that a hexagonal packing with integrated structures on the sidewalls will give the most homogeneous distributed velocity profile. The subsequent fabrication process was without any unexpected challenges. All the used clean room steps are well-established methods and therefore they give very reproducible results. A total of 10 wafer were processed and none of them showed any errors due to the fabrication process. The only error found is the one in the mask that is drawn.

5.2 Characterization of the chip

The designed chip showed an almost flat profile when a fluorescein filled column was flushed with DI-water. This indicates that the flow distributor is working. However, the formed profile was not as flat as is proven in the literature[180,181]. This can be attributed to the two-phase system created at the T-junction in the channel before the column. It was not possible to analyse the flow profile of the oil in the channels because the oil has a too high viscosity. The oil entered the chip, but only until the first flow distributor. Here it stagnated due to a too high pressure drop, as the pressure drop scales with the viscosity of the fluid (see equation (2.17). This created two menisci.

5.3 Functionalization

The different functionalization steps are first performed on flat test samples. These substrates are subsequently analysed with XPS and contact angle measurements. The results of these measurements clearly show that the functionalization steps occurred, but that the reaction parameters were not yet optimal. A parameter that can have a significant influence is the temperature[133,134]. A study into the effect of temperature during the functionalization can help to get better defined monolayers. The chitosan functionalization and the APTES functionalization in ethanol both showed a higher C/N ratio and lower contact angles than expected. For the chitosan functionalization, this can be attributed to the large amount of reactions that can occur with a GPTMS/chitosan system (see chapter 1 for an overview). The reason for the difference in measured values and literature values in the APTES functionalization in ethanol can be linked to incomplete cross-linking of ethoxy groups due to non-optimal reaction parameters. The functionalization inside the chips were not successful. The piranha solution has a too high viscosity, even at different H_2SO_4:H_2O_2 ratios. The effectiveness of these different piranha ratios was also investigated with contact angle measurements. From these data it became evident that the 1:1 ratio gives the most hydrophilic surface. However, literature reports that a 50% concentration of H_2O_2 in H_2SO_4 explosive is, so care must be taken when these concentrations are used.

5.4 DNA quantitation method

The Qubit dsDNA HS assay kit and the Fluorometer 2.0 are used for the quantitation of the DNA in solution. Although the method is not completely accurate, showing values for control samples that are show

2 and 40% difference with the standard concentration of 10 ng μL^{-1}, the method is still used throughout this research, since the method has proven to be more useful than conventional fluorescence measurements. The supplier guarantees linearity between 0 and 100 ng μL^{-1} if every sample is measured with the same standards. The straightforwardness of the analysis method simplifies the method significantly and increases the throughput of samples.

5.5 Extraction

The extraction of DNA was only performed on flat test samples since the functionalization of the chip was not achieved. The results of the extraction and elution tests with the different functionalizations does not give a conclusion which functionalization is the best. For the extraction of DNA from the MES buffer, a APTES monolayer which is grown in dry toluene extracts the most of the DNA, namely almost 95%. However, the elution of this same sample was only $\sim$4.2%. For this elution step a TRIS buffer of pH 12.6 was used. The elution efficiency with this buffer was already better than the elution from APTES with a TRIS buffer of 9.2, only a mere 0.1% was eluted. Chitosan on the other hand, had a low extraction efficiency. This was only $\sim$10.5%. However, the elution efficiency was rather high when compared to the elution efficiencies of the APTES layers, namely $\sim$18.8%. These differences in extraction efficiencies can be explained by the functionalization steps, which were, according to the XPS and contact angle measurements results, done at non-optimal reaction conditions. The time did not allow it to further investigate the different parameters of the functionalization steps. The low elution efficiency of the APTES can possibly be explained with the pK_a value of APTES. The literature describe a whole range of different values[116–119], making it difficult to find a proper buffer solution. The only conclusion that can be made here is that the reproducibility between test samples with the same functionalization is high, which is proven by the low experimental error (standard deviation).

5.6 Overall conclusion

The chosen method of ion exchange μSPE is a potential interesting method for DNA extraction. However, the chosen functionalization and buffer combinations did not yield the desired combination of a high extraction efficiency and high elution efficiency. Further research can give more clarity in which combination needs to be chosen in order to have the optimal combination. The chip design itself was also not optimal for the extraction of DNA. The column itself was not the problem, but the distributor gave the problems. The chosen distributor has channels of 2.5 μm wide and the depth of the distributor was quite large, when compared to the width, making it prone for clogging. Equation (2.17) learns us that the created pressure drop is related to the viscosity of the fluid. The fact that oil has a higher viscosity, together with the channel dimensions, make it that the oil could not enter the distributor. All recommendations for further research can be found in chapter 6.

Chapter 6

Recommendations and integration

After performing this Master's thesis research it is not surprising that some recommendations for further research are found and that an idea about the integration of such an ion exchange μSPE into the bigger portable DNA analyser for the forensic scientists. Both the recommendations, as well as the integration of the chip are discussed in this chapter.

6.1 Recommendations

After doing this Master's thesis research some recommendations can be made for further research into this topic. First of all, some recommendations are listed for the chip design:

- With regard to the inlet channels before the column. These channels form in the current design a T-junction. It is found in this research, as well as in the literature[203], that this kind junction does not give desired results. It would be better to make an Y-junction with an angle $\sim$45°.
- The distributor in the current design gave a lot of troubles. It is therefore recommended to implement another flow distributor. Although not giving a completely flat flow profile, the bifurcating channels distributor is still a good option. These channels are much wider than the chosen radially interconnected flow distributor, making the pressure drop much lower.
- The last recommendation regarding the chip design is the column length. The extractions which were performed on the test strips needed an area of 8.8 mm^2. This area is roughly 35% smaller than the current column length. Therefore it can be shortened to $\sim$6.5 mm. This also reduces the pressure drop of the column.

There can also be made some recommendation with regard to the functionalization process:

- Instead of using piranha solutions in the chip, the channels can be cleaned and activated using a corona discharge single phase plasma. This method is recently used by Davies *et al.* in their research to locally change the wettability inside a microfluidic chip[240]. The corona discharge plasma gun directs the plasma through the channel to the electrode near the outlet, as can be seen in figure 6.1. Plasma has proven to be useful in creating a hydrophilic surface, as is shown in this research. However, it is only possible to use this method in a fully silica device since silicon is conductive. So such a corona discharge plasma treatment would therefore be recommended when only silica wafers are used in the process.
- It is also recommended to investigate the optimal parameters for the functionalization steps. The C/N ratio of the APTES functionalization increased from 9:1 to 4:1 by only changing the solvent from ethanol to dry toluene. Another interesting parameter is temperature. There are different methods of heating described in the literature[133,134], so it can be interesting to investigate which one is the best suitable in this application.
- Another method can be the use of a clamped system. After etching the channels and the via-holes and dicing the individual chips, the channel can be functionalized via local functionalization techniques. Examples of these techniques are scanning probe lithography[241,242] and the Nano eNabler of BioForce Nanosciences (Ames, IA, United States)[243]. Once the functionalization is done, the glass top is placed on the chip and clamped on all 4 sides of the chip. In this way, a local functionalization can be done on only the micropillar array of the column.
- The last recommendation for the functionalization step is related to the choice of monolayer. APTES was chosen because of its commonly used chemistry and chitosan was chosen because of the proper pK_a value. However, there are more molecules suitable to form SAMs. An example is

aminomethylphosphonic acid (AMPA). This molecule needs less cross-linking during the SAM formation. This molecule is used quite a lot as a stationary phase in the chromatography world[244], so its chemistry on silica is well-established.

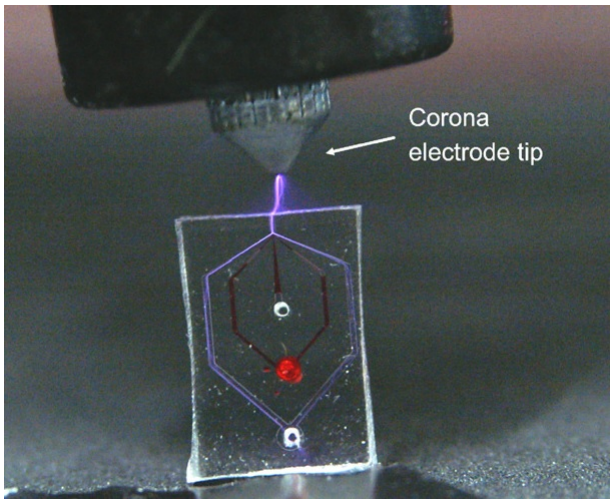

Figure 6.1: A corona discharge plasma arc travels freely from the inlet to the outlet via the unblocked outer channel. Picture taken from reference 240.

Besides these recommendation, there are also some for the characterization of the chip:

- Until now, there is only looked at the reproducibility between different chips. It can also be useful to look at the inter-chip reproducibility, *i.e.* performing multiple extractions with the same chip. With this test, the durability of the functionalization can be tested.
- Also the elution profile of the chips need to be measured. This method is already described before, but there was no functional chip produced during this research. Therefore it is still a recommendation for further research.

6.2 Integration

Once this system is designed in such manner that both the extraction and the elution efficiency are as high as possible, it can be integrated into a forensic LoC device. Such a system can have a sequence that starts with the input. The input can be a collected sample from the crime scene. This sample can be lysed, but the lysis can also be done on chip[245]. The sample then arrives at the μSPE part. Here, all the DNA is extracted from the sample solution, removing all contamination and amplification inhibitors. From here on, the sample is eluted to a flow focussing emulsifier[204,205]. This divides the DNA over a stream of multiple droplets in an oil or air. The stream of droplets goes to the amplification part of the chip. The method which can have a high specificity for human DNA is PCR amplification[227]. There are several *Alu* sequences present in human DNA[246–248] and these can be amplified if the primers are chosen in a proper way. This amplified DNA is mixed with a fluorescent dye and the final mixture can be measured with on-chip fluorescence measurements with a led and a Si photodiode[249].

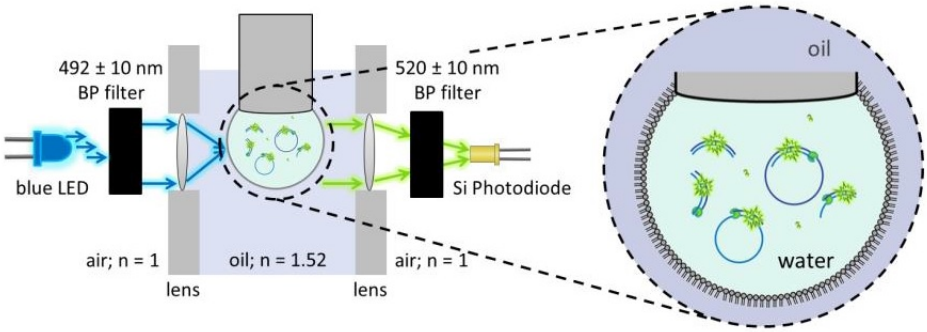

Figure 6.2: Design for fluorescence detection on chip. Picture taken from reference 249.

References

[1] S.C. Terry, J.H. Jerman, and J.B. Angell. A gas chromatographic air analyzer fabricated on a silicon wafer. *IEEE Transactions on electron devices*, 26(12):1880–1886, 1979.

[2] A. Manz, N. Graber, and H.M. Widmer. Miniaturized total chemical analysis systems: a novel concept for chemical sensing. *Sensors and actuators B1*, 1(1–6):244–248, 1990.

[3] A. Manz, Y. Miyahara, J. Miura, Y. Watanabe, H. Miyagi, and K. Sato. Design of an open-tubular column liquid chromatograph using silicon chip technology. *Sensors and actuators B1*, 1(1–6): 249–255, 1990.

[4] I. Moser, G. Jobst, E. Aschauer, P. Svasek, M. Varahram, and G. Urban. Miniaturized thin film glutamate and glutamine biosensors. *Biosensors & bioelectronics*, 10(6–7):527–532, 1995.

[5] G.M. Whitesides. The origins and future of microfluidics. *Nature*, 442(7101):368–373, 2006.

[6] Elsevier. Scopus, January 2014. URL `http://www.scopus.com/`.

[7] Thomson Reuters. Web of science, January 2014. URL `http://apps.webofknowledge.com/`.

[8] S. Shoji, M. Esashi, and T. Matsuo. Prototype miniature blood gas analyser fabricated on a silicon wafer. *Sensors and actuators*, 14(2):101–107, 1988.

[9] R. Zengerle, J. Ulrich, S. Kluge, M. Richter, and A. Richter. A bidirectional silicon micropump. *Sensors and actuators A: physical*, 50(1–2):81–86, 1995.

[10] C.J. Easley, J.M. Karlinsey, J.M. Bienvenue, L.A. Legendre, M.G. Roper, S.H. Feldman, M.A. Hughes, E.L. Hewlett, T.J. Merkel, J.P. Ferrance, and J.P. Landers. A fully integrated microfluidic genetic analysis system with sample-in-answer-out capability. *PNAS*, 103(51):19272–19277, 2006.

[11] A.J. Hopwood, C. Hurth, J. Yang, Z. Cai, N. Moran, J.G. Lee-Edghill, A. Nordquist, R. Lenigk, M.D. Estes, J.P. Haley, C.R. McAlister, X. Chen, C. Brooks, S. Smith, K. Elliot, P. Koumi, F. Zenhausern, and G. Tully. Integrated microfluidic systems for rapid forensic dna analysis: sample collection to dna profile. *Anal. Chem.*, 82(16):6991–6999, 2010.

[12] E.T. Lagally, P.C. Simpson, and R.A. Mathies. Monolithic integrated microfluidic dna amplification and capillary electrophoresis analysis system. *Sensors and actuators B: Chemical*, 63(3):138–146, 2000.

[13] D.R. Reyes, D. Iossifidis, P.-A. Auroux, and A. Manz. Micro total analysis systems. 1. Introduction, theory, and technology. *Anal. Chem.*, 74(12):2623–2636, 2002.

[14] D.C. Duffy, J.C. McDonald, O.J.A. Schueller, and G.M. Whitesides. Rapid prototyping of microfluidic systems in poly(dimethylsiloxane). *Anal. Chem.*, 70(23):4974–4984, 1998.

[15] J. Wang, M. Pumera, M.P. Chatrathi, A. Escarpa, R. Konrad, A. Griebel, W. Dörner, and H. Löwe. Toward dispocable lab-on-a-chip: Poly(methylmethacrylate) microchip electrophoresis device with electrochemical detection. *Electrophoresis*, 23(4):596–601, 2002.

[16] T.J. Johnson, D. Ross, and L.E. Locascio. Rapid microfluidic mixing. *Anal. Chem.*, 74(1):45–51, 2002.

[17] L.E. Locascio, C.E. Perso, and C.S. Lee. Measurement of electroosmotic flow in plastic imprinted microfluid devices and the effect of protein adsorption on flow rate. *J. Chromatogr. A*, 857(1–2): 275–284, 1999.

[18] S.L.R. Barker, M.J. Tarlov, H. Canavan, J.J. Hickman, and L.E. Locascio. Plastic microfluidic devices modified with polyelectrolyte multilayers. *Anal. Chem.*, 72(20):4899–4903, 2000.

[19] D. Nilsson, S. Balslev, and A. Kristensen. A microfluidic dye laser fabricated by nanoimprint lithography in a highly transparent and chemically resistant cyclic-olefin copolymer (COC). *J. Micromech. Microeng.*, 15(2):296–300, 2005.

[20] P.S. Nunes, P.D. Ohlsson, O. Ordeig, and J.P. Kutter. Cyclic olefin polymers: emerging materials for lab-on-a-chip applications. *Microfluidics and nanofluidics*, 9(2–3):145–161, 2010.

[21] H. Becker and L.E. Locascio. Polymer microfluidic devices. *Talanta*, 56(2):267–287, 2002.

[22] S. Franssila. *Introduction to microfabrication*, chapter 18. John Wiley & Sons Ltd., 2 edition, 2010. ISBN 9780470749838.

[23] D. Mijatovic, J.C.T. Eijkel, and A. van den Berg. Technologies for nanofluidic systems: *top-down* vs. *bottom-up* — a review. *Lab Chip*, 5(5):492–500, 2005.

[24] J. Narasimhan and I. Paputsky. Polymer embossing tools for rapid prototyping of plastic microfluidic devices. *J. Micromech. Microeng.*, 14(1):96–103, 2004.

[25] H.A. Stone and S. Kim. Microfluidics: basic issues, applications, and challenges. *AIChE J.*, 47 (6):1250–1254, 2001.

[26] H.A. Stone, A.D. Stroock, and A. Ajdari. Engineering flows in small devices: Microfluidics toward a lab-on-a-chip. *Annu. Rev. Fluid Mech.*, 36(1):381–411, 2004.

[27] A. Huebner, S. Sharma, M. Srisa-Art, F. Hollfelder, J.B. Edel, and A.J. deMello. Microdroplets: a sea of applications? *Lab Chip*, 8(8):1244–1254, 2008.

[28] R. Arayanarakool. *Toward single enzyme analysis in a droplet-based micro and nanofluidic system*. PhD thesis, Universiteit Twente, Enschede, The Netherlands, 2012.

[29] H. Song, J.D. Tice, and R.F. Ismagilov. A microfluidic system for controlling reaction networks in time. *Angew. Chem. Int. Ed.*, 42(7):768–772, 2003.

[30] B. Zheng, L.S. Roach, and R.F. Ismagilov. Screening of protein crystallization conditions on a microfluidic chip using nanoliter-size droplets. *J. Am. Chem. Soc.*, 125(37):11170–11171, 2003.

[31] H. Song and R.F. Ismagilov. Millisecond kinetics on a microfluidic chip using nanoliters of reagents. *J. Am. Chem. Soc.*, 125(47):14613–14619, 2003.

[32] N.R. Beer, B.J. Hindson, E.K. Wheeler, S.B. Hall, K.A. Rose, I.M. Kennedy, and B.W. Colston. On-chip, real-time, single-copy polymerase chain reaction in picoliter droplets. *Anal. Chem.*, 79 (22):8471–8475, 2007.

[33] N.R. Beer, E.K. Wheeler, L. Lee-Houghton, N. Watkins, S. Nasarabadi, N. Hebert, P. Leung, D.W. Arnold, C.G. Bailey, and B.W. Colston. On-chip single-copy real-time reverse-transcription PCR in isolated picoliter droplets. *Anal. Chem.*, 80(6):1854–1858, 2008.

[34] M.M. Kiss, L. Ortoleva-Donnelly, N.R. Beer, J. Warner, C.G. Bailey, B.W. Colston, J.M. Rothberg, D.R. Link, and J.H. Leamon. High-throughput quantitative polymerase chain reaction in picoliter droplets. *Anal. Chem.*, 80(23):8975–8981, 2008.

[35] S. Mohr, Y.-H. Zhang, A. Macaskill, P.J.R. Day, R.W. Barber, N.J. Goddard, D.R. Emerson, and P.R. Fielden. Numerical and experimental study of a droplet-based PCR chip. *Microfluid. Nanofluid.*, 3(5):611–621, 2007.

[36] F. Shen, W. Du, J.E. Kreutz, A. Fok, and R.F. Ismagilov. Digital PCR on a slipChip. *Lab Chip*, 10 (20):2666–2672, 2010.

[37] W. Wang, Z.-X. Li, R. Luo, S.-H. Lü, A.-D. Xu, and Y.-J. Yang. Droplet-based micro oscillating-flow PCR chip. *J. Micromech. Microeng.*, 15(8):1369–1377, 2005.

[38] Y. Zhang and P. Ozdemir. Microfluidic DNA amplification — a review. *Analytica Chimica Acta*, 638 (2):115–125, 2009.

[39] P. Kumaresan, C.J. Yang, S.A. Cronier, R.G. Blazej, and R.A. Mathies. High-throughput single copy DNA amplification and cell analysis in engineered nanoliter droplets. *Anal. Chem.*, 80(10): 3522–3529, 2008.

[40] A.D. Griffiths and D.S. Tawfik. Miniaturising the laboratory in emulsion droplets. *Trends Biotechnol.*, 24(9):395–402, 2006.

[41] B. Zheng, J.D. Tice, and R.F. Ismagilov. Formation of droplets of alternating composition in microfluidic channels and applications to indexing of concentrations in droplet-based assays. *Anal. Chem.*, 76(17):4977–4982, 2004.

[42] D.S. Tawfik and A.D. Griffiths. Man-made cell-like compartments for molecular evolution. *Nat. Biotechnol.*, 16(7):652–656, 1998.

[43] A. Aharoni, A.D. Griffiths, and D.S. Tawfik. High-throughput screens and selections of enzyme-encoding genes. *Curr. Opin. Chem. Biol.*, 9(2):210–216, 2005.

[44] V. Taly, B.T. Kelly, and A.D. Griffiths. Droplets as microreactors for high-throughput biology. *ChemBioChem*, 8(3):263–272, 2007.

[45] H. Song, D.L. Chen, and R.F. Ismagilov. Reactions in droplets in microfluidic channels. *Angew. Chem. Int. Ed.*, 45(44):7336–7356, 2006.

[46] J. Bibette, F.L. Calderon, and P. Poulin. Emulsions: basic principles. *Rep. Prog. Phys.*, 62(6): 969–1033, 1999.

[47] I. Roland, G. Piel, L. Delattre, and B. Evrard. Systematic characterization of oil-in-water emulsions for formulation design. *Int. J. Pharm.*, 263(1–2):85–94, 2003.

[48] H. Tian, A.F.R. Hühmer, and J.P. Landers. Evaluation of silica resins for direct and efficient extraction of DNA from complex biological matrices in a miniaturized format. *Anal. Biochem.*, 283 (2):175–191, 2000.

[49] C. Lui, N.C. Cady, and C.A. Batt. Nucleic acid-based detection of bacterial pathogens using integrated microfluidic platform systems. *Sensors*, 9(5):3713–3744, 2009.

[50] A. Mapes. The expectations within the criminal justice system on the use of mobile DNA-technologies at the crime scene. Master thesis, University of Amsterdam, Amsterdam, The Netherlands, 2012.

[51] T. de Wolff. The influence of using real-time DNA identification of techniques on searching, collecting, and analyzing DNA traces during the crime scene investigation. Master thesis, University of Amsterdam, Amsterdam, The Netherlands, 2013.

[52] Justitie. Jaarverslag. Technical report, Nederlands Forensisch Instituut, 2013. Available online: https://www.forensischinstituut.nl/kenniscentrum/publicaties/jaarverslagen/index.aspx, last accessed 19-May-2014.

[53] K.M. Horsman, J.M. Bienvenue, K.R. Blasier, and J.P. Landers. Forensic DNA analysis on microfluidic devices: a review. *J. Forensic. Sci.*, 52(4):784–799, 2007.

[54] Justitie. Jaarverslag. Technical report, Nederlands Forensisch Instituut, 2007. Available online: https://www.forensischinstituut.nl/kenniscentrum/publicaties/jaarverslagen/index.aspx, last accessed 19-May-2014.

[55] Justitie. Jaarverslag. Technical report, Nederlands Forensisch Instituut, 2008. Available online: https://www.forensischinstituut.nl/kenniscentrum/publicaties/jaarverslagen/index.aspx, last accessed 19-May-2014.

[56] Justitie. Jaarverslag. Technical report, Nederlands Forensisch Instituut, 2009. Available online: https://www.forensischinstituut.nl/kenniscentrum/publicaties/jaarverslagen/index.aspx, last accessed 19-May-2014.

[57] Justitie. Jaarverslag. Technical report, Nederlands Forensisch Instituut, 2010. Available online: https://www.forensischinstituut.nl/kenniscentrum/publicaties/jaarverslagen/index.aspx, last accessed 19-May-2014.

[58] Justitie. Jaarverslag. Technical report, Nederlands Forensisch Instituut, 2012. Available online: https://www.forensischinstituut.nl/kenniscentrum/publicaties/jaarverslagen/index.aspx, last accessed 19-May-2014.

[59] L.A. Legendre, J.M. Bienvenue, M.G. Roper, J.P. Ferrance, and J.P. Landers. A simple, valveless microfluidic sample preparation device for extraction and amplification of DNA from nanoliter-volume samples. *Anal. Chem.*, 78(5):1444–1451, 2006.

[60] J. Cheng, L.C. Waters, P. Fortina, G.E. Hvichia, S.C. Jacobson, J.M. Ramsey, L.J. Kricka, and P. Wilding. Degenerate oligonucleotide primed-polymerase chain reaction and capillary electrophoretic analysis of human DNA on microchip-based devices. *Anal. Biochem.*, 257(2):101–106, 1998.

[61] J. Cheng, M.A. Shoffner, G.E. Hvichia, L.J. Kricka, and P. Wilding. Chip PCR. II. investigation of different PCR amplification systems in microfabricated silicon-glass chips. *Nucl. Acids Res.*, 24 (2):380–385, 1996.

[62] A.T. Woolley, D. Hadley, P. Landre, A.J. deMello, R.A. Mathies, and M.A. Northrup. Functional integration of PCR amplification and capillary electrophoresis in a microfabricated DNA analysis device. *Anal. Chem.*, 68(23):4081–4086, 1996.

[63] P.C. Simpson, D. Roach, A.T. Woolley, T. Thorsen, R. Johnston, G.F. Sensabauch, and R.A. Mathies. High-throughput genetic analysis using microfabricated 96-sample capillary array electrophoresis microplates. *Proc. Natl. Acad. Sci. USA*, 95(5):2256–2261, 1998.

[64] B.C. Giordano, J. Ferrance, S. Swedberg, A.F.R. Hühmer, and J.P. Landers. Polymerase chain reaction in polymeric microchips: DNA amplification in less than 240 seconds. *Anal. Biochem.*, 291(1):124–132, 2001.

[65] N.J. Munro, K. Snow, J.A. Kant, and J.P. Landers. Molecular diagnostics on microfabricated electrophoretic devices: from slab gel- to capillary- to microchip-based assays for t- and b-cell lymphoproliferative disorders. *Clin. Chem.*, 45(11):1906–1917, 1999.

[66] H. Tian, A. Jaquins-Gerstl, N.J. Munro, M. Trucco, L.C. Brody, and J.P. Landers. Single-strand conformation polymorphism analysis by capillary and microchip electrophoresis: a fast, simple method for detection of common mutations in BRCA1 and BRCA2. *Genomics*, 63(1):25–34, 2000.

[67] H. Tian, L.C. Brody, and J.P. Landers. Rapid detection of deletion, insertion, and substitution mutations via heteroduplex analysis using capillary- and microchip-based electrophoresis. *Genome Res.*, 10(9):1403–1413, 2000.

[68] W.T. Hofgärtner, A.F.R. Hühmer, J.P. Landers, and J.A. Kant. Rapid diagnosis of herpes simplex encephalitis using microchip electrophoresis of PCR products. *Clin. Chem.*, 45(12):2120–2128, 1999.

[69] Y. Shi, P.C. Simpson, J.R. Scherer, D. Wexler, C. Skibola, M.T. Smith, and R.A. Mathies. Radial capillary array electrophoresis microplate and scanner for high-performance nucleic acid analysis. *Anal. Chem.*, 71(23):5354–5361, 1999.

[70] A.G. Hadd, S.C. Jacobson, and J.M. Ramsey. Microfluidic assays of acetylcholinesterase inhibitors. *Anal. Chem.*, 71(22):5206–5212, 1999.

[71] J. Khandurina, T.E. McKnight, S.C. Jacobson, L.C. Waters, R.S. Foote, and J.M. Ramsey. Integrated system for rapid PCR-based DNA analysis in microfluidic devices. *Anal. Chem.*, 72(13): 2995–3000, 2000.

[72] X. Chen, D. Cui, and J. Chen. *Microfluidic chips for DNA extraction and purification*, chapter 5. On-chip pretreatment of whole blood by using MEMS technology. Bentham Books, 1 edition, 2012. ISBN 9781608055289.

[73] M.C. Breadmore, K.A. Wolfe, I.G. Arcibal, W.K. Leung, D. Dickson, B.C. Giordano, M.E. Power, J.P. Ferrance, S.H. Feldman, P.M. Norris, and J.P. Landers. Microchip-based purification of DNA from biological samples. *Anal. Chem.*, 75(8):1880–1886, 2003.

[74] J.M. Butler. *Forensic DNA typing*, chapter 3. Elsevier Academic Press, 1 edition, 2005. ISBN 9780121479527.

[75] J. Wen, L.A. Legendre, J.M. Bienvenue, and J.P. Landers. Purification of nucleic acids in microfluidic devices. *Anal. Chem.*, 80(17):6472–6479, 2008.

[76] C.R. Reedy, K.A. Hagan, B.C. Strachen, J.J. Higginson, J.M. Bienvenue, S.A. Greenspoon, J.P. Ferrance, and J.P. Landers. Dual-domain microchip-based process for volume reduction solid phase extraction of nucleic acids from dilute, large volume biological samples. *Anal. Chem.*, 82 (13):5669–5678, 2010.

[77] J.M. Butler. *Forensic DNA typing*, chapter 7. Elsevier Academic Press, 1 edition, 2005. ISBN 9780121479527.

[78] C.W. Price, D.C. Leslie, and J.P. Landers. Nucleic acid extraction techniques and application to the microchip. *Lab Chip*, 9(17):2484–2494, 2009.

[79] J. Wen, C. Guillo, J.P. Ferrance, and J.P. Landers. Microfluidic-based DNA purification in a two-stage, dual-phase microchip containing a reversed-phase and a photopolymerized monolith. *Anal. Chem.*, 79(16):6135–6142, 2007.

[80] P.E. Mason, G.W. Neilson, J.E. Enderby, M.-L. Saboungi, C.E. Dempsey, A.D. MacKerell Jr., and J.W. Brady. The structure of aqueous guanidinium chloride solutions. *J. Am. Chem. Soc.*, 126 (37):11462–11470, 2004.

[81] K.A. Melzak, C.S. Sherwood, R.F.B. Turner, and C.A. Haynes. Driving forces for DNA adsorption to silica in perchlorate solutions. *Journal of Colloid and Interface Science*, 181(2):635–644, 1996.

[82] C.J. Alden and S.-H. Kim. Solvent-accessible surfaces of nucleic acids. *J. Mol. Biol.*, 132(3): 411–434, 1979.

[83] N.C. Cady, S. Stelick, and C.A. Batt. Nucleic acid purification using microfabricated silicon structures. *Biosensors and Bioelectronics*, 19(1):59–66, 2003.

[84] K.A. Hagan, W.L. Meier, J.P. Ferrance, and J.P. Landers. Chitosan-coated silica as solid phase for RNA purification in a microfluidic device. *Anal. Chem.*, 81(13):5249–5256, 2009.

[85] C.R. Reedy, C.W. Price, J. Sniegowski, J.P. Ferrance, M. Begley, and J.P. Landers. Solid phase extraction of DNA from biological samples in a post-based, high surface area poly(methyl methacrylate) (pmma) microdevice. *Lab Chip*, 11(9):1603–1611, 2011.

[86] T. Nakagawa, R. Hashimoto, K. Maruyama, T. Tanaka, H. Takeyama, and T. Matsunaga. Capture and release of DNA using aminosilane-modified bacterial magnetic particles for automated detection system of single nucleatide polymorphisms. *Biotechnology and Bioengineering*, 94(5): 862–868, 2006.

[87] P. Puget. *Lab on a chip*, volume 3 of *Nanoscience*, chapter 20. Springer-Verlag, 1 edition, 2007. ISBN 9783540886327.

[88] Y. Xu, B. Vaidya, A.B. Patel, S.M. Ford, R.L. McCarley, and S.A. Soper. Solid-phase reversible immobilization in microfluidic chips for the purification of dye-labeled DNA sequencing fragments. *Anal. Chem.*, 75(13):2975–2984, 2003.

[89] C.J. Elkin, P.M. Richardson, H.M. Fourcade, N.M. Hammon, M.J. Pollard, P.F. Predki, T. Glavina, and T.L. Hawkins. High-throughput plasmid purification for capillary sequencing. *Genome Res.*, 11(7):1269–1274, 2001.

[90] V. Reddy and J.D. Zahn. Interfacial stabilization of organic–aqueous two-phase microflows for a miniaturized DNA extraction module. *Journal of Colloid and Interface Science*, 286(1):158–165, 2005.

[91] R.D. Oleschuk, L.L. Shultz-Lockyear, Y. Ning, and D.J. Harrison. Trapping of bead-based reagents within microfluidic systems: on-chip solid-phase extraction and electrochromatography. *Anal. Chem.*, 72(3):585–590, 2000.

[92] D. Figeys and R. Aebersold. Nanoflow solvent gradient delivery from a microfabricated device for protein identifications by electrospray ionization mass spectrometry. *Anal. Chem.*, 70(18): 3721–3727, 1998.

[93] C. Yu, M.H. Davey, F. Svec, and J.M.J. Fréchet. Monolithic porous polymer for on-chip solid-phase extraction and preconcentration prepared by photoinitiated in situ polymerization within a microfluidic device. *Anal. Chem.*, 73(21):5088–5096, 2001.

[94] T.B. Stachowiak, T. Rohr, E.F. Hilder, D.S. Peterson, M. Yi, F. Svec, and J.M.J. Fréchet. Fabrication of porous polymer monoliths covalently attached to the walls of channels in plastic microdevices. *Electrophoresis*, 24(21):3689–3693, 2003.

[95] N. Sarrut, S. Bouffet, F. Mittler, O. Constantin, P. Combette, J. Sudor, F. Ricoul, F. Vinet, J. Garin, and C. Vauchier. Enzymatic digestion and liquid chromatography in micro-pillar reactors — hydrodynamic versus electroosmotic flow. In I. Papautsky and I. Chartier, editors, *Proceedings of SPIE: Microfluidics, BioMEMS, and Medical Microsystems III*, volume 5718 of *Proceedings of SPIE*, pages 99–109, Bellingham, WA, USA, 2005. SPIE.

[96] J.M. Bienvenue, N. Duncalf, D. Marchiarullo, J.P. Ferrance, and J.P. Landers. Microchip-based cell lysis and DNA extraction from sperm cells for application to forensic analysis. *J. Forensic Sci.*, 51(2):266–273, 2006.

[97] K.A. Hagan, C.R. Reedy, J.M. Bienvenue, A.H. Dewald, and J.P. Landers. A valveless microfluidic device for integrated solid phase extraction and polymerase chain reaction for short tandem repeat (STR) analysis. *Analyst*, 136(9):1928–1937, 2011.

[98] Y. Liu, N.C. Cady, and C.A. Batt. A plastic microchip for nucleic acid purification. *Biomed. Microdevices*, 9(5):769–776, 2007.

[99] K.A. Wolfe, M.C. Breadmore, J.P. Ferrance, M.E. Power, J.F. Conroy, P.M. Norris, and J.P. Landers. Toward a microchip-based solid-phase extraction method for isolation of nucleic acids. *Electrophoresis*, 23(5):727–733, 2002.

[100] J. Wen, C. Guillo, J.P. Ferrance, and J.P. Landers. DNA extraction using a tetramethyl orthosilicate-grafted photopolymerized monolithic solid phase. *Anal. Chem.*, 78(5):1673–1681, 2006.

[101] M. Benčina, A. Prodgornik, and A. Štrancar. Characterization of methacrylate monoliths for purification of DNA molecules. *J. Sep. Sci.*, 27(10–11):801–810, 2004.

[102] S. Hjertén, J.-L. Liao, and R. Zhang. High-performance liquid chromatography on continuous polymer beds. *J. Chromatogr. A*, 473:273–275, 1989.

[103] T.B. Tennikova, M. Bleha, F. Švec, T.V. Almazova, and B.G. Belenkii. High-performance membrane chromatography of proteins, a novel method of protein separation. *J. Chromatogr. A*, 555 (1–2):97–107, 1991.

[104] F. Svec and J.M.J. Fréchet. Continuous rods of macroporous polymer as high-performance liquid chromatography separation media. *Anal. Chem.*, 64(7):820–822, 1992.

[105] F. Svec and J.M.J. Fréchet. New designs of macroporous polymers and supports: from separation to biocatalysis. *Science*, 273(5272):205–211, 1996.

[106] M. Petro, F. Svec, and J.M.J. Fréchet. Molded continuous poly(styrene-*co*-divinylbenzene) rod as a separation medium for the very fast separation of polymers. comparison of the chromatographic properties of the monolithic rod with columns packed with porous and non-porous beads in high-performance liquid chromatography of polystyrenes. *J. Chromatogr. A*, 752(1–2):59–66, 1996.

[107] C. Yu, F. Svec, and J.M.J Fréchet. Towards stationary phases for chromatography on a microchip: molded porous monoliths prepared in capillaries by photoinitiated *in situ* polymerization as separation media for electrochromatography. *Electrophoresis*, 21(1):120–127, 2000.

[108] C. Viklund, F. Svec, and J.M.J. Fréchet. Monolithic, "molded", porous materials with high flow characteristics for separations, catalysis, or solid-phase chemistry: control of porous properties during polymerization. *Chem. Mater.*, 8(3):744–750, 1996.

[109] K. Morishima, B.D. Bennett, M.T. Dulay, J.P. Quirino, and R.N. Zare. Toward sol-gel electrochromatographic separations on a chip. *J. Sepl. Sci.*, 25(15–17):1226–1230, 2002.

[110] T. Nakagawa, T. Tanaka, D. Niwa, T. Osaka, H. Takeyama, and T. Matsunaga. Fabrication of amino silane-coated microchip for DNA extraction from whole blood. *Journal of Biotechnology*, 116(2):105–111, 2005.

[111] W. Cao, C.J. Easley, J.P. Ferrance, and J.P. Landers. Chitosan as a polymer for pH-induced DNA capture in a totally aqueous system. *Anal. Chem.*, 78(20):7222–7228, 2006.

[112] L.A. Christel, K. Petersen, W. McMillan, and M.A. Northrup. Rapid, automated nucleic acid probe assays using silicon microstructures for nucleic acid concentration. *J. Biomech. Eng.*, 121(1): 22–27, 1999.

[113] B. Yoza, M. Matsumoto, and T. Matsunaga. DNA extraction using modified bacterial magnetic particles in the presence of amino silane compound. *Journal of Biotechnology*, 94(3):217–224, 2002.

[114] B. Yoza, A. Arakaki, and T. Matsunaga. DNA extraction using bacterial magnetic particles modified with hyperbranched polyamidoamine dendrimer. *Journal of Biotechnology*, 101(3):219–228, 2003.

[115] T. Matsunaga. Applications of bacterial magnets. *Trends Biotechnol.*, 9(1):91–95, 1991.

[116] S.E. Williams, P.R. Davies, J.L. Bowen, and C.J. Allender. Controlling the nanoscale patterning of AuNPs on silicon surfaces. *Nanomaterials*, 3(1):192–203, 2013.

[117] K. van der Maaden, K. Sliedregt, A. Kros, W. Jiskoot, and J. Bouwstra. Fluorescent nanoparticle adhesion assay: a novel method for surface pk_a determination of self-assembled monolayers on silicon surfaces. *Langmuir*, 28(7):3403–3411, 2012.

[118] B. Ashcroft, B. Takulapalli, J. Yang, G.M. Laws, H.Q. Zhang, N.J. Tao, S. Lindsay, D. Gust, and T.J. Thronton. Calibration of a pH sensitive buried channel silicon-on-insulator MOSFET for sensor applications. *Phys. Stat. Sol. B*, 241(10):2291–2296, 2004.

[119] L. Nony, R. Boisgard, and J.-P. Aimé. DNA properties investigated by dynamic force microscopy. *Biomacromolecules*, 2(3):827–835, 2001.

[120] Roche Applied Science. Taq DNA polymerase. Online: http://mvz.berkeley.edu/egl/inserts/RocheTaqPolymerase.pdf (last accessed 23-May-2014), November 2005. Datasheet of the Taq polymerase enzyme.

[121] J.W. Park, K.-H. Choi, and K.K. Park. Acid-base equilibria and related properties of chitosan. *Bulletin of Korean Chemical Society*, 4(2):68–72, 1983.

[122] M.L. Hair and W. Hertl. Acidity of surface hydroxyl groups. *J. Phys. Chem.*, 74(1):91–94, 1970.

[123] S. Hashioka, R. Ogawa, H. Ogawa, and Y. Horiike. Integrated DNA purification and detection device for diagnosis of infectious disease. *Jpn. J. Appl. Phys.*, 46(4B):2775–2780, 2007.

[124] J.R. Falsey, M. Renil, S. Park, S. Li, and K.S. Lam. Peptide and small molecule microarray for high throughput cell adhesion and functional assays. *Bioconjugate Chem.*, 12(3):346–353, 2001.

[125] S.D. Conzone and C.G. Pantano. Glass slides to DNA microarrays. *Materials Today*, 7(3):20–26, 2004.

[126] J. Doh and D.J. Irvine. Immunological synapse arrays: patterned protein surfaces that modulate immunological synapse structure formation in t cells. *Proc. Natl. Acad. Sci.*, 103(15):5700–5705, 2006.

[127] H.S. Mansur, W.L. Vasconcelos, R.F.S. Lenza, R.L. Oréfice, E.F. Reis, and Z.P. Lobato. Sol-gel silica based networks with controlled chemical properties. *J. Non-Cryst. Solids*, 273(1–3):109–115, 2000.

[128] J. Bart, R. Tiggelaar, M. Yang, S. Schlautmann, H. Zuilhof, and H. Gardeniers. Room-temperature intermediate layer bonding for microfluidic devices. *Lab Chip*, 9(24):3481–3488, 2009.

[129] Y. Engel, R. Elnathan, A. Pevzner, G. Davidi, E. Flaxer, and F. Patolsky. Supersensitive detection of explosives by silicon nanowire arrays. *Angew. Chem. Int. Ed.*, 49(38):6830–6835, 2010.

[130] J. Kim, P. Seidler, L.S. Wan, and C. Fill. Formation, structure, and reactivity of amino-terminated organic films on silicon substrates. *Journal of Colloid and Interface Science*, 329(1):114–119, 2009.

[131] J. Sagiv. Organized monolayers by adsorption. 1. Formation and structure of oleophobic mixed monolayers on solid surfaces. *J. Am. Chem. Soc.*, 102(1):92–98, 1980.

[132] K.M.R. Kallury, P.M. Macdonald, and M. Thompson. Effect of surface water and base catalysis on the silanization of silica by (aminopropyl)alkoxysilanes studied by X-ray photoelectron spectroscopy and ^{13}C cross-polarization/magic angle spinning nuclear magnetic resonance. *Langmuir*, 10(2):492–499, 1994.

[133] R.M. Pasternack, S.R. Amy, and Y.J. Chabal. Attachment of 3-(aminopropyl)triethoxysilane on silicon oxide surfaces: dependence on solution temperature. *Langmuir*, 24(22):12963–12971, 2008.

[134] E.T. Vandenberg, L. Bertilsson, B. Liedberg, K. Uvdal, R. Erlandsson, H. Elwing, and I. Lundström. Structure of 3-aminopropyl triethoxy silane on silicon oxide. *Journal of Colloid and Interface Science*, 147(1):103–118, 1991.

[135] J.A. Howarter and J.P. Youngblood. Optimization of silica silanization by 3-aminopropyltriethoxysilane. *Langmuir*, 22(26):11142–11147, 2006.

[136] C.-H. Chiang, H. Ishida, and J.L. Koenig. The structure of γ-aminopropyltriethoxysilane on glass surfaces. *Journal of Colloid and Interface Science*, 74(2):396–404, 1980.

[137] P. Herder, Vågberg L., and P. Stenius. ESCA and contact angle studies of the adsorption of aminosilanes on mica. *Colloids Surf.*, 34(2):117–132, 1988/1989.

[138] L.D. White and C.P. Tripp. Reaction of (3-aminopropyl)dimethylethoxysilane with amine catalysts on silica surfaces. *Journal of Colloid and Interface Science*, 232(2):400–407, 2000.

[139] T. Kovalchuk, H. Sfihi, L. Kostenko, V. Zaitsev, and J. Fraissard. Preparation, structure and thermal stability of onium- and amino-functionalized silicas for the use as catalysts supports. *Journal of Colloid and Interface Science*, 302(1):214–229, 2006.

[140] S.R. Culler, H. Ishida, and J.L. Koenig. Structure of silane coupling agents adsorbed on silicon powder. *Journal of Colloid and Interface Science*, 106(2):334–346, 1985.

[141] S.R. Culler, H. Ishida, and J.L. Koenig. FT-IR characterization of the reaction at the silane/matrix resin interphase of composite materials. *Journal of Colloid and Interface Science*, 109(1):1–10, 1986.

[142] Ch. Weigel and R. Kellner. FTIR-ATR-spectroscopic investigation of the silanization of germanium surfaces with 3-aminopropyltriethoxysilane. *Fresenius Z. Anal. Chem.*, 335(7):663–668, 1989.

[143] R. Peña Alonso, F. Rubio, J. Rubio, and J.L. Oteo. Study of the hydrolysis and condensation of γ-aminopropyltriethoxysilane by FT-IR spectroscopy. *J. Mater. Sci.*, 42(2):595–603, 2007.

[144] D.G. Kurth and T. Bein. Surface reactions on thin layers of silane coupling agents. *Langmuir*, 9 (11):2965–2973, 1993.

[145] S.-H. Choi and B.-M. Zhang Newby. Suppress polystyrene thin film dewetting by modifying substrate surface with aminopropyltriethoxysilane. *Surf. Sci.*, 600(6):1391–1404, 2006.

[146] N.K. Kamisetty, S.P. Pack, M. Nonogawa, K.C. Devarayapalli, T. Kodaki, and K. Makino. Development of an efficient amine-functionalized glass platform by additional silanization treatment with alkylsilane. *Anal. Bioanal. Chem.*, 386(6):1649–1655, 2006.

[147] C.-H. Chiang, N.-I. Liu, and J.L. Koenig. Magic-angle cross-polarization carbon 13 NMR study of aminosilane coupling agents on silica surfaces. *Journal of Colloid and Interface Science*, 86(1): 26–34, 1982.

[148] P. Dhawade and R. Jagtap. Comparative study of physical and thermal properties of chitosan-silica hybrid coatings prepared by sol-gel method. *Der Chemica Sinica*, 3(3):589–601, 2012.

[149] J.D. Bumgardner, R. Wiser, S.H. Elder, R. Jouett, Y. Yang, and J.L. Ong. Contact angle, protein adsorption and osteoblast precursor cell attachment to chitosan coatings bonded to titanium. *J. of Biomater. Sci. Polymer Edn.*, 14(12):1401–1409, 2003.

[150] I. Aranaz, M. Mengíbar, R. Harris, I. Paños, B. Miralles, N. Acosta, G. Galed, and Á Heras. Functional characterization of chitin and chitosan. *Curr. Chem. Biol.*, 3(2):203–230, 2009.

[151] G.S. Silva, P.C. Oliveira, D.S. Giordani, and H.F. de Castro. Chitosan/siloxane hybrid polymer: synthesis, characterization and performance as a support for immobilizing enzyme. *J. Braz. Chem. Soc.*, 22(8):1407–1407, 2011.

[152] K.R. Krishnapriya and M. Kandaswamy. Synthesis and characterization of a crosslinked chitosan derivative with a complexing agent and its adsorption studies toward metal(II) ions. *Carbohydr. Res.*, 344(13):1632–1638, 2009.

[153] I. Leceta, P. Guerrero, and K. de la Caba. Functional properties of chitosan-based films. *Carbohydrate polymers*, 93(1):339–349, 2013.

[154] M. Rinaudo. Chitin and chitosan: properties and applications. *Prog. Polym. Sci.*, 31(7):603–632, 2006.

[155] X.-L. Luo, J.-J. Xu, Q. Zhang, G.-J. Yang, and H.-Y. Chen. Electrochemically deposited chitosan hydrogel for horseradish peroxidase immobilization through gold nanoparticles self-assembly. *Biosens. Bioelectron.*, 21(1):190–196, 2005.

[156] S.B. Rao and C.P. Sharma. Use of chitosan as a biomaterial: studies on its safety and hemostatic potential. *Journal of Biomedical Materials Research*, 34(1):21–28, 1997.

[157] Z. Deng, Z. Zhen, X. Hu, S. Wu, Z. Xu, and P.K. Chu. Hollow chitosan-silica nanospheres as pH-sensitive targeted delivery carriers in breast cancer therapy. *Biomaterials*, 32(21):4976–4986, 2011.

[158] X. Hu, Y. Wang, and B. Peng. Chitosan-capped mesoporous silica nanoparticles as pH-responsive nanocarriers for controlled drug release. *Chem. Asian J.*, 9(1):319–327, 2014.

[159] P. Innocenzi and T. Kidchob. Hybrid organic-inorganic sol-gel materials based on epoxy-amine systems. *J. Sol-Gel Sci. Techn.*, 35(3):225–235, 2005.

[160] G. Toskas, C. Cherif, R.-D. Hund, E. Laourine, B. Mahltig, A. Fahmi, C. Heinemann, and T. Hanke. Chitosan(PEO)/silica hybrid nanofibers as a potential biomaterial for bone regeneration. *Carbohydrate Polymers*, 94(2):713–722, 2013.

[161] F.A. Carey. *Organic Chemistry*, chapter 16. McGraw-Hill Higher Education, 4 edition, 2000. ISBN 0072905018.

[162] L.S. Connell, F. Romer, M. Suárez, E.M. Valliant, Z. Zhang, P.D. Lee, M.E. Smith, J.V. Hanna, and J.R. Jones. Chemical characterisation and fabrication of chitosan–silica hybrid scaffolds with 3-glycidoxypropyl trimethoxysilane. *J. Mater. Chem. B*, 2(6):668–680, 2014.

[163] Y. Shirosaki, K. Tsuru, S. Hayakawa, A. Osaka, M.A. Lopes, J.D. Santos, M.A. Costa, and M.H. Fernandes. Physical, chemical and in vitro biological profile of chitosan hybrid membrane as a function of organosiloxane concentration. *Acta Biomater.*, 5(1):346–355, 2009.

[164] Y.-L. Liu, Y.-H. Su, and J.-Y. Lai. In situ crosslinking of chitosan and formation of chitosan–silica hybrid membranes with using γ-glycidoxypropyltrimethoxysilane as a crosslinking agent. *Polymer*, 45(20):6831–6837, 2004.

[165] A.-C. Chao. Preparation of porous chitosan/GPTMS hybrid membrane and its application in affinity sorption for tyrosinase purification with *Agaricus bisporus*. *J. Membr. Sci.*, 311(1–2):306–318, 2008.

[166] J.G. Varghese, R.S. Karuppannan, and M.Y. Kariduraganavar. Development of hybrid membranes using chitosan and silica precursors for pervaporation separation of water + isopropanol mixtures. *J. Chem. Eng. Data*, 55(6):2084–2092, 2010.

[167] S. Spirk, G. Findenig, A. Doliska, V.E. Reichel, N.L. Swanson, R. Kargl, V. Ribitsch, and K. Stana-Kleinschek. Chitosan-silane sol-gel hybrid thin films with controllable layer thickness and morphology. *Carbohydrate Polymers*, 93(1):285–290, 2013.

[168] F. Al-Sagheer and S. Muslim. Thermal and mechanical properties of chitosan/SiO_2 hybrid composites. *J. Nanomater.*, 2010(3):1–8, 2010.

[169] S.S. Rashidova, D.S. Shakarova, O.N. Ruzimuradov, D.T. Satubaldieva, S.V. Zalyalieva, O.A. Shpigun, V.P. Varlamov, and B.D. Kabulov. Bionanocompositional chitosan-silica sorbent for liquid chromatography. *J. Chromatogr. B*, 800(1–2):49–53, 2004.

[170] G. Poologasundarampillai, C. Ionescu, O. Tsigkou, M. Murugesan, R.G. Hill, M.M. Stevens, J.V. Hanna, M.E. Smith, and J.R. Jones. Synthesis of bioactive class II poly(γ-glutamic acid)/silica hybrids for bone regeneration. *J. Mater. Chem.*, 20(40):8952–8961, 2010.

[171] U. Lehmann, C. Vandevyver, V.K. Parashar, and M.A.M. Gijs. Droplet-based DNA purification in a magnetic lab-on-a-chip. *Angew. Chem. Int. Ed.*, 45(19):3062–3067, 2006.

[172] D. Arpita. *Electronic DNA detection and diagnostics*. PhD thesis, Universiteit Twente, Enschede, The Netherlands, 2013.

[173] C.R. Reedy, J.M. Bienvenue, L. Coletta, B.C. Strachan, N. Bhatri, S. Greenspoon, and J.P. Landers. Volume reduction solid phase extraction of DNA from dilue, large-volume biological samples. *Forensic Science International: Genetics*, 4(3):206–212, 2010.

[174] P. Teeninga. Detection of nucleic acids. Lab-on-a-chip for forensics. Bachelor thesis, Saxion University of Applied Sciences, Enschede, The Netherlands, 2012.

[175] S.C. Jacobson, R. Hergenröder, L.B. Koutny, R.J. Warmack, and J.M. Ramsey. Effects of injection schemes and column geometry on the performance of microchip electrophoresis devices. *Anal. Chem.*, 66(7):1107–1113, 1994.

[176] B. Baidya, T. Mukherjee, and J.F. Hoburg. Dispersion modeling in microfluidic channels for system-level optimization. *International Conference on Modeling and Simulation of Microsystems - MSM 2002*, pages 182–185, 2002.

[177] G. Goranovic and H. Bruus. *Simulations in microfluidics*, chapter 5. Microsystem engineering of lab-on-a-chip devices. John Wiley & Sons Ltd., 1 edition, 2006. ISBN 9783527606368.

[178] P.S. Williams, S.B. Giddings, and J.C. Giddings. Calculation of flow properties and end effects in field-flow fractioning channels by a conformal mapping procedure. *Anal. Chem.*, 58(12):2397–2403, 1986.

[179] B. He, N. Tait, and F. Regnier. Fabrication of nanocolumns for liquid chromatography. *Anal. Chem.*, 70(18):3790–3797, 1998.

[180] J. Vangelooven. *Optimal pillar configurations for on-chip chromatographic separation beds and flow distributors*. PhD thesis, Vrije Universiteit Brussel, Brussels, Belgium, 2010.

[181] J. Vangelooven, S. Schlautmann, F. Detobel, H. Gardeniers, and G. Desmet. Experimental optimization of flow distributors for pressure-driven separations and reactions in flat-rectangular microchannels. *Anal. Chem.*, 83(2):467–477, 2011.

[182] J. Vangelooven, W. de Malsche, J. op de Beeck, H. Eghbali, H. Gardeniers, and G. Desmet. Design and evaluation of flow distributors for microfabricated pillar array columns. *Lab Chip*, 10 (3):349–356, 2010.

[183] H. Bruus. *Theoretical microfluidics*, chapter 3. Oxford University Press, 1 edition, 2007. ISBN 9780199235087.

[184] B.R. Munson, D.F. Young, T.H. Okiishi, and W.W. Huebsch. *Fundamentals of fluid mechanics*, chapter 1. John Wiley & Sons Ltd., 6 edition, 2009. ISBN 9780470398814.

[185] C.L.M.H. Navier. Memoire sur les lois du mouvement des fluides. *Mem. Acad. Sci. Inst. France*, 6:389–440, 1827.

[186] S.D. Poisson. Mémoire sur les équations générales de l'équilibre et du mouvement des corps solides élastiques et des fluids. *Journal de l'École Polytechnique Paris*, 13:1–174, 1831.

[187] A.J.C.B. de Saint-Venant. Mémoire sur la dynamique des fluides. *C. R. Acad. Sci. Paris*, 17: 1240–1242, 1843.

[188] G.G. Stokes. On the theories of the internal friction of fluids in motion, and of the equilibrium and motion of elastic solids. *Trans. Cambridge Philos. Soc.*, 8:287–319, 1845.

[189] B.R. Munson, D.F. Young, T.H. Okiishi, and W.W. Huebsch. *Fundamentals of fluid mechanics*, chapter 6. John Wiley & Sons Ltd., 6 edition, 2009. ISBN 9780470398814.

[190] E. Oosterbroek. *Modeling, design and realization of microfluidic components*. PhD thesis, University of Twente, Enschede, The Netherlands, 1999.

[191] O. Reynolds. An experimental investigation of the circumstances which determine whether the motion of water shall be direct of sinuous, and of the law of resistance in parallel channels. *Phil. Trans. R. Soc. Lond.*, 174:935–982, 1883.

[192] H. Bruus. *Theoretical microfluidics*, chapter 4. Oxford University Press, 1 edition, 2007. ISBN 9780199235087.

[193] S.G. Kandlikar, S. Garimella, D. Li, S. Colin, and M.R. King. *Heat transfer and fluid flow in minichannels and microchannels*, chapter 3. Elsevier Ltd., 2 edition, 2014. ISBN 9780080983462.

[194] G. Barnes and I. Gentle. *Interfacial science: an introduction*, chapter 4. Oxford University Press, 2 edition, 2011. ISBN 9780199571185.

[195] H. Gu. *Controlling two-phase flow in microfluidic systems using electrowetting*. PhD thesis, University of Twente, Enschede, The Netherlands, 2011.

[196] A. Serizawa, Z. Feng, and Z. Kawara. Two-phase flow in microchannels. *Exp. Therm. Fluid Sci.*, 26(6–7):703–714, 2002.

[197] H. Gu, M.H.G. Duits, and F. Mugele. Droplets formation and merging in two-phase flow microfluidics. *Int. J. Mol. Sci.*, 12(4):2572–2597, 2011.

[198] H. Gu, F. Malloggi, S.A. Vanapalli, and F. Mugele. Electrowetting-enhanced microfluidic device for drop generation. *Appl. Phys. Lett.*, 93(18):183507:1–183507:3, 2008.

[199] H. Gu and F. Duits, M.H.G. Mugele. A hybrid microfluidic chip with electrowetting functionality using ultraviolet (uv)-curable polymer. *Lab Chip*, 10(12):1550–1556, 2010.

[200] T. Thorsen, R.W. Roberts, F.H. Arnold, and S.R. Quake. Dynamic pattern formation in a vesicle-generating microfluidic device. *Phys. Rev. Lett.*, 86(18):4163–4166, 2001.

[201] M.L.J. Steegmans, K.G.P.H. Schroën, and R.M. Boom. Characterization of emulsification at flat microchannel Y junctions. *Langmuir*, 25(6):3396–3401, 2009.

[202] M.L.J. Steegmans, A. Warmerdam, K.G.P.H. Schroën, and R.M. Boom. Dynamic interfacial tension measurements with microfluidic Y-junctions. *Langmuir*, 25(17):9751–9758, 2009.

[203] M.L.J. Steegmans. *Emulsification in microfluidic Y- and T-junctions*. PhD thesis, Universiteit Twente, Enschede, The Netherlands, 2009.

[204] S.L. Anna, N. Bontoux, and H.A. Stone. Formation of dispersions using "flow focusing" in microchannels. *Appl. Phys. Lett.*, 82(3):364–366, 2003.

[205] R. Dreyfus, P. Tabeling, and H. Willaime. Ordered and disordered patterns in two-phase flows in microchannels. *Phys. Rev. Lett.*, 90(14):144505:1–144505:4, 2003.

[206] P. Garstecki, M.J. Fuerstman, H.A. Stone, and G.M. Whitesides. Formation of droplets and bubbles in a microfluidic t-junction–scaling and mechanism of break-up. *Lab Chip*, 6(5):437–446, 2006.

[207] W. Lee, L.M. Walker, and S.L. Anna. Role of geometry and fluid properties in droplet and thread formation processes in planar flow focusing. *Phys. Fluids*, 21(3):032103:1–032103:14, 2003.

[208] T. Ward, M. Faivre, M. Abkarian, and H.A. Stone. Microfluidic flow focusing: drop size and scaling in pressure versus flow-rate-driven pumping. *Electrophoresis*, 26(19):3716–3724, 2005.

[209] J. Collins and A.P. Lee. Control of serial microfluidic droplet size gradient by step-wise ramping of flow rates. *Microfluid. Nanofluid.*, 3(1):19–25, 2007.

[210] J.D. Tice, A.D. Lyon, and R.F. Ismagilov. Effects of viscosity on droplet formation and mixing in microfluidic channels. *Anal. Chim. Acta*, 507(1):73–77, 2004.

[211] T. Cubaud and T.G. Mason. Capillary threads and viscous droplets in square microchannels. *Phys. Fluids*, 20(5):053302:1–053302:11, 2008.

[212] Z. Nie, M. Seo, S. Xu, P.C. Lewis, M. Mok, E. Kumacheva, G.M. Whitesides, P. Garstecki, and H.A. Stone. Emulsification in a microfluidic flow-focusing device: effect of the viscosities of the liquids. *Microfluid. Nanofluid.*, 5(5):585–594, 2008.

[213] J.-C. Baret, F. Kleinschmidt, A. El Harrak, and A.D. Griffiths. Kinetic aspects of emulsion stabilization by surfactants: a microfluidic analysis. *Langmuir*, 25(11):6088–6093, 2009.

[214] L. Shui, A. van den Berg, and J.C.T. Eijkel. Interfacial tension controlled w/o and o/w 2-phase flows in microchannel. *Lab Chip*, 9(6):795–801, 2009.

[215] L.S. Roach, H. Song, and R.F. Ismagilov. Controlling nonspecific protein adsorption in a plug-based microfluidic system by controlling interfacial chemistry using fluorous-phase surfactants. *Anal. Chem.*, 77(3):785–796, 2005.

[216] M.J. Rosen. *Surfactants and interfacial phenomena*, chapter 1. John Wiley & Sons Inc., 3 edition, 2004. ISBN 9780471478188.

[217] the free encyclopedia Wikipedia. Surfactant, June 2014. URL `http://en.wikipedia.org/wiki/Surfactant`.

[218] S. Giglio, P.T. Monis, and C.P. Saint. Demonstration of preferential binding of SYBR Green I to specific DNA fragments in real-time multiplex PCR. *Nucl. Acids Res.*, 31(22):e136:1–e136:5, 2003.

[219] I. Johnson and M.T.Z. Spence. *The molecular probes handbook: a guide to fluorescent probes and labeling technologies*, chapter 8. Invitrogen, 11 edition, 2010. ISBN 9780982927915.

[220] Invitrogen by Life Technologies. Qubit® dsDNA HS reagent ∗200x concentrate in DMSO∗, May 2013. Product code Q32851COMPA.

[221] Invitrogen by Life Technologies. Qubit® dsDNA HS assay kit product page, June 2014. URL `http://www.lifetechnologies.com/order/catalog/product/Q32854`.

[222] Q.Z. Wang, X.G. Chen, N. Liu, S.X. Wang, C.S. Liu, X.H. Meng, and C.G. Liu. Protonation constants of chitosan with different molecular weight and degree of deacetylation. *Carhyd. Polym.*, 65(2):194–201, 2006.

[223] M. Rinaudo, G. Pavlov, and J. Desbrières. Influence of acetic acid concentration on the solubilization of chitosan. *Polymer*, 40(25):7029–7032, 1999.

[224] Invitrogen by Life Technologies. Qubit 2.0 fluorometer, for your precious samples and high-value applications, . URL http://www.ebc.uu.se/digitalAssets/120/120354_qubitbrochure.pdf.

[225] Invitrogen by Life Technologies. Qubit assays quick reference card, . URL https://www.lifetechnologies.com/content/dam/LifeTech/migration/en/filelibrary/cell-tissue-analysis/qubit-all-file-types.par.47595.file.dat/mp39808-qubit-2-qrc.pdf.

[226] R.D. Bowman and N. Davidson. Hydrodynamic shear breakage of DNA. *Biopolymers*, 11(12): 2601–2624, 1972.

[227] J.M. Butler. *Forensic DNA typing*, chapter 4. Elsevier Academic Press, 1 edition, 2005. ISBN 9780121479527.

[228] W. de Malsche, D. Clicq, V. Verdoold, P. Gzil, G. Desmet, and H. Gardeniers. Integration of porous layers in ordered pillar arrays for liquid chromatography. *Lab Chip*, 7(12):1705–1711, 2007.

[229] J.F. Watts and J. Wolstenholme. *An introduction to surface analysis by XPS and AES*, chapter 1. John Wiley & Sons Ltd., 1 edition, 2003. ISBN 0470847123.

[230] S. Franssila. *Introduction to microfabrication*, chapter 12. John Wiley & Sons Ltd., 2 edition, 2010. ISBN 9780470749838.

[231] F. Zhang, M.G. Kibria, K. Cornier, and M.M.R. Howlader. Surface and interface characterization of sequenstially plasma activated silicon, silicon dioxide and germanium wafers for low temperature bonding applications. *ECS Transactions*, 33(4):329–338, 2010.

[232] Y. Xia, M. Mrksich, E. Kim, and G.M. Whitesides. Microcontact printing of octadecylsiloxane on the surface of silicon dioxide and its application in microfabrication. *J. Am. Chem. Soc.*, 117(37): 9576–9577, 1995.

[233] K.K.. Lee. Surface modification of silicon and PDMS surfaces with vapor phase deposited ultrathin fluoropolymer and flluorosilane films for biomedical micro/nanoelectromechanical system applications. Master thesis, The Ohio State University, Columbus, OH, United States, 2005.

[234] Y. Wang and M. Ferrari. Surface modification of micromachined silicon filters. *J. Mater. Sci.*, 35 (19):4923–4930, 2000.

[235] M. Lazghab, K. Saleh, and P. Guigon. Functionalisation of porous silica powders in a fluidised-bed reactor with glycidoxypropyltrimethoxysilane (GPTMS) and aminopropyltriethoxysilane (APTES). *Chem. Eng. Res. Des.*, 88(5–6):686–692, 2010.

[236] E.A. El-Hefian, M.M. Nasef, and A.H. Yahaya. Preparation and characterization of chitosan/poly(vinyl alcohol) bleded films: mechanical thermal and surface investigations. *E-J. Chem.*, 8(1):91–96, 2011.

[237] X. Zeng, G. Xu, Y. Gao, and Y. An. Surface wettability of (3-aminopropyl)triethoxysilane self-assembled monolayers. *J. Phy. Chem. B*, 115(3):450–454, 2011.

[238] Princeton University. Section 10: chemical specific information, piranha solutions, July 2014. URL http://web.princeton.edu/sites/ehs/labsafetymanual/cheminfo/piranha.htm.

[239] University of Cambridge. Procedure on handling and using acid piranha solution, July 2014. URL http://www.ch.cam.ac.uk/sites/ch/files/users/meg27/DSO017C%20Acid%20Piranha%20Solution%200911.pdf.

[240] R.T. Davies, D. Kim, and J. Park. Formation of liposomes using a 3D flow focusing microfluidic device with spatially patterned wettability by corona discharge. *J. Micromech. Microeng.*, 22(5): 055003–1–055003–8, 2012.

[241] G.-Y. Liu, S. Xu, and Y. Qian. Nanofabrication of self-assembled monolayers using scanning probe lithography. *Acc. Chem. Res.*, 33(7):457–466, 2000.

[242] S. Krämer, R.R. Fuierer, and C.B. Gorman. Scanning probe lithography using self-assembled monolayers. *Chem. Rev.*, 103(11):4367–4418, 2003.

[243] BioForce Nanosciences. Nano eNabler molecular printing system, July 2014. URL http://bioforcenano.com/product/nano-enabler-molecular-printing-system/.

[244] P.N. Nesterenko, M.J. Shaw, S.J. Hill, and P. Jones. Aminophosphate-functionalized silica: a versatile chromatographic stationary phase for high-performance chelation ion chromatography. *Microchem. J.*, 62(1):58–69, 1999.

[245] S. le Gac and A. van den Berg. *Cell capture and lysis on chip*, volume 15 of *Unravelling single cell genomics: micro and nanotools*, chapter 12. RSC Publishing, 1 edition, 2010. ISBN 9781849732284.

[246] I.Y. Khitrinskaya, V.A. Stepanov, and V.P. Puzyrev. *Alu* repeats in the human genome. *Mol. Biol.*, 37(3):325–333, 2003.

[247] M.A. Batzer and P.L. Deininger. Alu repeats and human genomic diversity. *Nat. Rev. Genet.*, 3 (5):370–379, 2002.

[248] D.J. Rowold and R.J. Herrera. *Alu* elements and the human genome. *Genetica*, 108(1):57–72, 2000.

[249] D.K. Harshman, R. Reyes, and J.-Y. Yoon. Direct detection of plasmid-mediated antibiotic resistance in bloodstream infection by PCR using wire-guided droplet manipulation (WDM). In R. Zengerle, editor, *μTAS 2013*, volume 17, pages 470–472, Freiburg-Black Forest, Germany, 2013.

[250] PhD Comics. Comic 1715, July 2014. URL `http://phdcomics.com/comics/archive.php?comicid=1715`.

[251] S. Franssila. *Introduction to microfabrication*, chapter 21. John Wiley & Sons, 2 edition, 2010. ISBN 9780470749838.

[252] T. Sugizaki, M. Kobayashi, M. Ishidao, H. Minakata, M. Yamaguchi, Y. Tamura, Y. Sugiyama, T. Nakanishi, and H. Tanaka. Novel multi-bit SONOS type flash memory using a high-k charge trapping layer. In The IEEE Electron Devices Society The Japan Society of Applied Physics, editor, *2003 Symposium on VLSI technology, digest of technical papers*, pages 27–28, Kyoto, Japan, 2003. The Japan Society of Applied Physics.

[253] S.-L. Wu (of Vanguard International Semiconductor Company). Method to form a capacitor having multiple pillars for advanced DRAMS. *US Patent No. 5,650,351*, 1996.

[254] T.W. O'Keeffe and R.M. Handy. Fabrication of planar silicon transistors without photoresist. *Solid-State Electronics*, 11(2):261–266, 1968.

[255] Y. Huang, A.S. Ergun, E. Hæggström, M.H. Badi, and B.T. Khuri-Yakub. Fabricating capacitive micromachined ultrasonic transducers with wafer-bonding technology. *Journal of microelectromechanical systems*, 12(2):128–137, 2003.

[256] B.E. Deal and A.S. Grove. General relationship for the thermal oxidation of silicon. *Journal of applied physics*, 36(12):3770–3778, 1965.

[257] T. Watanabe and I. Ohdomari. A kinetic equation for thermal oxidation of silicon replacing the deal-grove equation. *Journal of the Electrochemical Society*, 154(12):G270–G276, 2007.

[258] R.C. Jaeger. *Introduction to microelectronic fabrication*, volume 5 of *Modular series on solid state devices*, chapter 3. Prentice Hall, Inc., 2 edition, 2002. ISBN 9780201444940.

[259] S. Franssila. *Introduction to microfabrication*, chapter 9. John Wiley & Sons, 2 edition, 2010. ISBN 9780470749838.

[260] F. Laermer and A. (of Robert Bosch GmbH) Schilp. Method of anisotropically etching silicon. *US Patent No. 5,501,893*, 1994.

[261] R. Abdolvand and F. Ayazi. An advanced reactive ion etching process for very high aspect-ratio sub-micron wide trenches in silicon. *Sensors and Actuators A*, 144:109–116, 2008.

[262] K.J. Owen, B. van der Elzen, R.L. Peterson, and K. Najafi. High aspect ratio deep silicon etching. In IEEE, editor, *2012 IEEE 25th International Conference on Micro Electro Mechanical Systems (MEMS)*, volume 25, pages 251–254, Paris, France, 2012. IEEE.

[263] S. Franssila. *Introduction to microfabrication*, chapter 17. John Wiley & Sons, 2 edition, 2010. ISBN 9780470749838.

[264] M.A. Schmidt. Wafer-to-wafer bonding for microstructure formation. *Proceedings of the IEEE*, 86 (8):1575–1585, 1998.

[265] T. Rogers and J. Kowal. Selection of glass, anodic bonding conditions and material compatibility for silicon-glass capacitive sensors. *Sensors and Actuators A*, 46(1–3):113–120, 1995.

[266] T.M.H. Lee, D.H.Y. Lee, C.Y.N. Liaw, A.I.K. Lao, and I.-M. Hsing. Detailed characterization of anodic bonding process between glass and thin-film coated silicon substrates. *Sensors and Actuators*, 86(1–2):103–107, 2000.

[267] R.C. Frye, J.E. Griffith, and Y.H. Wong. A field-assisted bonding process for silicon dielectric isolation. *J. Electrochem. Soc.*, 133(8):1673–1677, 1986.

[268] J. Wei, H. Xie, M.L. Nai, C.K. Wong, and L.C. Lee. Low temperature wafer anodic bonding. *J. Micromech. Microeng.*, 13(2):217–222, 2003.

[269] M.X. Chen, X.J. Yi, Z.Y. Gan, and S. Liu. Reliability of anodically bonded silicon-glass packages. *Sensors and Actuators A*, 120(1):291–295, 2005.

[270] W.C. Bigelow, D.L. Pickett, and W.A. Zisman. Oleophobic monolayers. i. films adsorbed from solution in non-polar liquids. *J. Colloid Sci.*, 1(6):513–538, 1946.

[271] E.E. Polymeropoulos and J. Sagiv. Electrical conduction through adsorbed monolayers. *J. Chem. Phys.*, 69(5):1836–1847, 1978.

[272] J.J. Pesek, M.T. Matyska, M. Oliva, and M. Evanchic. Synthesis and characterization of bonded phases made via hydrosilation of alkynes on silica hydride surfaces. *J. Chromatogr. A*, 818(2): 145–154, 1998.

[273] J.M. Buriak. Organometallic chemistry on silicon and germanium surfaces. *Chemical Reviews*, 102(5):1271–1308, 2002.

[274] A.B. Sieval, R. Linke, H. Zuilhof, and E.J.R. Sudhölter. High-quality alkyl monolayers on silicon surfaces. *Advanced Materials*, 12(19):1457–1460, 2000.

[275] R.L. Cicero, M.R. Linford, and C.E.D. Chidsey. Photoreactivity of unsaturated compounds with hydrogen-terminated silicon(111). *Langmuir*, 16(13):5688–5695, 2000.

[276] M.M. Sung, G.J. Kluth, O.W. Yauw, and R. Maboudian. Thermal behavior of alkyl monolayers on silicon surfaces. *Langmuir*, 13(23):6164–6168, 1997.

[277] G.S. Higashi, Y.J. Chabal, G.W. Trucks, and K. Raghavachari. Ideal hydrogen termination of the Si (111) surface. *Appl. Phys. Lett.*, 56(7):656–658, 1990.

[278] K.-I. Iimura, Y. Nakajima, and T. Kato. A study on structures and formation mechanisms of self-assembled monolayers of *n*-alkyltrichlorosilanes using infrared spectroscopy and atomic force microscopy. *Thin Solid Films*, 379(1–2):230–239, 2000.

[279] J.J. Cras, C.A. Rowe-Taitt, D.A. Nivens, and F.S. Ligler. Comparison of chemical cleaning methods of glass in preparation for silanization. *Biosensors & Bioelectronics*, 14(8–9):683–688, 1999.

[280] M. Hu, S. Noda, T. Okubo, Y. Yamaguchi, and H. Komiyama. Structure and morphology of self-assembled 3-mercaptopropyltrimethoxysilane layers on silicon oxide. *Applied Surface Science*, 181(3–4):307–316, 2001.

[281] G. Ledung, M. Bergkvist, A.P. Quist, U. Gelius, J. Carlsson, and S. Oscarsson. A novel method for preparation of disulfides on silicon. *Langmuir*, 17(20):6056–6058, 2001.

[282] E.L. Schmid, T.A. Keller, Z. Dienes, and H. Vogel. Reversible oriented surface immobilization of functional proteins on oxide surfaces. *Anal. Chem.*, 69(11):1979–1985, 1997.

[283] H.-G. Hong, M. Jiang, S.G. Sligar, and P.W. Bohn. Cysteine-specific surface tethering of genetically engineered cytochromes for fabrication of metalloprotein nanostructures. *Langmuir*, 10(1): 153–158, 1994.

[284] E. Pavlovic, A.P. Quist, U. Gelius, and S. Oscarsson. Surface functionalization of silicon oxide at room temperature and atmospheric pressure. *Journal of colloid and interface science*, 254(1): 200–203, 2002.

[285] R.R. Rye, G.C. Nelson, and M.T. Dugger. Mechanistic aspects of alkylschlorosilane coupling reactions. *Langmuir*, 13(11):2965–2972, 1997.

[286] X. Zhao and R. Kopelman. Mechanism of organosilane self-assembled monolayer formation on silica studied by second-harmonic generation. *J. Phys. Chem.*, 100(26):11014–11018, 1996.

[287] D. Borah, M. Ozmen, S. Rasappa, M.T. Shaw, J.D. Holmes, and M.A. Morris. Molecularly functionalized silicon substrates for orientation control of the microphase separation of PS-*b*-PMMA and PS-*b*-PDMS block copolymer systems. *Langmuir*, 29(9):2809–2820, 2013.

[288] Hampton Research. Optimize, certificate of analysis, titration table for 0.5 M MES with 1.0 M sodium hydroxide, . URL http://hamptonresearch.com/documents/product/0000000132-0000000269.pdf.

[289] Hampton Research. Optimize, certificate of analysis, titration table for 1.0 M Tris HCl with 1.0 M sodium hydroxide, . URL https://hamptonresearch.com/documents/product/0000000137-0000000284.pdf.

[290] MESA$^+$ Institute for Nanotechnology. Equipment database: Analysis PHI Quantera SXM-XPS system. URL http://mesaplusnanolab.ewi.utwente.nl//mis/mishomepage.php.

Aknowledgements

Nu dat dit master scriptie onderzoek ten einde is, wordt het tijd om wat mensen te bedanken. Allereerst wil ik prof. Han Gardeniers en Roald Tiggelaar bedanken. Via Han heb ik deze opdracht gekregen, waarbij Roald mijn dagelijkse begeleider werd. Roald, heel erg bedankt voor je geduld en je hulp met het corrigeren van mijn scriptie.

Ook wil ik graag mijn medekantoorbewoners, Hoon Suk Rho, Mattia Morassutto, en Peter van der Linde. Peter kende ik al van de opleiding, en ik zal onze koffiemomentjes missen. Hoon, I will never forget your dedication to PDMS and how you wanted that I would work with PDMS as well. I also will never forget your other dedication: Molly Malone. It was really fun going there with you all! Mattia, I am still hearing you cursing in Italian from behind your computer screen: Vaffanculo!! Cazzo!! And of course I woul like to thank all the people of MCS for the great time! I hope to see you all soon again!!

People from out of MCS which I would like to thank are Yoonsun Yang and Daniël Hagedoorn. Yoon, thank you that I could use the Qubit fluorometer of the MCBP group!! Daniël, bedankt voor je hulp bij de contacthoekmetingen die ik bij de PCF groep kon doen! Verder wil ik graag de hele clean room staff bedanken voor hun trainingen en hulp tijden mijn fabricage proces.

Als laatste wil ik graag mijn ouders, broertje, en mijn vriendin Linda bedanken voor hun steun en geduld! Het lijkt mij maar moeilijk om met zo'n rare nanotechnoloog opgescheept te zitten.

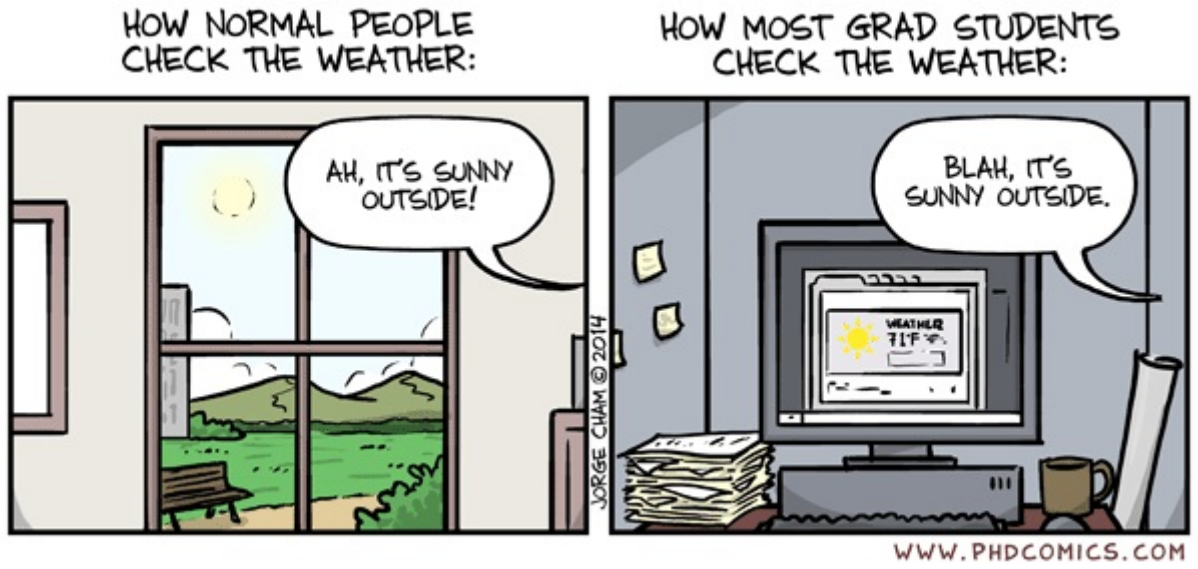

Figure 6.3: My experience the last weeks of my Master's thesis research. Picture taken from reference 250.

Appendix A

Microfabrication steps

The idea of the μSPE chip is already explained in chapter 1. In order to fabricate such a chip, some different fabrication steps are performed. These steps, in order of execution on a silicon $<100>$ DSP wafer, are standard cleaning, wet oxidation, front side photolithography, deep reactive ion etching (BOSCH process), cleaning, backside photolithography, BOSCH process on the backside of the wafer for the holes, and cleaning. Then, a glass borofloat wafer is cleaned and anodic bonded on the silicon wafer, followed by dicing the wafer into separate chips. The final step is the channel functionalization with chitosan or 3-aminopropylsilane. In the now following paragraphs, some attention is paid to the most important fabrication steps, *i.e.* wet oxidation, photolithography, deep reactive ion etching (BOSCH process), anodic bonding, channel functionalization, and the coupling of the micro world to the macro world. The cleaning steps are not further discussed here. The whole process flow can be found in appendix C.

A.1 Thermal oxidation

Thermal oxidation of silicon gives silicon dioxide. This material is amorphous and not the same as crystalline quarts (SiO_4) because bonds are not perfectly formed at the silicon/oxide interface, leaving atoms unbound and charged[251]. The structure of the silicon/oxide interface is shown in figure A.1.

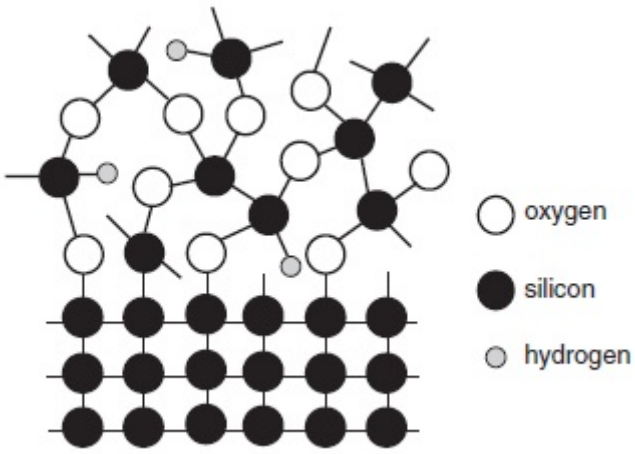

Figure A.1: The crystalline silicon and amorphous oxide interface. Dangling bonds are visible on atoms that do not have their full valence and some have hydrogen atoms bonded to them. Picture taken from reference 251.

There are two basic methods for the thermal oxidation of Si: wet and dry oxidation. The wet thermal oxidation has water gas and dry oxidation oxygen gas present in the oxidation furnace. The representative chemical reactions are shown in reaction 1 and 2, respectively.

$$Si(s) + 2\,H_2O(g) \longrightarrow SiO_2(s) + 2\,H_2(g)$$

$$Si(s) + O_2(g) \longrightarrow SiO_2(s)$$

Dry oxidation is normally performed in the temperature range of 800-950℃ and is often used for the growth of thin oxides (1-20 nm). The growth of oxide in a dry oxidation process is rather slow, when

compared to wet oxidation. This makes it very suitable for the growth of thin oxides for flash-memory tunnel oxides[252] and DRAM capacitors[253]. Wet oxidation on the other hand is used for the growth of thick oxides (100-1,000 nm). These thick oxides are grown at temperatures in the range 950-1100℃ and are used as diffusion[254] and etch masks[1], and as electrical isolation layers[255].

The growth of oxide is not a linear process. A model for the growth has been developed by Deal and Grove[256], hence the name Deal-Grove Oxidation Model. This models the growth by the classical Fick diffusion equation and chemical rate equation. However, the model does not assume anything about atomistic mechanisms of oxidation[251]. The derivation of this model is not given here because this goes beyond the scope of this report, but it can be found in reference 256. The result of this model is the following equation for oxide thickness:

$$\frac{x_0}{\frac{A}{2}} = \sqrt{1 + \frac{t+\tau}{\frac{A^2}{4B}}} - 1 \tag{A.1}$$

For wet oxidation the limits are $t \gg \frac{A^2}{4B}$ and $t \gg \tau$, making:

$$\frac{x_0}{\frac{A}{2}} \cong \sqrt{\frac{t}{\frac{A^2}{4B}}} \qquad \text{or} \qquad x_0 \cong \sqrt{Bt} \tag{A.2}$$

For dry oxidation the limits is $t \ll \frac{A^2}{4B}$, making:

$$\frac{x_0}{\frac{A}{2}} = \frac{1}{2}\left(\frac{t+\tau}{\frac{A^2}{4B}}\right) \qquad \text{or} \qquad x_0 \cong \frac{B}{A}(t+\tau) \tag{A.3}$$

The term $\frac{B}{A}$ is thus referred to as the linear rate constant and B is the parabolic rate constant, x_0 is the oxide thickness, t is the oxidation time, τ is the time correction for the already present (native) oxide. These results show that a parabolic decrease in oxidation rate is obtained when thick oxides are grown. This sets the maximum practical oxidation thickness on one to two micrometres. The results show also that the oxidation rate is linear for thin oxides. This is visible when the thicknesses of wet and dry etching are plotted. Graphs for wet and dry oxidation are shown in figure A.2[251]. The Deal-Grove model predicts initially a linear oxidation maximum practical thickness of the oxide is one to two micrometres because the oxidation rate decreases parabolic.

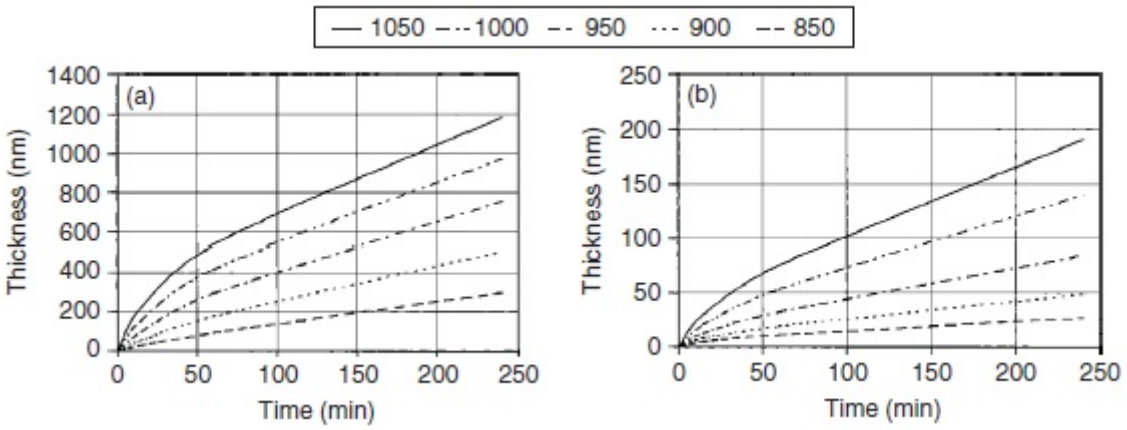

Figure A.2: A) Wet and B) dry oxidation of a $<100>$ Si wafer at temperatures ranging from 850 to 1050℃. Picture taken from reference 251.

In figure A.2 it is clearly visible that wet thermal oxidation has a much higher oxidation rate, even though the diffusion of oxygen molecules is quite faster than the diffusion of water molecules through the formed silicon dioxide. The reason for this is that the water solubility of silicon dioxide is four orders of magnitude larger than the oxygen solubility. Therefore, there is a higher concentration of water in silicon dioxide[251].

Although that the Deal-Grove model is a nice approximation, Watanabe and Ohdomari have developed a new kinetic equation for the thermal oxidation of silicon to replace the Deal-Grove model. Especially the linear initial part was not covered with satisfaction and is due to the very thin (native) oxide present at zero oxidation time[251]. This makes the initial stages of oxidation poorly understood. More information about this model can be found in their paper[257].

One other important property of oxidation is that it consumes silicon. The oxide is not only grown on top of the silicon, but also grown into the silicon. About 46% of the oxide layer is grown into the silicon, as can be seen in the following equation:

$$\frac{T_{Si}}{T_{SiO_2}} = \frac{V_{M,Si}}{V_{M,SiO_2}} = \frac{\frac{MW_{Si}}{\rho_{Si}}}{\frac{MW_{SiO_2}}{\rho_{SiO_2}}} = \frac{\frac{28.9[\text{g mol}^{-1}]}{2.33[\text{g cm}^{-3}]}}{\frac{60.08[\text{g mol}^{-1}]}{2.21[\text{g cm}^{-3}]}} \approx 0.46 \tag{A.4}$$

This growing mechanism is shown in figure A.3.

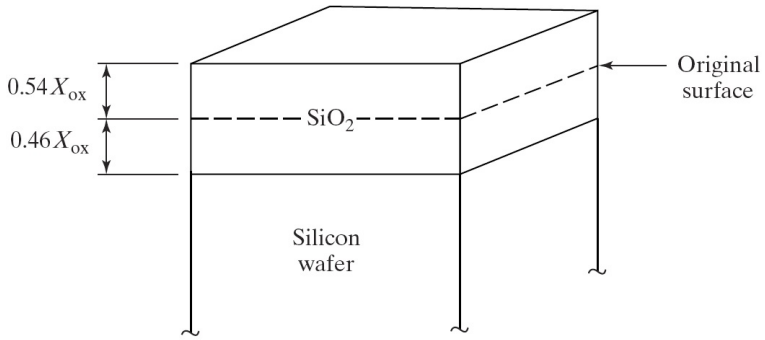

Figure A.3: Schematics of oxide growth, showing the consumption of silicon. X_{ox} is the final oxide thickness. Picture taken from reference 258.

The oxidation rate is dependent on the crystal orientation of the silicon. The $<100>$ orientation oxidizes slightly lower than the $<111>$ orientation. All the other orientations fall between these two[251,258].

A.2 Photolithography

Photolithography (also known as UV lithography or optical lithography) consists of several steps, which are performed in order to make a mask for the etching step. With the following sections, the whole photolithography process flow for direct contact/proximity lithography is discussed step by step as the wafer sees it. For every step a short explanation is given and some important elements are pointed out. Stepper lithography is not discussed, since this falls beyond the scope of this thesis.

A.2.1 Bake and prime

These two steps are the surface preparation steps of the photolithography process[259]. They initialize the surface and make the photolithography process independent from preceding process steps. The baking step is performed at 100-200℃ in order to remove adsorbed water. In the priming step, an adhesive promoter is applied on the surface by spin coating. Hexamethyl disilazane (HMDS, structural formula: $(H_3C)_3-Si-NH-Si-(CH_3)_3$) is often used as adhesive promoter. The hydroxyl groups of the wafer surface will form a bond with the silicon atom in HMDS, releasing ammonia. This process makes the surface hydrophobic and is shown in figure A.4. This hydrophobicity prevents water readsorption and ensures good wetting by the photoresist.

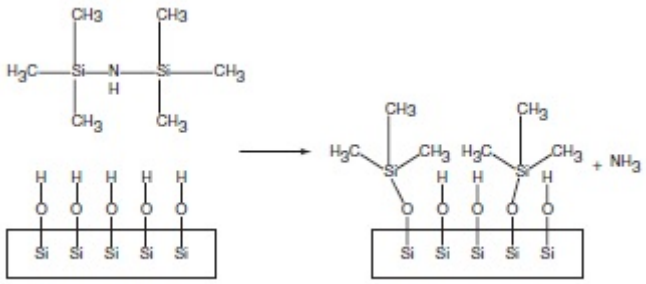

Figure A.4: Adhesion promotion by priming with HMDS. Figure taken from reference 259.

A.2.2 Photoresist spinning

In this step, a layer of photoresist is applied via spin coating. This is the standard resist application method. The resist is spread out over the wafer by accelerating the wafer to about 4,000 rpm. This leaves a very uniform layer of photoresist. The thickness of this layer (t) scales as follow with resist viscosity (η) and spin speed (ω):

$$t \propto \sqrt{\frac{\eta}{\omega}} \tag{A.5}$$

This process is shown in figure A.5.

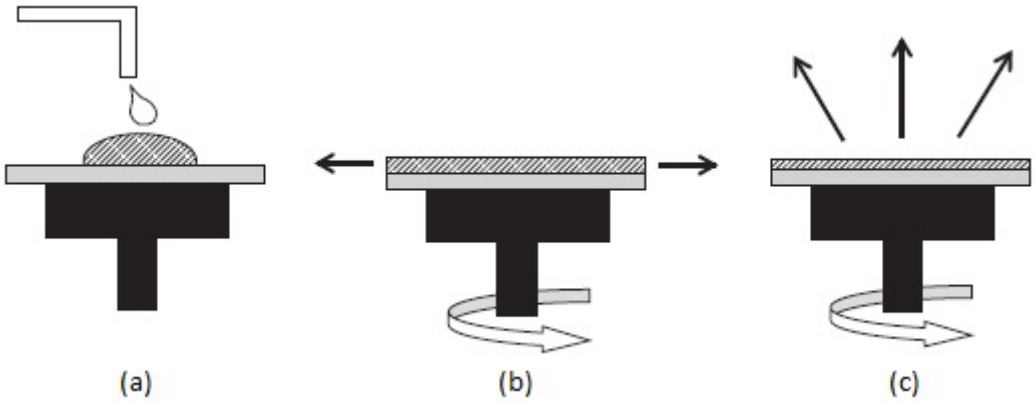

Figure A.5: Photoresist spin coating process, with (A) photoresist dispensing (a few millilitres), (B) acceleration (resist is expelled), and (C) final spinning at 4,000 rpm (partial drying via evaporation). Picture taken and modified from reference[259].

A.2.3 Pre-exposure bake

After spin coating the wafer with photoresist, the photoresist layer still consists solvent. This solvent is removed via a pre-exposure bake (also known as soft-bake). The temperature must not be too high because this will decompose the photoactive compound, leaving to lower sensitivity upon exposure.

A.2.4 Alignment and exposure

The next step in the photolithography process is inserting the wafer with photoresist and photomask into a mask aligner (schematics of an aligner are shown in figure A.6). The photomask is a glass plate with a pattern made of chromium on top of it. After aligning, the mask with photoresist and the photomask on top of it are exposed to an UV light source, which is often a mercury lamp. The chromium patterns of the photomask block the incoming light. The light that is not blocked, passes through the photomask and forms the pattern in the photoresist. The exposure time is often in the order of a few seconds, but can also be around 30 seconds[259]. The longer exposure times are used for thick photoresist layers. The pattern of the photomask is 1:1 transferred to the photoresist in case of vacuum contact lithography or proximity lithography. The difference between these two is shown in figure A.6).

A.2.5 Post-exposure bake

This baking step is performed after the exposure and leads to the diffusion of photogenerated molecules, which are responsible for a change in resist solubility in the developer. This diffusion also makes the artefacts made by optical interference effects smoother. Sometimes, the post-exposure bake is required to complete the photopolymerization process. This is especially the case with chemically amplified resists. Here, the catalyst, which is created by the UV light, reacts during this baking step and produces the difference in solubility between exposed and unexposed areas[259].

A.2.6 Development and hard bake

In the development step, the soluble parts of the photoresist are dissolved in a developer solution. The exposed parts in positive resist turn into carboxylic acids. This can be developed in an alkaline developer. An often used developer for positive photoresist is 0.26 M tetramethyl ammonium hydroxide

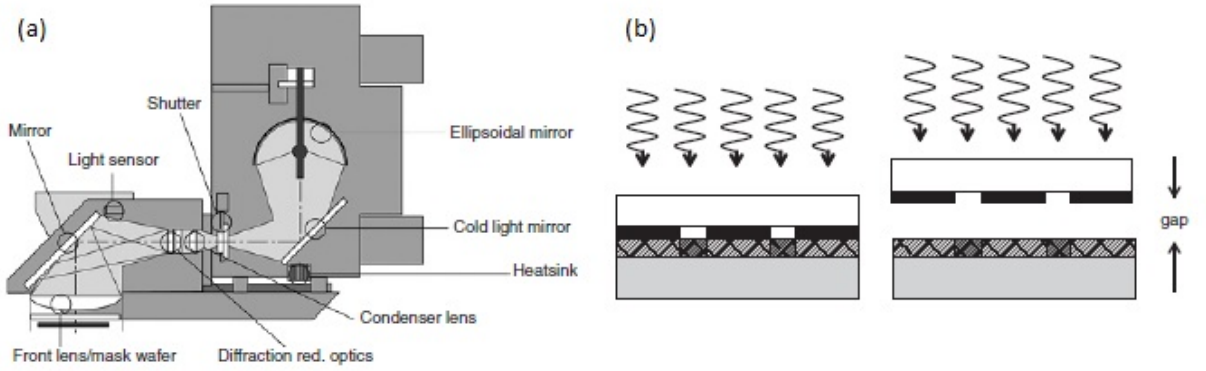

Figure A.6: Photolithography: (A) The lamp-mirror-shutter-filter-lens system of a traditional mask aligner, (B) difference between vacuum contact lithography (left) and proximity lithography (right). Figures taken from reference 259.

(TMAH)[259]. In negative resist it is the other way around. Here the exposed parts are cross-linked and rendered stable. The unexposed parts are dissolved in a solvent developer[259]. Rinsing and drying complete the development process. After the development, a hard bake is performed. This hardens the photoresist and is very useful in subsequent steps which are energetic, such as plasma etching or ion implementation, or wet processes, like wet etching or electroplating, because it improves the adhesion of the photoresist[259]. The temperature of this baking step is limited by the glass transition temperature. Above this temperature, the resist starts flowing. This creates shallow sloped walls instead of (nearly) straight vertical walls[259].

A.3 Deep reactive ion etching (BOSCH process)

The BOSCH process is a particular kind of deep reactive ion etching (DRIE), named after the company which developed and patented it[260]. It is an improved version of the reactive ion etching (RIE) process. Properties of DRIE and the BOSCH process are that it can etch with high etch rates, that it can fabricate structures with a relatively high aspect ratio (depth-to-width ratio), and that it have good side-wall profile control[251]. The etch rate for a DRIE process is often in the range 2-20 μm min^{-1}, which is one or two orders of magnitude higher than a RIE process (typically in the range 0.1-1 μm min^{-1})[251]. Because of the high etch rates, DRIE has become an standard step for through-wafer etching. Like RIE, the process starts with the application of a patterned photoresist layer. This layer protects the places on the wafer where etching is not desired. The etching step for DRIE consists of a cyclic process in which three processes are repeated until the desired etching depth is obtained[251,261]:

1. The first step is a plasma etching step. The etch gas is SF_6 and pulsed into the vacuum chamber. When brought into the plasma phase, this gas gives SF_5^+ ions. These ions etch not completely anisotropic, their etch effect is a little bit isotropic. The etching rate is amplified in one direction by applying an electrical field on the SF_6 plasma. The SF_6 gas is chosen for Si etching because it can achieve an etch rate that is one order of magnitude higher than for example Cl_2 and HBr, which also etch Si.

2. For the second step the gas is switched to C_4F_8 and pulsed into the vacuum chamber. This gas forms a Teflon-like n[CF_2] passivation layer all over the surface of the wafer and protects the side-walls against the isotropic etching of the SF_6 plasma, causing far less underetching. This causes an increase in anisotropy, and thus it promotes the fabrication of high aspect ratio structures. But it slows down the etching process and there is a chance of overpassivation. Overpassivation leads to residues and in the extreme case to nanograss due to micromasking (also known as black silicon).

After the second step, the process starts over, making it a cycle of two pulsed steps. The sidewalls of the final structure are undulating because of the pulsed operation, as can be seen in figure A.7.

Sensitivity of the etching plasma is dependent on the RF power of the plasma generator. A higher RF power results in an increased etch rate, but also in a lower selectivity. A lower pressure will give better directionality in the ion bombardment because of the fewer ion collisions during the flight of the ions, but higher gas flow rates are needed, making high pumping capacity mandatory. The temperature has to be low, since the photoresist will degrade when the temperatures approach and exceed the 100 ℃[251]. This all makes that a balance needs to be found in order to make high aspect ratio structures. If a

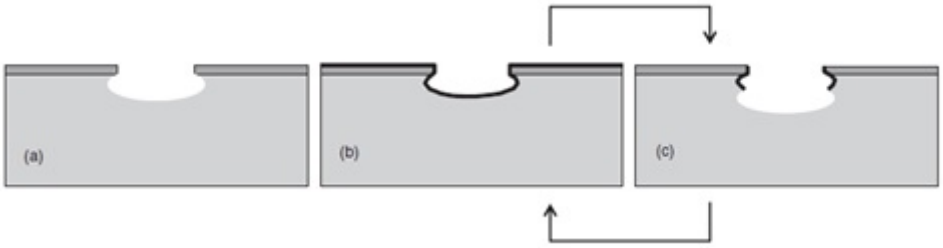

Figure A.7: Schematic representation of a basic two step Bosch process, which starts with (A) an etching step and is followed by (B) an passivation step. Picture taken and modified from 251.

good balance is found, aspect ratio's as high as 40[261], or more recently even 97[262] can be achieved with the BOSCH process. The complex interdependence of some general DRIE parameters and etch responses on the wafer is shown in figure A.8.

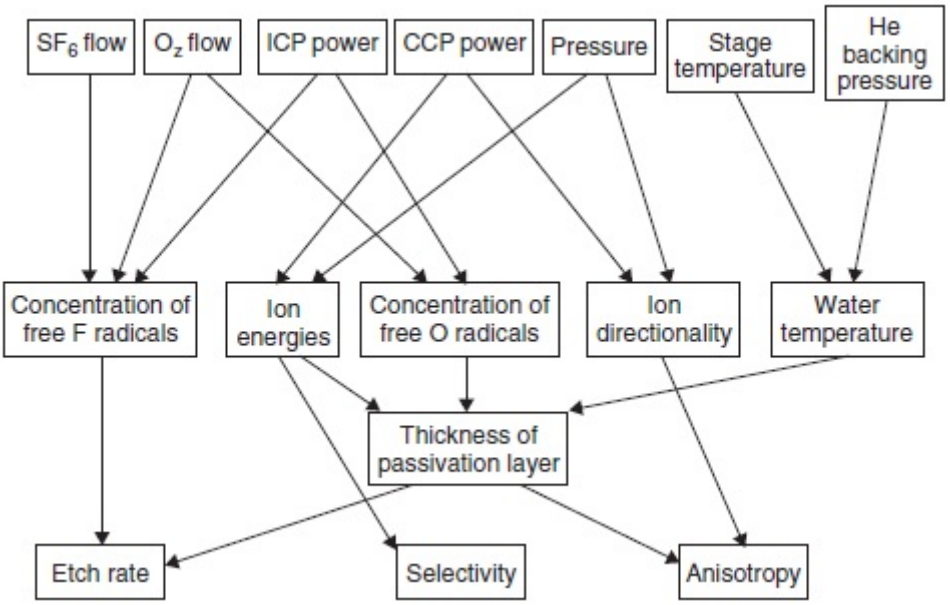

Figure A.8: The complex interdependence of some general DRIE parameters and etch responses on the wafer. Picture taken from reference 251.

A.4 Anodic bonding

Anodic bonding is also known as field-assisted thermal bonding (FATB) and is a direct bonding technique to mate two complete wafers, a silicon and glass wafer, and is used to hermetically seal and encapsulate the final structures in silicon[263–265]. The technique is the oldest bonding technique in microfabrication[263] and is based on bonding via elevated temperatures (usually in the range 200-500 °C[263,266]) and voltages (usually in the range 100-1,000 V[263,266]). Glass will conform at temperatures of 400-500 °C, which will seal structures and irregularities of up to 50-60 nm hermetically[263,265]. At a temperature of 400 °C, sodium oxide (NaO_2) will decompose into sodium and oxygen ions, $2\,Na^+$ and O_2^-, respectively[263]. The bonding process uses a voltage between 100-1,000 V, which is applied to the glass wafer[263,266]. The sodium ions become mobile at the elevated temperatures and start to migrate towards the glass top surface (cathode) because of the applied voltage. This leaves the relatively immobile oxygen ions behind at the glass-silicon interface[266]. This accumulation of oxygen ions will form a depletion layer (or space charge region). Then, an equivalent charge of opposite sign will form on the silicon side of the glass-silicon interface. This region is called the image charge[266]. Now, an electrostatic force will pull the glass and silicon wafer together[263] and the charged regions result in a high electric field across the glass-silicon interface[266]. This electric field has a magnitude up to 10^6 V cm^{-2}[267]. The oxygen ions are drifted away from the sodium depletion region to the glass-silicon interface[266]. Here, they will react with the silicon, leading to irreversible chemical SiO_2 bonds (oxidation)[266,268]:

$$Si + 2\,O^{2-} \longrightarrow SiO_2 + 4\,e^-$$

The sodium ions are neutralized at the cathode. The elevated temperatures will cause that more ionization will take place, but also that the diffusion of ions is faster, so the depletion width is greater, leading to stronger bonds[263]. The diffusion is mainly dependent on the applied voltage[266]. A small voltage causes that the drift velocity and kinetic energy of the oxygen ions cannot sustain a high oxidation rate at the bonding front. This leads to longer bonding times, or even non-bonded substrates. This charge (re)distribution process is shown in figure A.9 and the applied voltage-bonding time relation is shown in figure A.10. This makes the magnitudes of applied DC voltage and temperature, the bonding time, and surface characteristics the most deterministic parameters for the anodic bonding process[269].

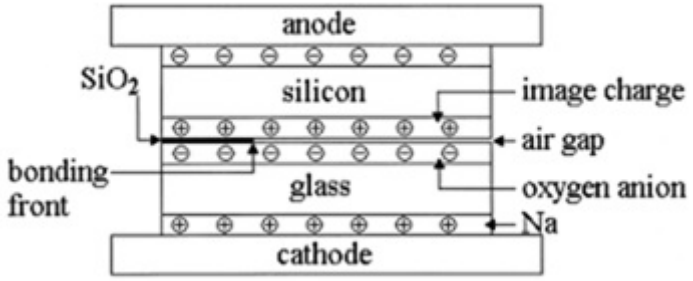

Figure A.9: Schematic representation of anodic silicon-glass bonding, illustrating the charge distribution during bonding. Picture taken from reference 266.

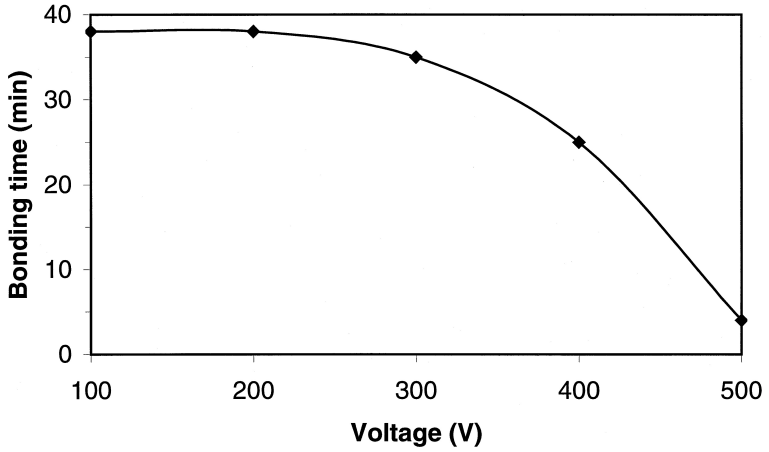

Figure A.10: Plot of bonding time versus applied voltage for a p-type silicon wafer and Corning 7740 glass wafer. Both substrates were pre-cleaned using acetone. Picture taken from reference 266.

The bonding mechanism can be initiated by simply applying some pressure at the centre of the wafer. This can be omitted when the bonding is performed in a vacuum[263]. The size of bondable area can be small. Silicon pillars of 10 μm diameter have been bonded to glass, as described by de Malsche *et al.*[228].

A.5 Channel functionalization

The functionalization of the channel and pillars is based on conventional silicon oxide surface chemistry via self-assembled monolayers (SAM). A SAM is only a couple of nanometres thick, but it can completely change the properties of a surface. The use of self-assembly is already known since 1946, when Zisman *et al.* used monolayers of long-chain hydrocarbons with polar head groups on polar surfaces[270]. Even though these layers were extremely thin (roughly 2 nm), they were able to change the surface properties completely. The first real application for SAMs came a little bit more than three decades later, when Polymeropoulos *et al.* used it for measuring electrical conduction between two metal surfaces[271]. The real revolution started when Sagiv published the results of his work on organosilane monolayers on SiO_2[131].

There are diverse methods available for the functionalization of the surface of a silicon wafer. For example, the passivated silicon can be derivatized via a hydrosilation reaction. Such SAM formation

can be done via, for example, metal complex catalysed hydrosilylation[272,273], or radical-induced hydrosilylation[274–276]. The hydrosilation method is an unsuitable method for silicon with a (native) oxide layer because this needs an hydrogen-terminated surface in order to attach a SAM via, for example, This hydrogen-terminated surface is created by etching away the (native) oxide in HF[277] and this makes it a unsuitable method for coating a silicon oxide surface. In order to attach a monolayer to a silicon oxide surface, silanization of the (native) silicon oxide layer via a liquid phase[138,278–280] or gas phase[281–283] can be performed. The gas phase silanization reactions can be performed via heating up the silane reagent[281], gas formation in a vacuum chamber[282], or vacuum distillation[283]. The main problems of the gas phase method is that it results in a layer with high variations in silane amounts and quality of the layer[284], that it takes up to several hours before the reaction is finished[284], and that it requires more advanced equipment.

The silanization process consists of two steps, *e.g.* the hydrolysis of the leaving groups (for example alkoxy groups) and the condensation of surface silanols with the silanols of the silane molecule[131,284] in an anti-Markovnikov fashion[274]. Studies have shown that these two steps occur when the silane molecules come in contact with the adsorbed water layer on the (native) silicon oxide surface[285,286]. A monolayer of water is promoting the coverage and quality of the SAM formation[131]. Vacuum fired samples show a saturation coverage for octadecyltrichlorosilane which is roughly three times smaller than the saturation coverage on a surface of hydrated silicon oxide[285]. More information about SAMs and organometallic surface chemistry on silicon can be found in the comprehensive reviews written by Onclin, Ravoo, and Reinhoudt *et al.*[**?**] and Buriak[273]. This water promoted functionalization makes a liquid phase functionalization favourable in this study. In order to increase the quality of the formed layer even further, the silicon oxide is activated with piranha solution (1:3 v/v 30% H_2O_2/96% H_2SO_4). This reagent removes any organic contamination and creates hydroxyl groups[287]. This is useful since native oxide has a low surface hydroxyl ($-$OH) group content[285].

Appendix B

Photolithography masks

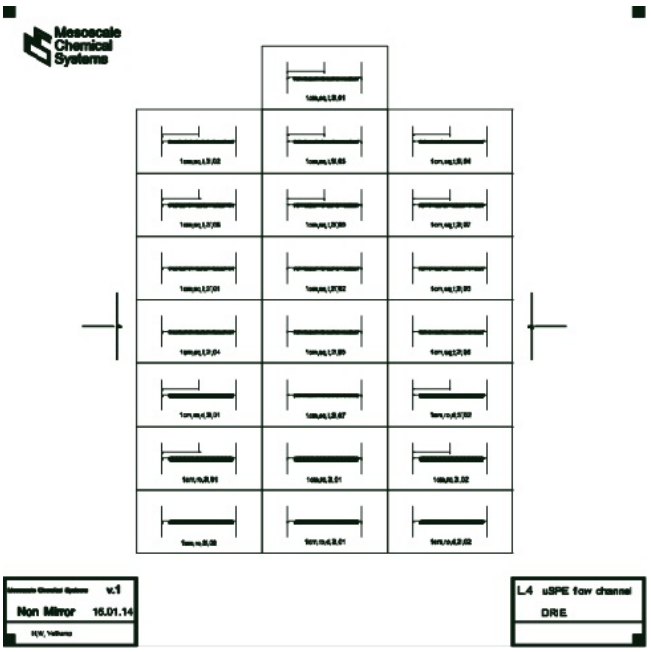

(a) Mask with channels for frontside lithography.

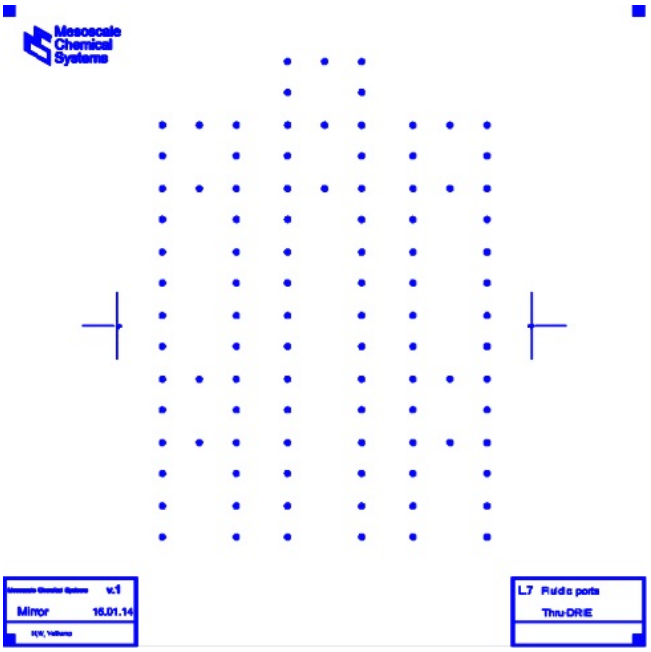

(b) Mask with via-holes for backside lithography.

Figure B.1: Photolithography masks used for the fabrication of the μSPE device.

Appendix C

Process flow

C.1 Frontside

Step	Process		Comment
1	**Substrate - Silicon** **Si <100> DSP**	NL-CLR-Wafer Storage Cupboard Orientation: <100> Diameter: 100 mm Thickness: 525 $\pm$ 25μm Polished: Double side Resistivity: 5-10Ωcm Type: p	Start with 10 wafers
2	**Clean HNO_3-1**	NL-CLR-WB14 beaker 1: HNO_3 (99%), 5min	
3	**Clean HNO_3-2**	NL-CLR-WB14 beaker 2: HNO_3 (99%), 5min	
4	**Quick Dump Rinse (QDR)**	NL-CLR-Wet benches Recipe 1 QDR: 2 cycles of steps 1 till 3: 1- fill bath 15 sec 2- spray dump 15 sec 3- spray-fill 40 sec 4- end fill 500 sec	
5	**Clean HNO3-3a/b**	NL-CR-WB14 beaker 3a/b: HNO_3 (69%) temp 95℃ time $>$ 10 min	
6	**Quick Dump Rinse (QDR)**	NL-CLR-Wet benches Recipe 1 QDR: 2 cycles of steps 1 till 3: 1- fill bath 15 sec 2- spray dump 15 sec 3- spray-fill 40 sec 4- end fill 500 sec	
7	**Etching in HF 1%** **(prefurnace)**	NL-CLR-WB15 use beaker HF 1%	Native oxide strip: $>$ 1 min or hydrofobic surface
8	**Quick Dump Rinse (QDR)**	NL-CLR-Wet benches Recipe 1 QDR: 2 cycles of steps 1 till 3: 1- fill bath 15 sec 2- spray dump 15 sec 3- spray-fill 40 sec 4- end fill 500 sec	
9	**Substrate drying**	NL-CLR-Wet benches Single wafer dryer Speed: 2500 rpm Time: 60 s with 30 s N_2 flow	Or use Semitool (#clean121) 1 - Quick dump rinse 2 - Load Semitool 3 - Press start

Step	Process		Comment
10	**Wet Oxidation of Silicon @ 1150℃**	NL-CLR- Furnace B2 Standby temperature: 800℃ Check water level of bubbler Check water temp.: 85℃ Program: WET1150B • Temp.: 1150℃ • Gas: H_2O + N_2 (1 L min^{-1}) • Ramp: 10℃ min^{-1} • Cooldown: 7.5℃ min^{-1}	1.2 μm ($\sim$5 hours) Time required: Process time + 2 hours Do it overnight
11	**Priming (liquid)**	NL-CLR-WB21/22 Primer: HexaMethylDiSilazane (HMDS) Use spincoater recipe: • 4000 (4000 rpm, 30 s)	
12	**Coating Olin OiR 906-12**	NL-CLR-WB21 Coating: Primus spinner • Olin OiR 906-12 • Program: 4000 (4000 rpm, 30 s) Prebake: hotplate • Time: 60 s • Temp.: 95℃	$\pm$ 1.2 μm thick
13	**Alignment & Exposure Olin OiR 906-12**	NL-CLR-EV620 Electronic Vision Group EV620 Mask Aligner • Hg-lamp: 12 mW cm^2 • Exposure time: 2.5 s	Manual top side, vacuum hard contact, 1 min delay exposure MASK1 – usPE flow channel
14	**Development Olin OiR resist**	NL-CLR-WB21 Post exposure bake: hotplate • Time: 60 s • Temp.: 120℃ development: developer OPD4262 • Time: 30 s in beaker 1 • Time: 15-30 s in beaker 2	
15	**Quick Dump Rinse (QDR)**	NL-CLR-Wet benches Recipe 1 QDR: 2 cycles of steps 1 till 3: 1- fill bath 15 sec 2- spray dump 15 sec 3- spray-fill 40 sec 4- end fill 500 sec	
16	**Substrate drying**	NL-CLR-Wet benches Single wafer dryer Speed: 2500 rpm Time: 60 s with 30 s N_2 flow	Or use Semitool (#clean121) 1 - Quick dump rinse 2 - Load Semitool 3 - Press start
17	**Inspection by optical microscope**	NL-CLR-Nikon Microscope dedicated microscope for lithography inspection	
18	**DRIE of SiO_2**	NL-CLR-Adixen AMS100 DE Application: $<$ 5 μm etch depth **Parameters** / **Values** C_4F_8 20 sccm He 150 sccm CH_4 15 sccm He-backside cooling 10 mbar ICP 2800 watt CCP 350 watt Pressure 8.5×10^{-3} mbar Electrode temp. -10℃ Substrate height 120 mm	30 minutes of cleaning after every 20 minutes of etching Etch rate SiO_2: 450$\sim$520 nm min^{-1} Etch time: 3$\sim$3.5 min Process time: etch time + 5 min Cooling down from 20℃ to -10℃ takes $\pm$ 30 min

Step	Process		Comment
19	**Chamber clean with O_2 plasma**	NL-CLR-Adixen AMS100 DE Chamber clean **Parameters** **values** Gas O_2 Flow 200 sccm APC 100 % ICP 2000 watt CCP 50 RF (SH gen 1) SH 150 mm Electrode temp. - He-backside cooling 10 mbar Wafer plain Si wafer Time 30 min Pressure after cleaning $< 6.5\times10^{-3}$ mbar	After every 20 minutes of etching Recipe: cleaningSTD
20	**Plasma etching of Si B-HARS recipe**	NL-CLR-Adixen AMS100 SE Recipe: B-HARS Standard **Parameters** **Etch** **Deposition** Gas SF_6 C_4F_8 Flow [sccm] 250 200 Time [s] 3 1 Priority 2 1 APC [%] 100 100 CCP LF [watt] 90 90 Pulsed LF [ms] 10/90 10/90 ICP [watt] 1500 1500 He [mbar] 10 10 SH [mm] 200 200 Electrode T [℃] 10 10	Desired depth: 25 μm Etch speed Si: $\pm$ 2.5 μm min^{-1} Etch speed Olin OiR: 25$\sim$50 nm min^{-1} Use dummy wafer for determining real etch rate
21	**Stripping of resist in O_2 plasma**	NL-CLR-Tepla300 Barrel Etcher (2.45 GHz) Ultra clean system only: • No metals except Al See list with recipes in Clean room • O_2 flow: 200 sccm (50%) • Power: up to 1000 W • Pressure: 1 mbar	Recipe 5 Time: 30 min

C.2 Backside

Step	Process		Comment
22	**Priming (liquid)**	NL-CLR-WB21/22 Primer: HexaMethylDiSilazane (HMDS) Use spincoater recipe: • 4000 (4000 rpm, 30 s)	
23	**Coating Olin OiR 908-35**	NL-CLR-WB21 Coating: Primus spinner • Olin OiR 908-35 • Program: 2000dyn (2000 rpm, 30 s) Prebake: hotplate • Time: 180 s • Temp.: 95℃	$\pm$ 5 μm thick
24	**Alignment & Exposure Olin OiR 908-35**	NL-CLR-EV620 Electronic Vision Group EV620 Mask Aligner • Hg-lamp: 12 mW cm^2 • Exposure time: 12 s	Manual back side, soft contact MASK2 – Fluidic ports

Step	Process		Comment
25	**Development Olin OiR resist**	NL-CLR-WB21 development: developer OPD4262 • Time: 45 s in beaker 1 • Time: 45 s in beaker 2	Post exposure bake not required because of thick resist
26	**Quick Dump Rinse (QDR)**	NL-CLR-Wet benches Recipe 1 QDR: 2 cycles of steps 1 till 3: 1- fill bath 15 sec 2- spray dump 15 sec 3- spray-fill 40 sec 4- end fill 500 sec	
27	**Substrate drying**	NL-CLR-Wet benches Single wafer dryer Speed: 2500 rpm Time: 60 s with 30 s N_2 flow	Or use Semitool (#clean121) 1 - Quick dump rinse 2 - Load Semitool 3 - Press start
28	**Postbake Olin OiR resist**	NL-CLR-WB21 Postbake: hotplate • Temp.: 120℃ • Time: 20 min	Not longer than 20 minutes! Otherwise cracks can appear in the resist!
29	**Inspection by optical microscope**	NL-CLR-Nikon Microscope dedicated microscope for lithography inspection	
30	**DRIE of SiO_2**	NL-CLR-Adixen AMS100 DE Application: < 5 μm etch depth **Parameters** **Values** C_4F_8 20 sccm He 150 sccm CH_4 15 sccm He-backside cooling 10 mbar ICP 2800 watt CCP 350 watt Pressure 8.5×10^{-3} mbar Electrode temp. -10℃ Substrate height 120 mm	30 minutes of cleaning after every 20 minutes of etching Etch rate SiO_2: 450∼520 nm min^{-1} Etch time: 3∼3.5 min Process time: etch time + 5 min Cooling down from 20℃ to -10℃ takes $\pm$ 30 min
31	**Chamber clean with O_2 plasma**	NL-CLR-Adixen AMS100 DE Chamber clean **Parameters** **values** Gas O_2 Flow 200 sccm APC 100 % ICP 2000 watt CCP 50 RF (SH gen 1) SH 150 mm Electrode temp. - He-backside cooling 10 mbar Wafer plain Si wafer Time 30 min Pressure after cleaning $< 6.5\times10^{-3}$ mbar	After every 20 minutes of etching Recipe: cleaningSTD

Step	Process			Comment
32	**DRIE of Si** **B-UNIFROM recipe**	NL-CLR-Adixen AMS100 SE Recipe: B-UNIFORM Standard Applicatoin: Uniform/high speed Si etching		Use DuPont MX5020 foil for protection against He leakage Etch rate Si: 18$\sim$22 μm min^{-1} Etch rate Olin OiR: $<$125 nm min^{-1}
		Parameters	**Etch** / **Deposition**	
		Gas	SF_6 / C_4F_8	
		Flow [sccm]	500 / 135	
		Time [s]	13 / 2	
		Priority	1 / 2	
		APC [%]	15 / 15	
		CCP LF [watt]	10 / 10	
		Pulsed LF [ms]	35on/65off / 35on/65off	
		ICP [watt]	2500 / 2500	
		He [mbar]	10 / 10	
		SH [mm]	110 / 110	
		Electrode T [℃]	10 / 10	
33	**Stripping of resist in O_2 plasma**	NL-CLR-Tepla300 Barrel Etcher (2.45 GHz) Ultra clean system only: • No metals except Al See list with recipes in Clean room • O_2 flow: 200 sccm (50%) • Power: up to 1000 W • Pressure: 1 mbar		Recipe 5 Time: 30 min
34	**Stripping resist in piranha private use**	NL-CLR-WB09 Application: stripping of resist Mixture: H_2SO_4:H_2O_2 (3:1) vol% • Add H_2O_2 slowly! to H_2SO_4 exothermic process! • Due to mixing the temperature will increase to $\pm$130℃ • Adjust the hotplate at 85℃ • Time: depends on application (10-30 min)		Stripping of resist and DuPont MX5020 foil
35	**Quick Dump Rinse (QDR)**	NL-CLR-Wet benches Recipe 1 QDR: 2 cycles of steps 1 till 3: 1- fill bath 15 sec 2- spray dump 15 sec 3- spray-fill 40 sec 4- end fill 500 sec		
36	**Substrate drying**	NL-CLR-Wet benches Single wafer dryer Speed: 2500 rpm Time: 60 s with 30 s N_2 flow		Or use Semitool (#clean121) 1 - Quick dump rinse 2 - Load Semitool 3 - Press start
37	**Etching in HF 50%**	NL-CLR-WB09/10 Use private beaker for etching: HF (xx%) Add HF (50%) to DI water for diluted etch solutions Temp.: 20℃		Time: 3 min or untill hydrophobic surface Etch rate: $\pm$ 1 μm min^{-1}
38	**Quick Dump Rinse (QDR)**	NL-CLR-Wet benches Recipe 1 QDR: 2 cycles of steps 1 till 3: 1- fill bath 15 sec 2- spray dump 15 sec 3- spray-fill 40 sec 4- end fill 500 sec		
39	**Substrate drying**	NL-CLR-Wet benches Single wafer dryer Speed: 2500 rpm Time: 60 s with 30 s N_2 flow		Or use Semitool (#clean121) 1 - Quick dump rinse 2 - Load Semitool 3 - Press start

C.3 Top wafer

Step	Process		Comment
40	**Substrate - Borofloat BF33-500 μm**	NL-CLR-Wafer Storage Cupboard • Supplier: Schott • Type: Borofloat 33 • C.T.E.: 3.25×10^{-6} K^{-1} • T_{glass}: 525℃ • T_{anneal}: 560℃ • $T_{softening}$: 820℃ • Diameter: 100.0 mm $\pm$ 0.3 mm • Thickness: 0.5 mm $\pm$ 0.025 mm • Roughness: $<$ 1.0 nm • TTV: $<$ 5 μm • Surface: DSP • Edge: C-edge • Flat: 32.5 mm (Semi) • Sec. Flat: 18 mm (acc to SEMI) Etch rates: HF 25%: 1 μm min^{-1} BHF (1:7): 20$\sim$25 nm min^{-1} HF 1%: 8.6 nm min^{-1}	Start with 10 wafers For glass cover of chip
41	**Clean HNO3 1&2**	NL-CLR-WB16 • Beaker 1: HNO_3 (99%), 5 min • Beaker 2: HNO_3 (99%), 5 min	Clean together with processed Si wafers: promotes oxidation of the surface
42	**Quick Dump Rinse (QDR)**	NL-CLR-Wet benches Recipe 1 QDR: 2 cycles of steps 1 till 3: 1- fill bath 15 sec 2- spray dump 15 sec 3- spray-fill 40 sec 4- end fill 500 sec	
43	**Substrate drying**	NL-CLR-Wet benches Single wafer dryer Speed: 2500 rpm Time: 60 s with 30 s N_2 flow	Or use Semitool (#clean121) 1 - Quick dump rinse 2 - Load Semitool 3 - Press start

C.4 Bonding and dicing

Step	Process		Comment
44	**Manually aligning and prebonding**	NL-CLR-WB16 Method: • Contact wafers manually • Apply light pressure with tweezers • If necessary use tweezers to press out air bubbles • Check prebonding by using IR-setup	Wafers must be completely dry: use N_2 gun to dry Place single wafer box slightly tilted and use as bonding holder

Step	Process		Comment
45	**EV501 Anodic bonding**	NL-CLR-EV501 bond tool Settings: • Temp.: 400℃ • Vacuum: $< 10^{-1}$ mbar • High voltage: 1000 Volt • Pressure: 300 N • Total process time: 2 h • Load first Si wafer • Load then glass wafer • If necessary, alignment can be done with EV620 mask aligner	
46	**UV dicing foil (Adwill D-210)**	NL-CLR- Dicing foil Information: • Thickness: 125 μm • Material: 100 μm PET + 25um acrylic (adhesive) • Adhesion before UV: 2000 mN/25mm • Adhesion after UV: 15 mN/25mm UV irradiation: • Luminance: $>$ 120 mW cm^{-2} • Quality: $>$ 70 mJ cm^{-2} • Wavelength: 365 nm	Apply on Si side: blocks via-holes for dirt
47	**Dicing of a Si-glass wafer stack**	NL-CLR-Disco DAD dicing saw Parameters dicing: • Wafer work size: 110 mm for a standard 100 mm Si wafer • Max. feed speed: 10 mm s^{-2} • X and Y values: correspond respectively to Ch1 and Ch2 and those values are determined by mask layout • Saw type: TC-300	Set blade height: 50 μm Pitch: X: 10.3 mm Y: 20.3 mm
48	**UV flood exposure UV dicing foil**	NL-CLR-Spectronics Corporation Spectrolinker XL-1500 UV Crosslinker • UV cross linking (200-450 nm) • Dose: 100 mJ cm^{-2} • Time: 1200$\times$100 μJ cm^{-2}	Choose Optimal crosslink Press start

Appendix D

Protocols

D.1 Chelex DNA isolation

1. Rinse your mouth for 10 s with 0.9% NaCl.
2. Spit the mouthwash into a plastic cup.
3. Transfer the mouthwash into a centrifuge tube and close the lid.
4. Centrifuge for 10 minutes at 500$\sim$1,000 g.
5. Transfer the supernatant into the plastic cup, while keeping the cell pellet intact.
6. Put the tube with the cell pellet on ice.
7. Add 500 μL 10% Chelex solution to the cell pellet (mix the Chelex suspension a couple of times in order to get a homogeneous solution before adding it to the cell pellet).
8. Resuspend the cells in the Chelex solution by pipetting it a couple of times.
9. Pipet 500 μL of the resuspended solution into a 1.5 mL Eppendorf cup and close the lid.
10. Puncture the lid of the Eppendorf cup.
11. Heat the cup for 10 minutes at 100℃.
12. Cool the cup for 1 minute on ice.
13. Centrifuge the cup for 30 s on maximal rpm in order to filtrate the Chelex grains.
14. Pipet 200 μL of the supernatant (leave the Chelex pellet behind) into a new 1.5 mL Eppendorf cup en freeze it.

D.2 Buffer preparation

The buffers are prepared according to tables of Hampton Research. The buffers are made according following protocols:

MES buffer of pH 5.0[288]:

1. Add 510 μL 1.0 M NaOH solution in 100 mL glassware.
2. Add 20 mL 0.5 M MES solution to it.
3. Fill it to 100 mL with DI water.

TRIS buffer of pH 9.2[289]:

1. Add 9.2 mL 1.0 M NaOH solution in 100 mL glassware.
2. Add 10 mL 1.0 M TRIS solution to it.
3. Fill it to 100 mL with DI water.

The TRIS buffer of pH 12.6[289]:

1. Add 18.54 mL 1.0 M NaOH solution in 100 mL glassware.
2. Add 10 mL 1.0 M TRIS solution to it.
3. Fill it to 100 mL with DI water.

The result of the first two buffers is tested with universal pH indicator paper and with a Mettler Toledo SevenMulti with an InLab Expert PRO pH probe (Greifensee, Switzerland). These results are shown in figure D.1 and table D.1.

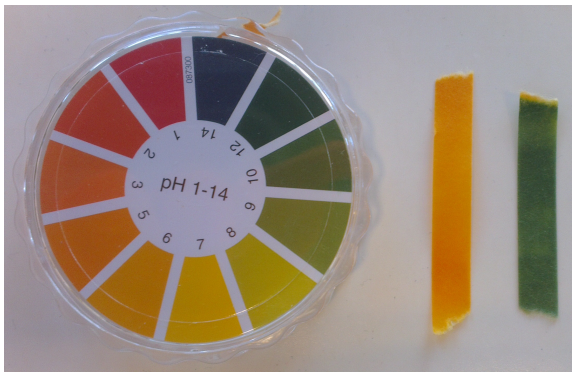

Figure D.1: pH analysis with universal pH indicator paper.

Table D.1: Results of pH measurements with the Mettler Toledo SevenMulti with an InLab Expert PRO pH probe.

Buffer	**Measured pH**
MES	5.01 $\pm$ 0.02 (n=3)
TRIS buffer 1	9.23 $\pm$ 0.08 (n=3)
TRIS buffer 2	12.61 $\pm$ 0.02 (n=3)

D.3 Qubit dsDNA HS assay

1. Prepare working solution
    - 200 µL is required for each sample and standard
    - Dilute the reagent 1:200 in buffer, use a disposable plastic container
2. Make standards
    - Add 10 µL of standard and 190 µL of working solution in a 500 µL PCR tube
    - Vortex 2-3 s
    - Incubate for 2 min at R.T.
3. Prepare samples
    - Add 1 µL of sample and 199 µL of working solution in a 500 µL PCR tube

- Vortex 2-3 s
- Incubate for 2 min at R.T.

4. Measurement
   - Turn on the Qubit fluorometer and press any button
   - Select assay to be performed
   - Calibrate

     Load first standard and press go

     Load second standard and press go
   - Read samples

     Load sample tube 1 and press go

     Continue

     Calculate starting concentration, using "calculate sample concentration" or manually calculate based on dilution in working solution
5. Discard all tubes

Appendix E

Computational fluid dynamics results

The simulations are done with the creeping flow physics package of COMSOL Multiphysics 4.3b (Burlington, MA, United States). As model liquid, water at room temperature is taken. No-slip boundary conditions are assumed because of the microfluidics regime. The column is 300 μm wide and the pillars are either 10 $\times$ 10 μm^2 or 10 μm in diameter. All values of the scale bar are in mm s^{-1}.

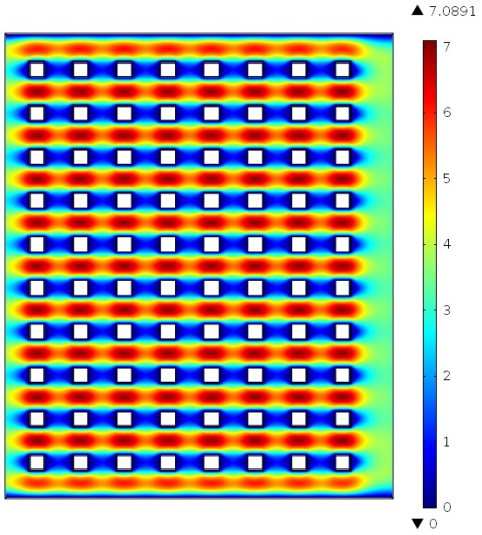

Figure E.1: Velocity profile in a column with square pillars with the flat directed to the flow and placed in a line grid.

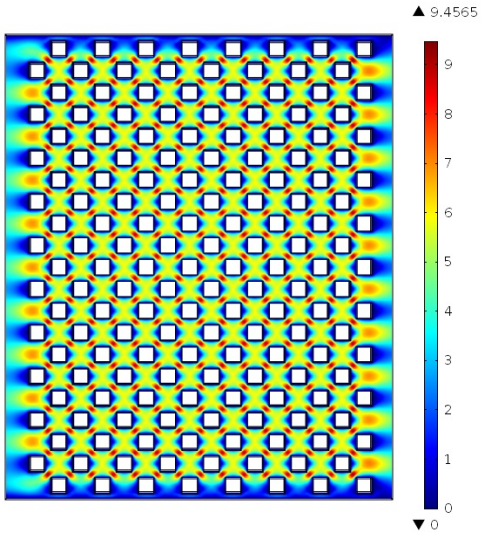

Figure E.2: Velocity profile in a column with square pillars with the flat directed to the flow and placed in a hexagonal grid.

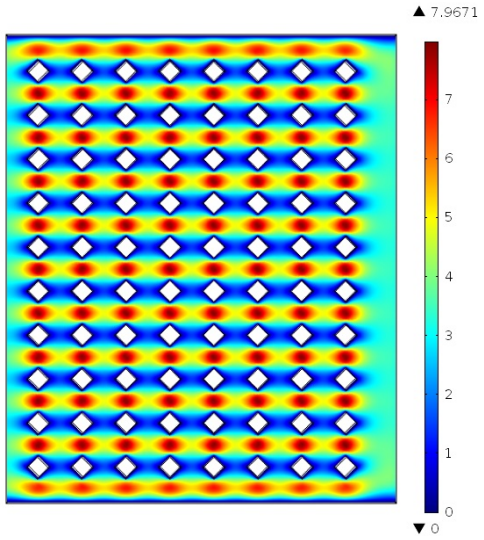

Figure E.3: Velocity profile in a column with square pillars with the corner directed to the flow and placed in a line grid.

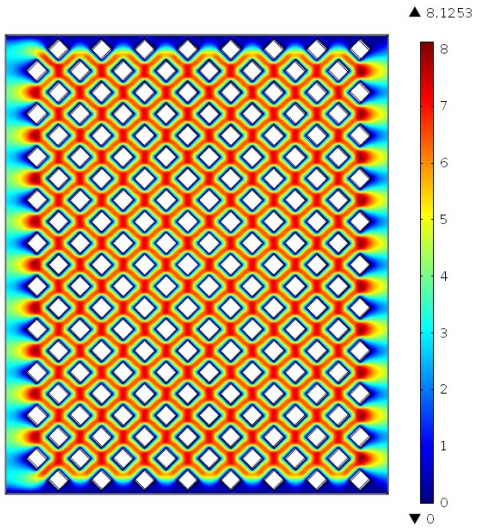

Figure E.4: Velocity profile in a column with square pillars with the corner directed to the flow and placed out of phase.

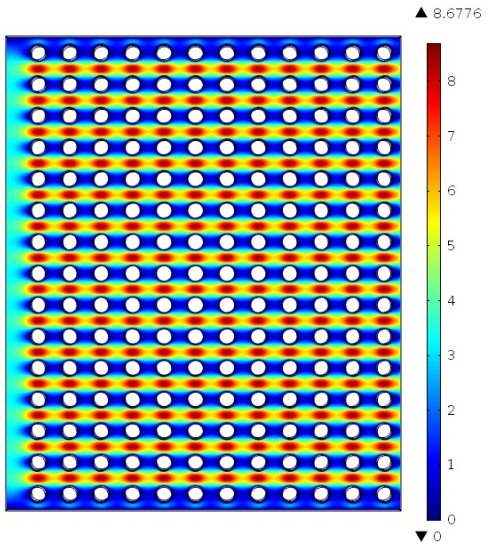

Figure E.5: Velocity profile in a column with round pillars that are placed in a line grid.

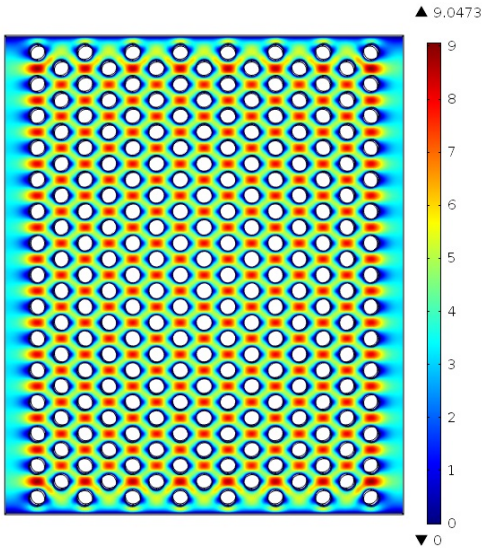

Figure E.6: Velocity profile in a column with round pillars that are placed in a hexagonal grid.

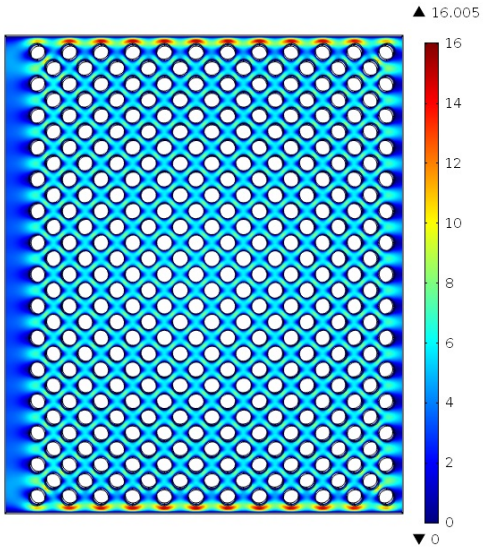

Figure E.7: Velocity profile in a column with denser packed round pillars that are placed in a hexagonal grid.

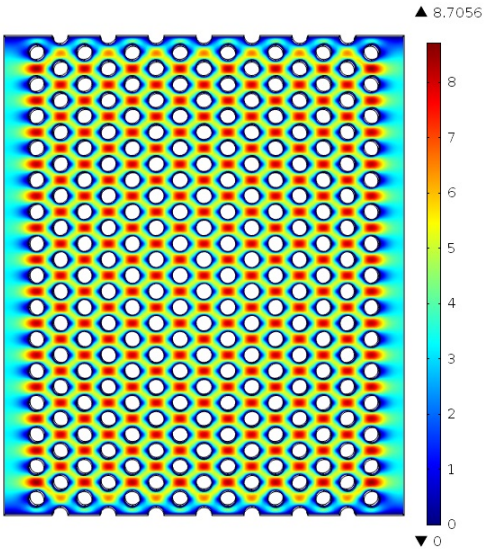

Figure E.8: Velocity profile in a column with sidewall structures and round pillars that are placed in a hexagonal grid.

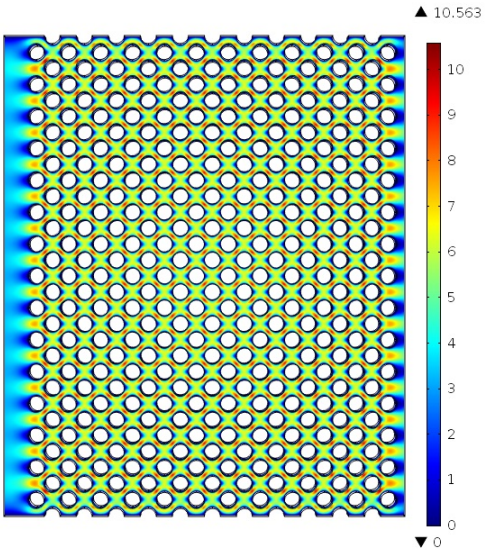

Figure E.9: Velocity profile in a column with sidewall structures and denser packed round pillars that are placed in a hexagonal grid.

Appendix F

Microscope images of the photolithography mask “μSPE flow channel”

Images are made with normal optical microscopy.

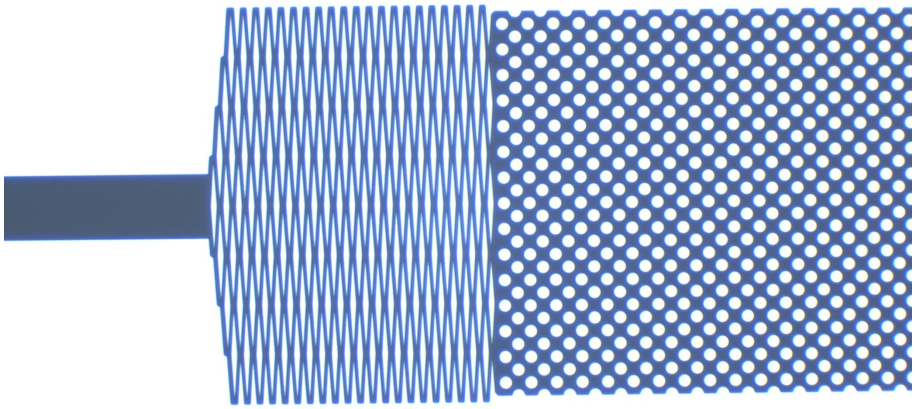

(a) Inlet of the column.

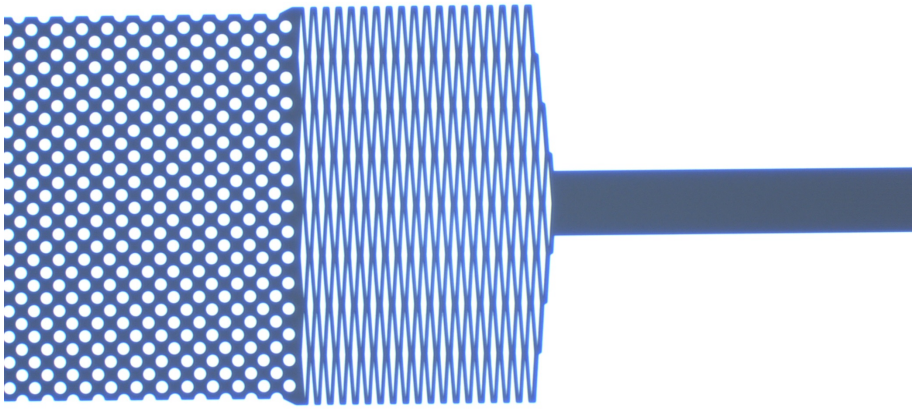

(b) Outlet of the column.

Figure F.1: Microscope images of the mask for the chip with a column with densely packed round pillars.

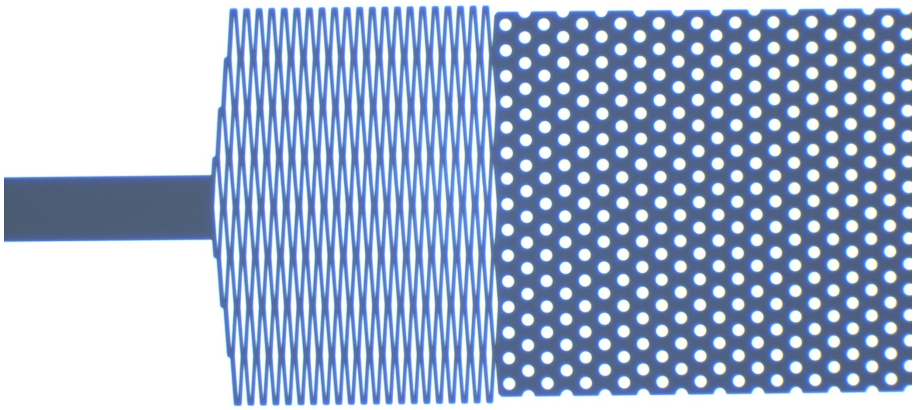

(a) Inlet of the column.

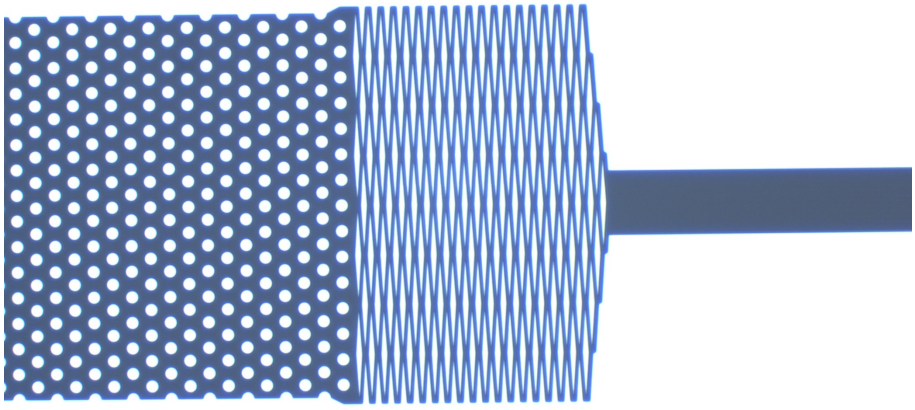

(b) Outlet of the column.

Figure F.2: Microscope images of the mask for the chip with a column with round pillars.

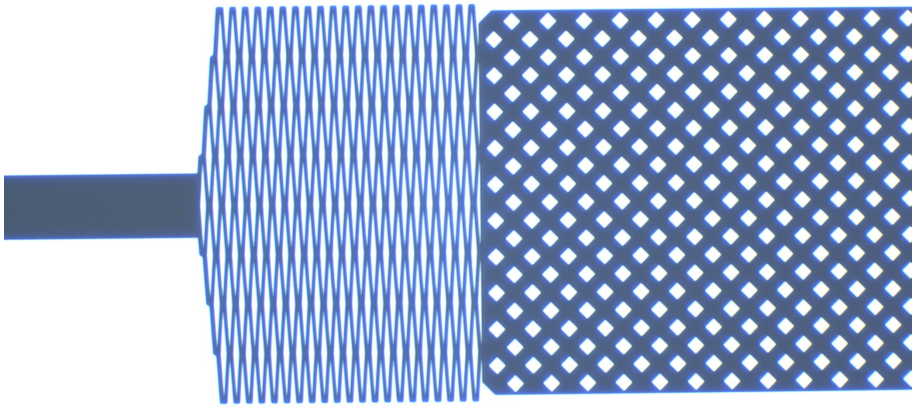

(a) Inlet of the column.

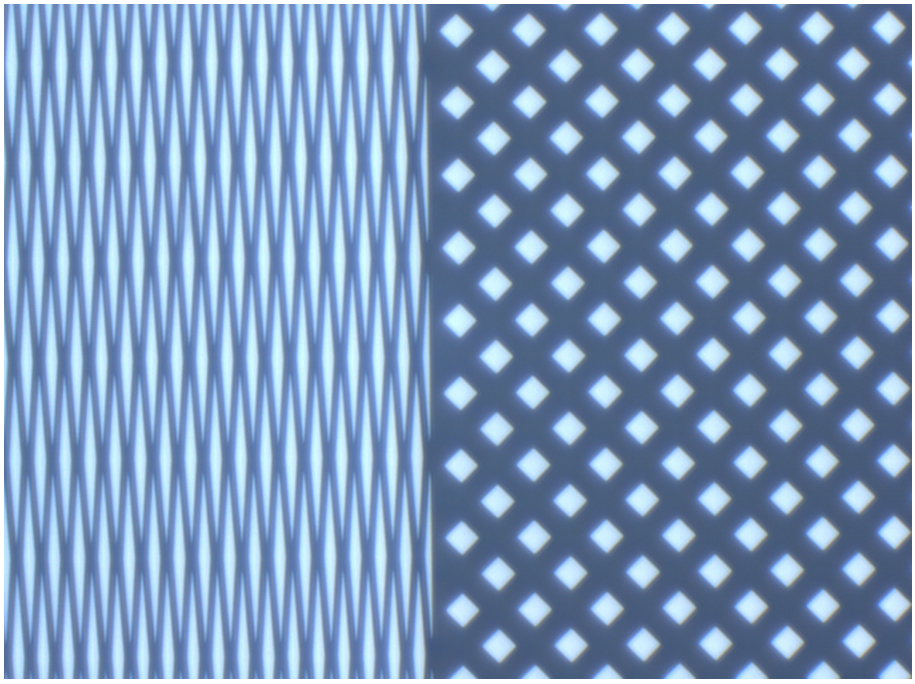

(b) Design error.

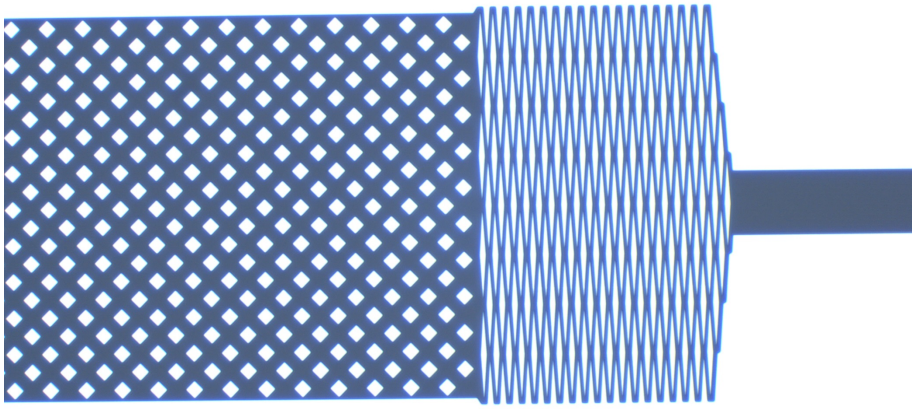

(c) Outlet of the column.

Figure F.3: Microscope images of the mask for the chip with a column with square pillars.

Appendix G

Fabrication related results

The results of several fabrication steps are combined in this appendix.

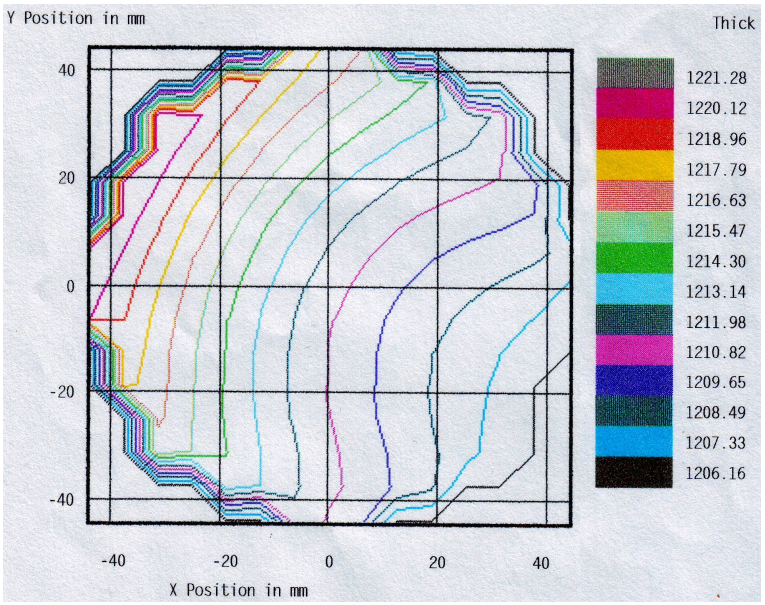

Figure G.1: Ellipsometry results of the wet oxidized Si made with a full wafer scan.

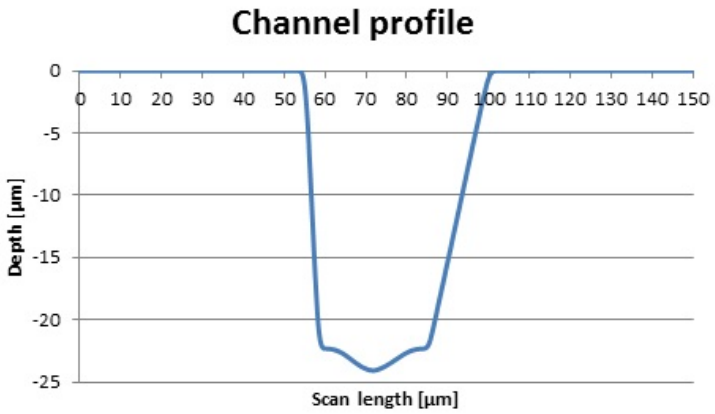

Figure G.2: Channel profile as measured with the Veeco Dektak profiler.

The small dip (making the maximal depth 24.07 μm) in figure G.2, in the middle of the etched channel is due to the used BOSCH recipe (B-HARS)[180]. The sloped sidewalls are due to the stylus radius and scan speed, as can be seen by the SEM images below.

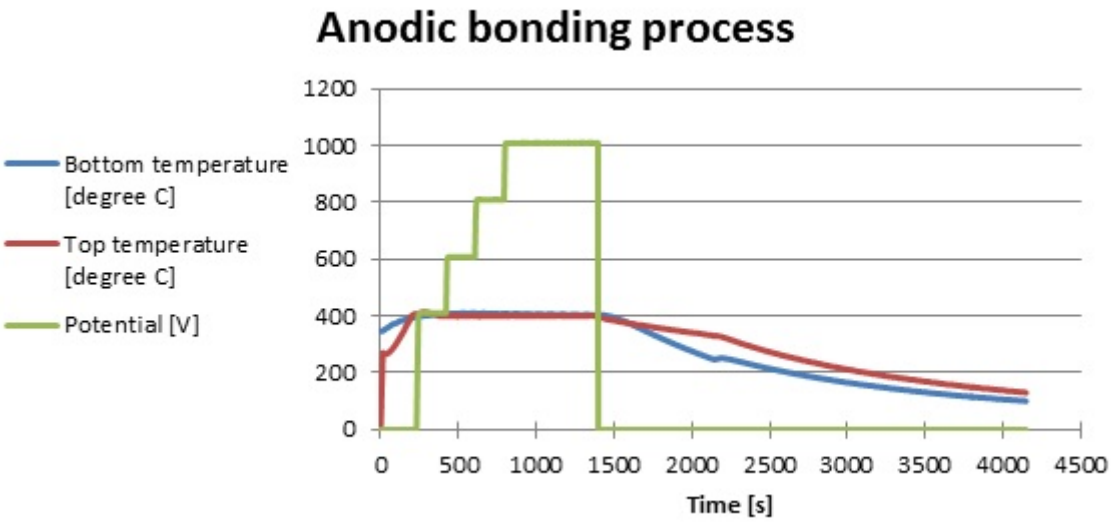

Figure G.3: Anodic bonding recipe.

Appendix H

Detailed SEM images of the scallops on the pillars

All the SEM images in this appendix are made with the FEI Sirion HR-SEM (Hillsboro, OR, United States), which is shown in figure H.1.

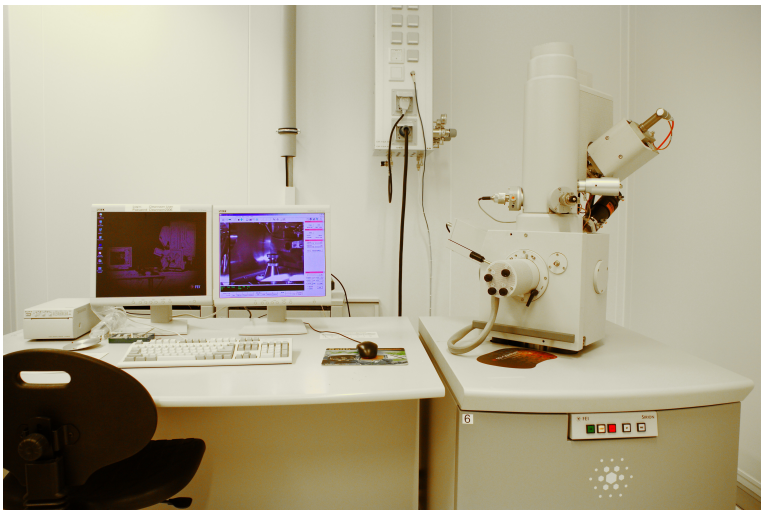

Figure H.1: FEI Sirion HR-SEM.

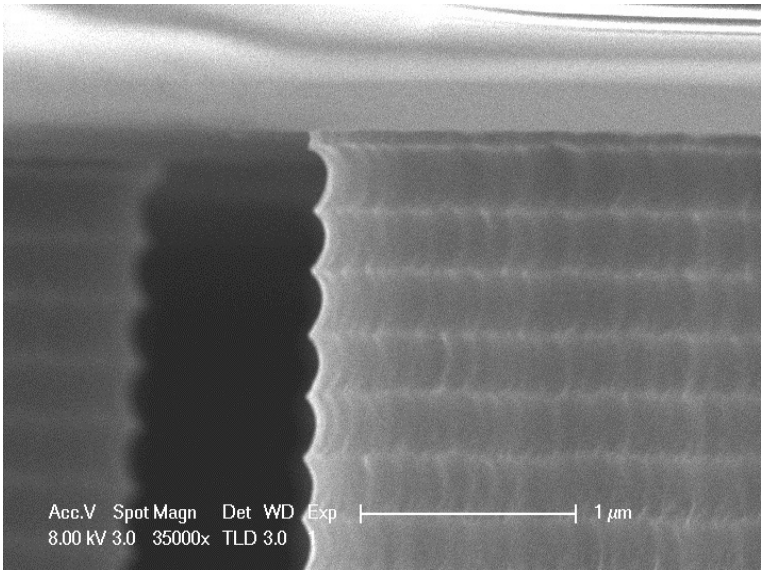

Figure H.2: SEM image of round pillar at depth is 0 μm.

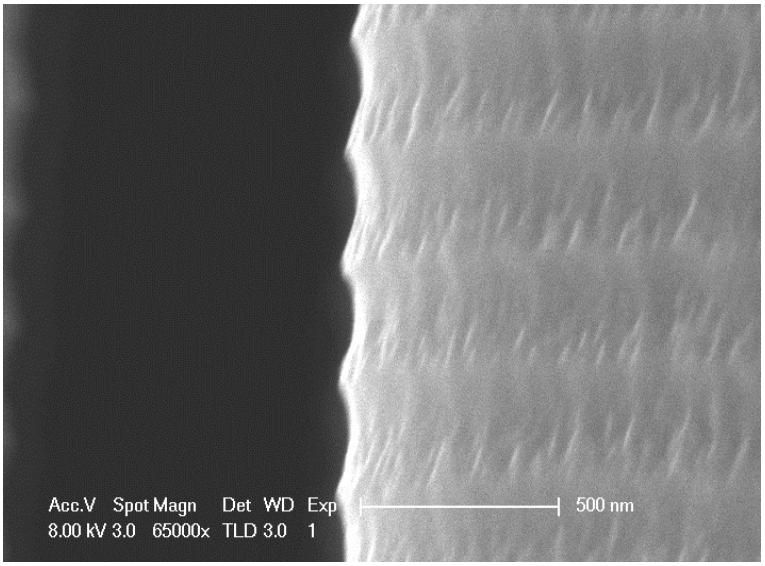

Figure H.3: SEM image of round pillar at depth is $\sim$ 4.5 μm.

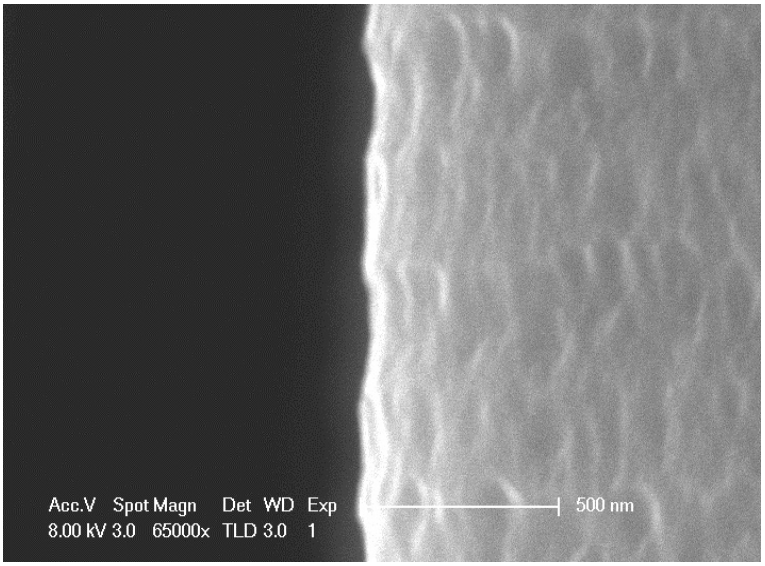

Figure H.4: SEM image of round pillar at depth is $\sim$ 10.5 μm.

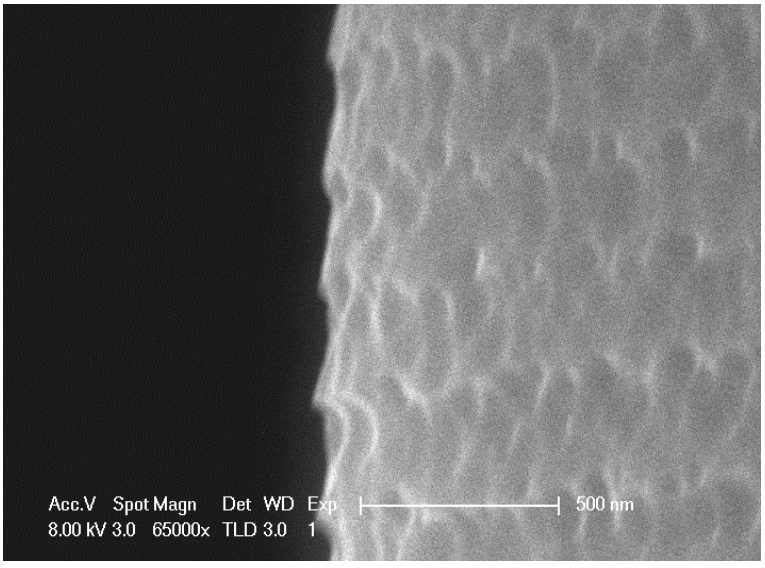

Figure H.5: SEM image of round pillar at depth is $\sim$ 16.5 μm.

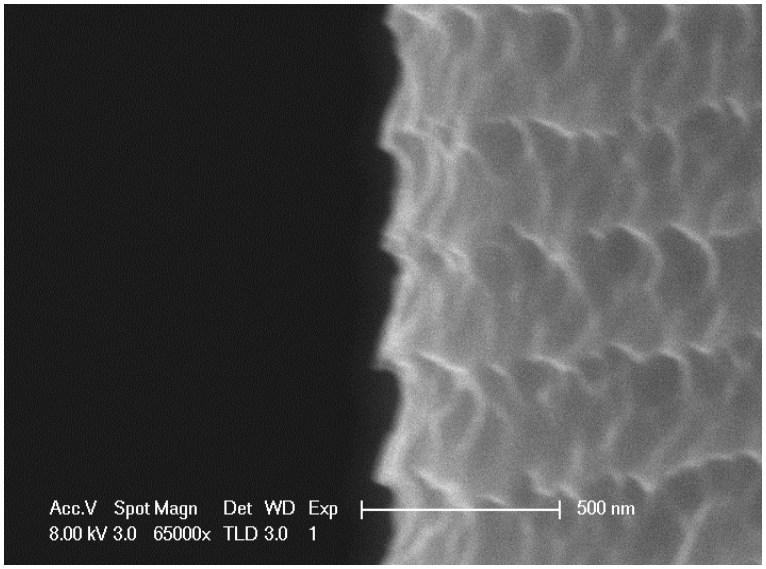

Figure H.6: SEM image of round pillar at depth is $\sim$ 20.5 μm.

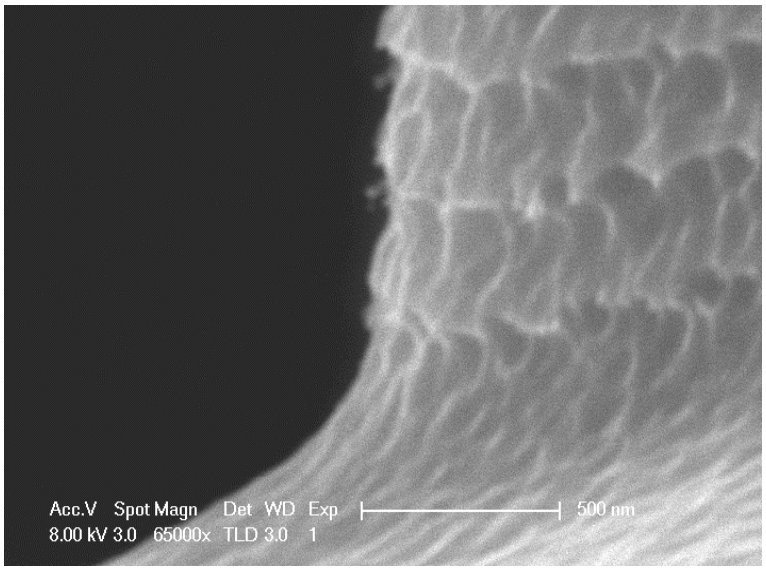

Figure H.7: SEM image of round pillar at depth is 25 μm.

Appendix I

Graphs of the XPS results

In the following appendix, the results of the XPS measurements can be found. All used substrates are 1.5×1.5 cm^2 <100> silicon substrates with native oxide. The substrates are measured with the PHI Quantera SXM-XPS system (Chanhassen, MN, United States).

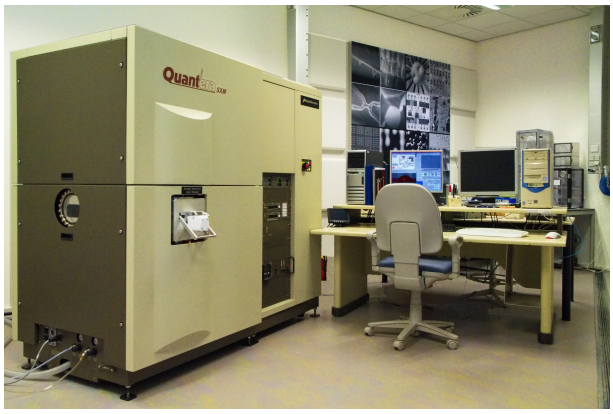

Figure I.1: The PHI Quantera SXM-XPS. Picture taken from reference 290.

I.1 Chitosan functionalization

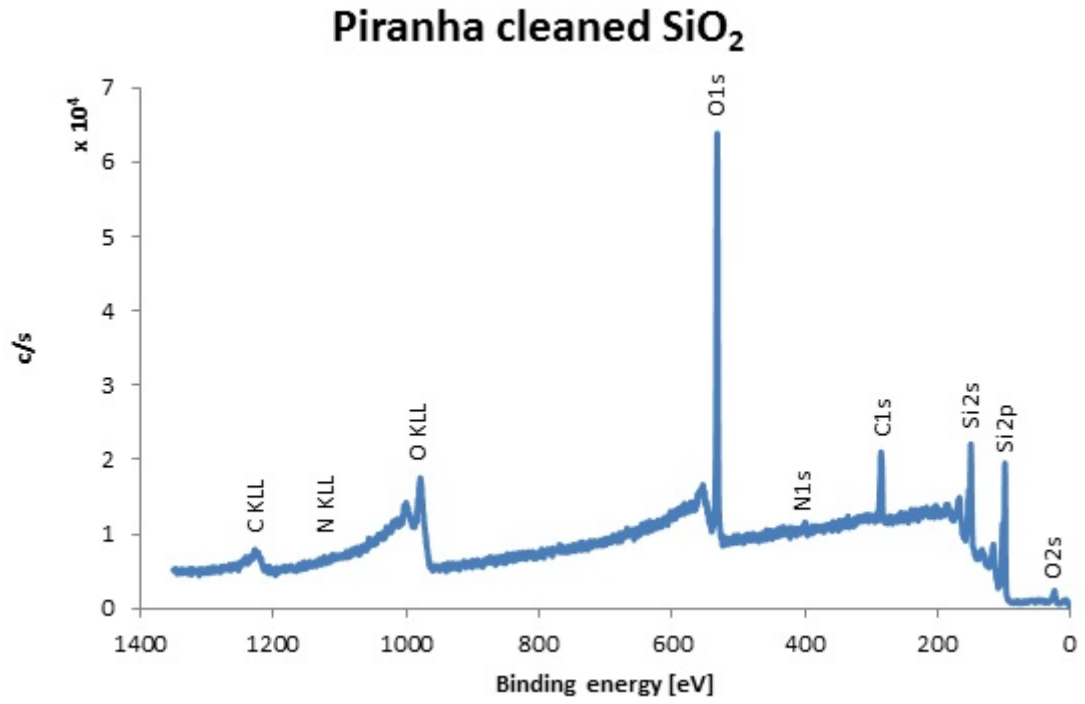

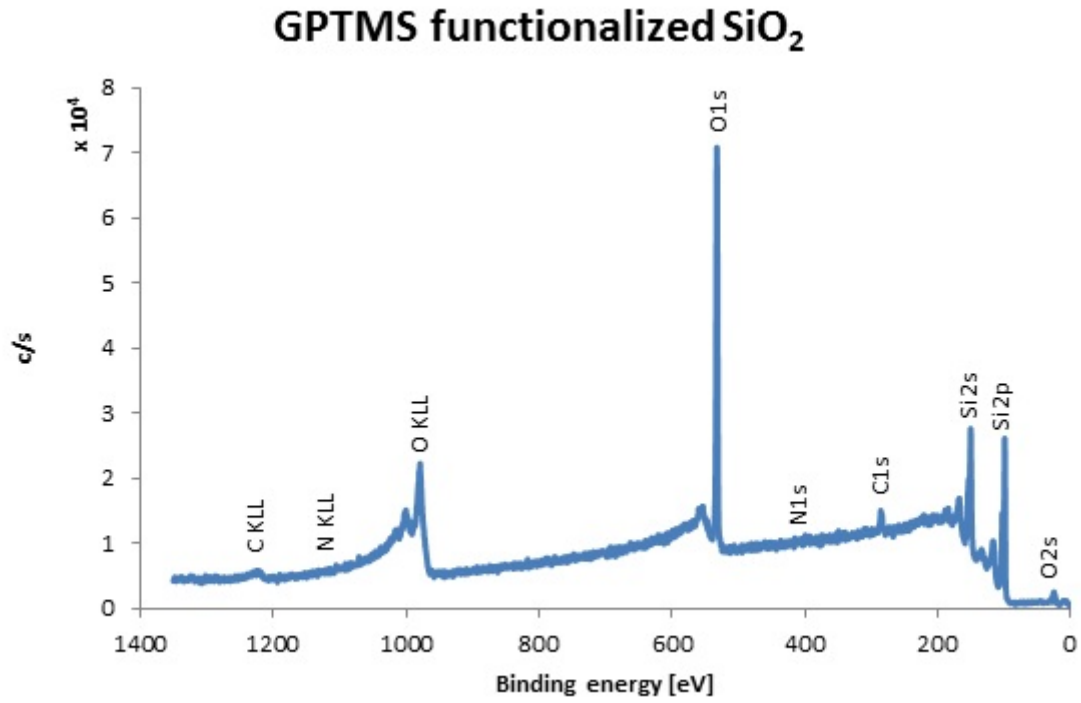
GPTMS functionalized SiO2
x 10^4
c/s
8
7
6
5
4
3
2
1
0
O1s
Si2s
Si2p
O KLL
C1s
C KLL
N KLL
N1s
O2s
1400
1200
1000
800
600
400
200
0
Binding energy [eV]

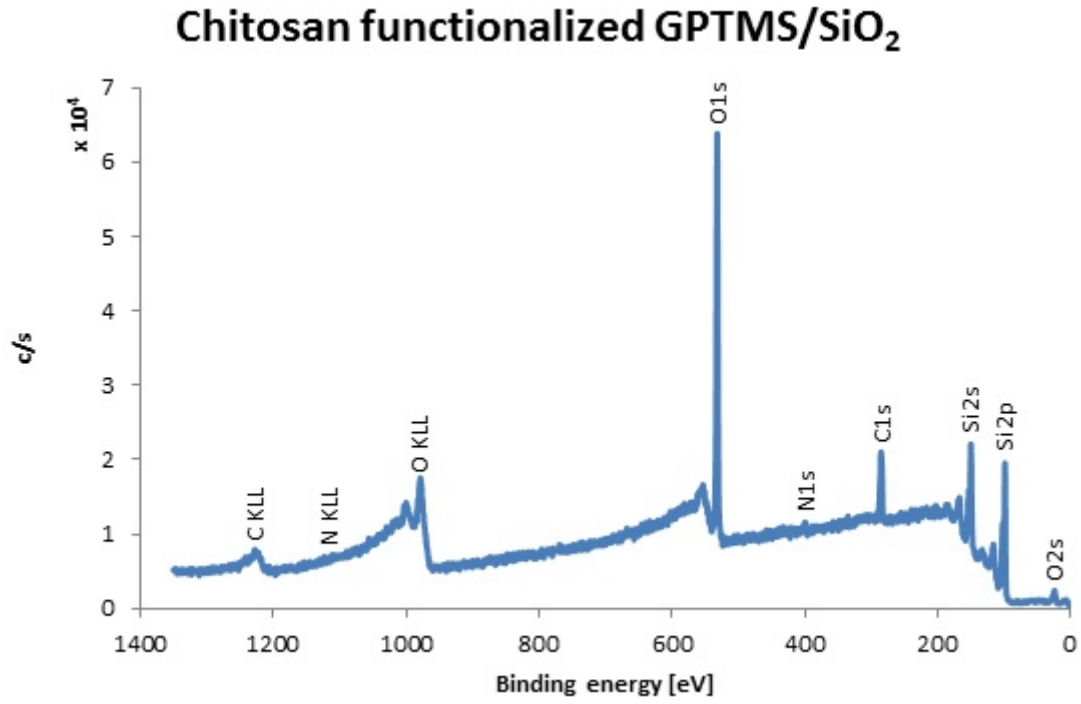
Chitosan functionalized GPTMS/SiO2
x 10^4
c/s
7
6
5
4
3
2
1
0
O1s
Si2s
Si2p
O KLL
C1s
C KLL
N KLL
N1s
O2s
1400
1200
1000
800
600
400
200
0
Binding energy [eV]

I.2 APTES functionalization

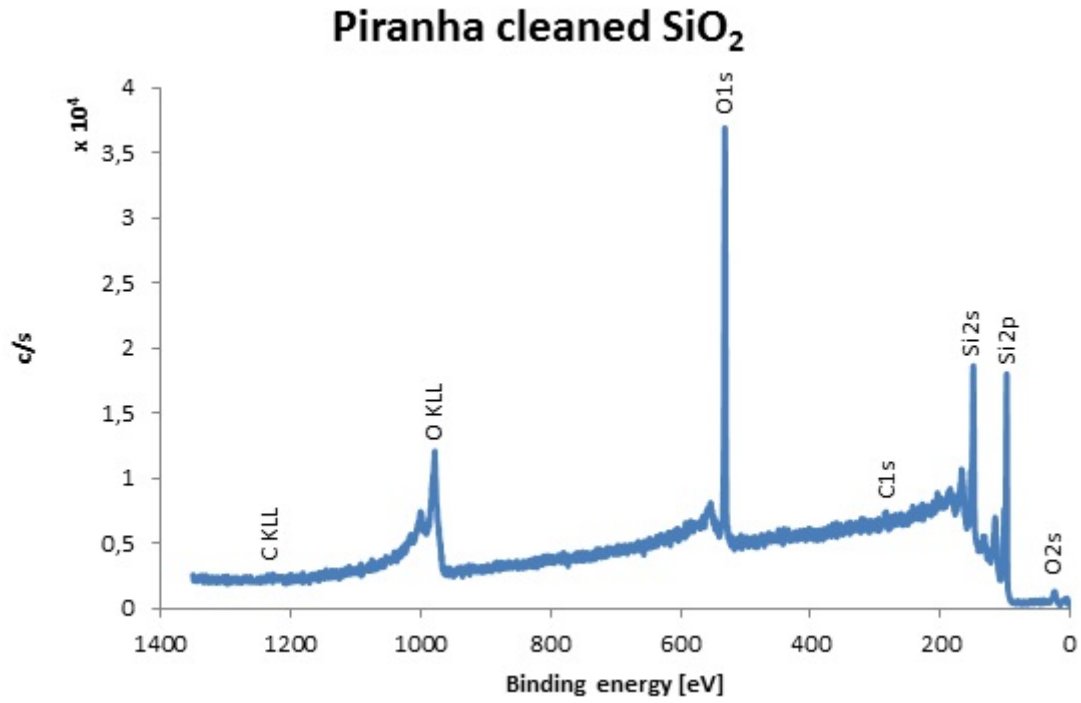

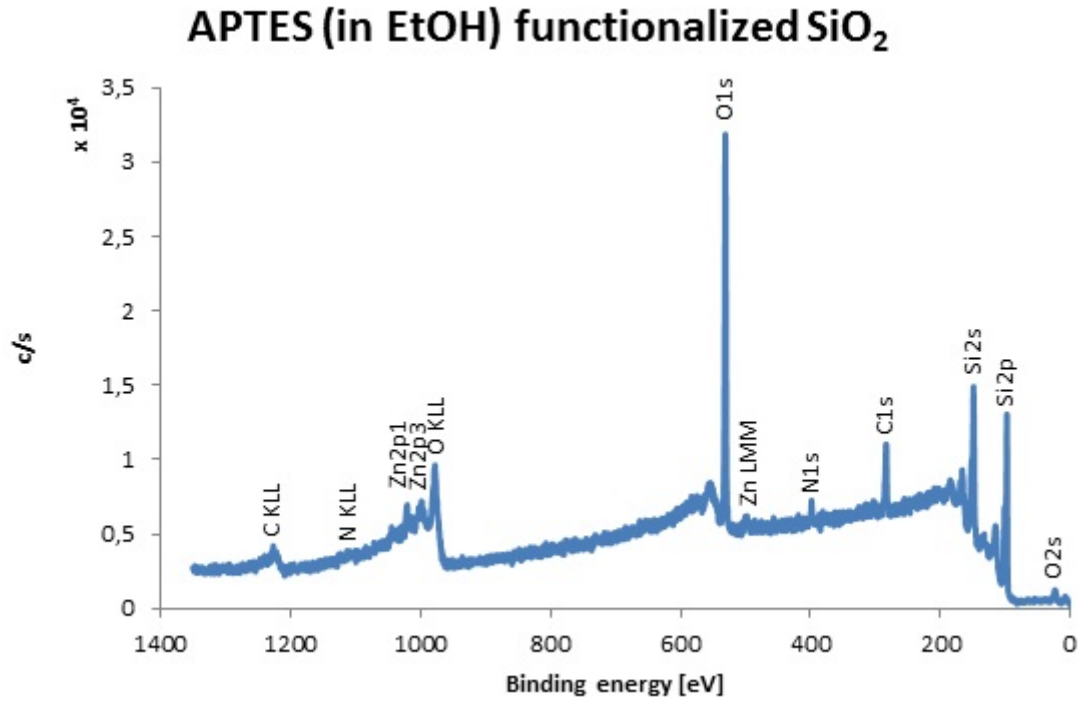

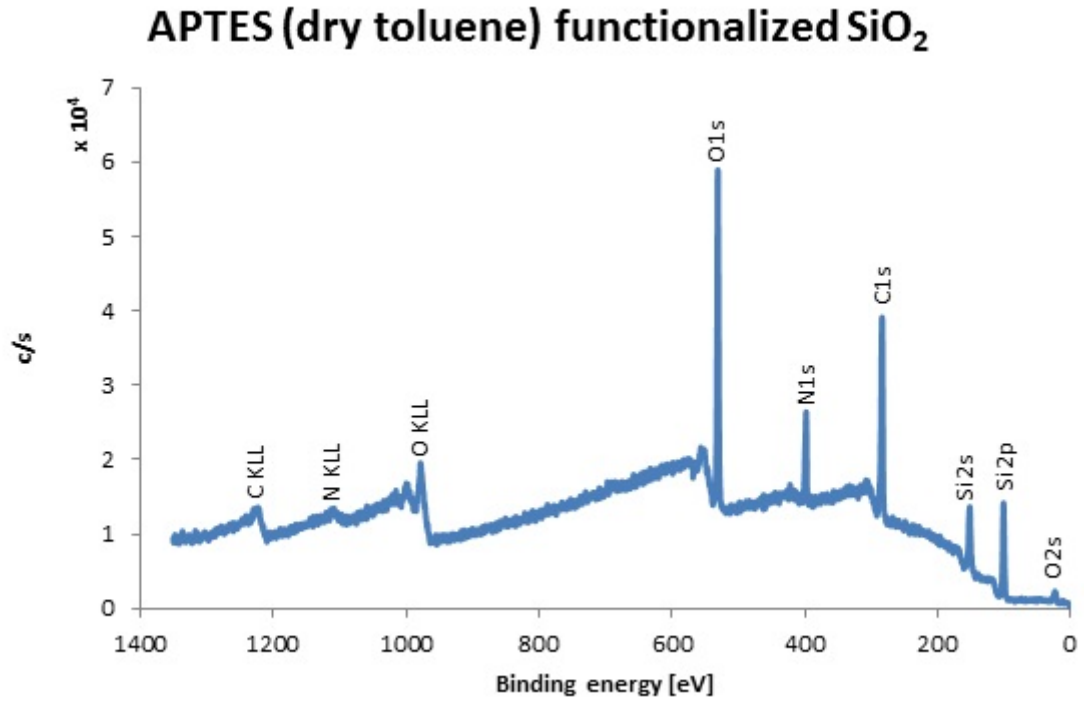
APTES (dry toluene) functionalized SiO2
c/s
x 10⁴
7
6
5
4
3
2
1
0
C KLL
N KLL
O KLL
O1s
N1s
C1s
Si2s
Si2p
O2s
1400
1200
1000
800
600
400
200
0
Binding energy [eV]

Appendix J

Contact angle measurement results

All measurements are done with a DataPhysics OCA 15plus contact angle system (Filderstadt, Germany) in sessile drop operation, see figure J.1.

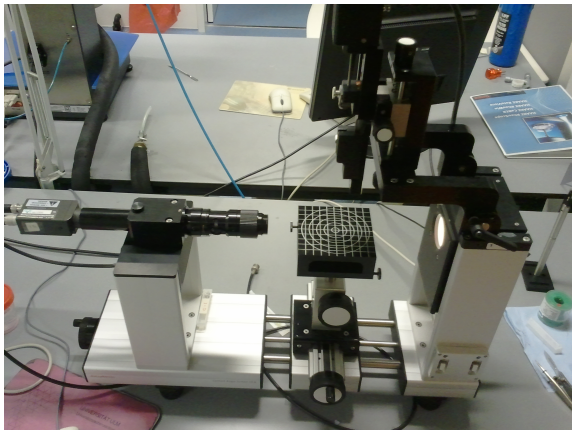

Figure J.1: The DataPhysics OCA 15plus contact angle system.

J.1 Functionalization

Without functionalization	**Photograph**
Native SiO_2	
Chitosan functionalization	
Piranha cleaned native SiO_2, with carbon contamination according to XPS	

GPTMS functionalized native SiO_2	
Chitosan functionalized GPTMS/native SiO_2	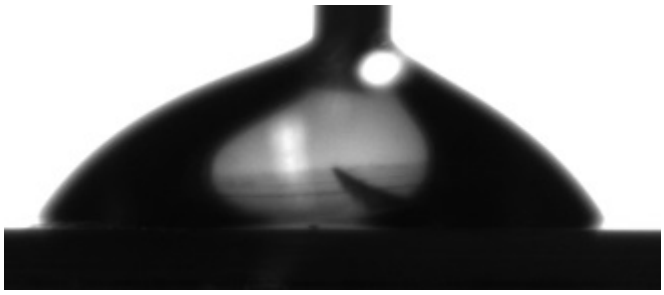
APTES functionalization	
Piranha cleaned native SiO_2	
APTES functionalized native SiO_2, in EtOH	
APTES functionalized native SiO_2, in dry toluene	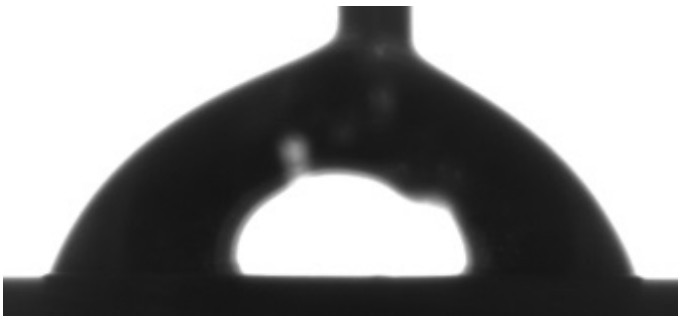

J.2 Cleaning and activation

Cleaning and activation step	Photograph
Native SiO_2	
Piranha 3:1	
Piranha 2:1	
Piranha 1:1	
Piranha 0:1	
Piranha 1:2	
Oxygen plasma	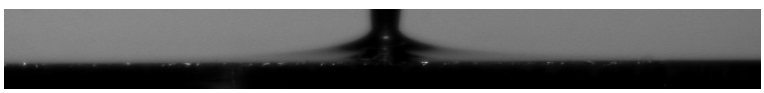

Table J.1: Contact angle measurement results of cleaned substrates. All ratios are 95.0-98.0% H_2SO_4 (Sigma-Aldrich, ACS reagent):31% H_2O_2 (Q-BASF, VLSIn Selectipur). All values are in degrees.

Cleaning mixture	**Static contact angle (θ_{stat})**	**Advancing and reducing contact angle (θ_{adv} / θ_{red})**
Native SiO_2	38.6 $\pm$ 1.6 (n=2)	42.0 $\pm$ 2.8 (n=5) 17.1 $\pm$ 0.1 (n=4)
3:1	19.4 $\pm$ 1.4 (n=6)	17.6 $\pm$ 3.2 (n=12) 5.1 $\pm$ 2.2 (n=12)
2:1	15.5 $\pm$ 0.9 (n=6)	17.6 $\pm$ 1.4 (n=15) 3.9 $\pm$ 1.7 (n=15)
1:1	12.1 $\pm$ 2.2 (n=6)	15.3 $\pm$ 1.0 (n=15) 3.6 $\pm$ 0.6 (n=15)
0:1	24.4 $\pm$ 1.4 (n=6)	24.7 $\pm$ 1.2 (n=15) 8.3 $\pm$ 0.9 (n=15)
1:2	21.5 $\pm$ 2.1 (n=6)	22.4 $\pm$ 2.7 (n=15) 36.9 $\pm$ 0.9 (n=15)
Oxygen plasma	Too low, can't find dimensions	Too low, can't find dimensions

Appendix K

Extraction results

Below are the graphs of the extraction tests with <100> DSP Si strips with a total extraction area of 88 mm^2. The procedure and a table with the summary of these tests can be found in chapter 4.

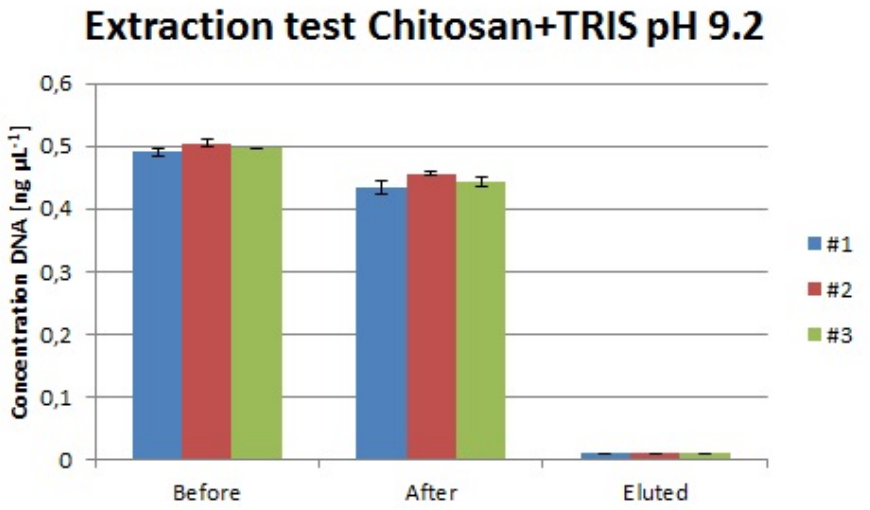

Figure K.1: Extraction test with chitosan coating and TRIS pH 9.2.

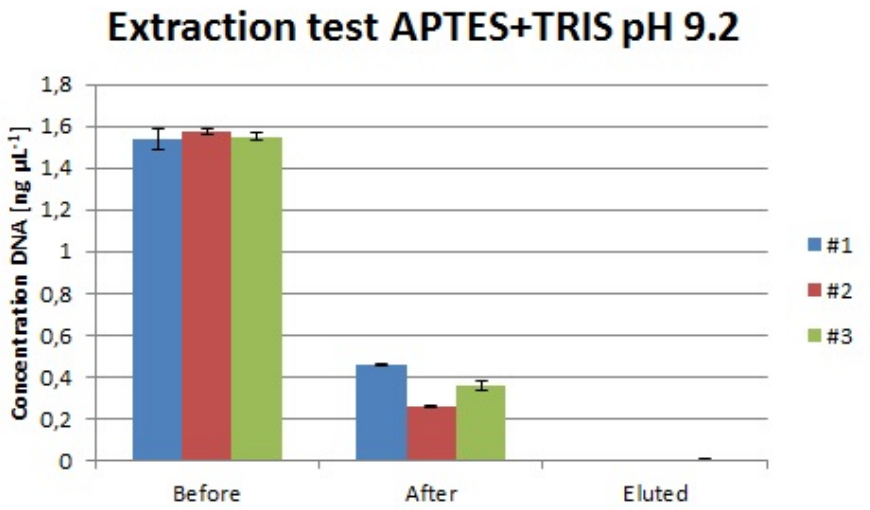

Figure K.2: Extraction test with APTES coating and TRIS pH 9.2.

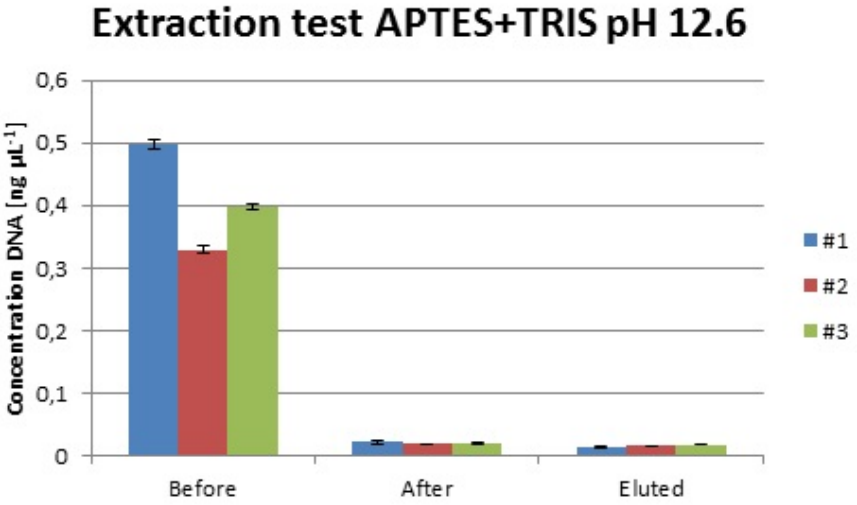

Figure K.3: Extraction test with APTES coating and TRIS pH 12.6.

Appendix L

List of activities

L.1 Clean room courses

Course	Description
Nanolab Introduction to Clean room Equipment (NICE) workshop	Basics of clean room environment and photolithoraphy
Vacuum course	Introduction into vacuum technologie (pumps and meters)
Piranha	Learning to prepare and clean with piranha (3:1 96% H_2SO_4:31% H_2O_2)
Ellipsometry	Learning to use the Woollam M-2000UI ellipsometer (Lincoln, NE, United States)
Dektak	Learning to use the Veeco Dektak profiler (Plainview, NY, United States)
Adixen DE	Learning to use the Alcatel Adixen AMS100 DE (Annecy Cedex, France)
Adixen SE	Learning to use the Alcatel Adixen AMS100 SE (Annecy Cedex, France)
Sputteren	Learning to use the homebuild sputter equipment “Sputterke” (TCO, Enschede, The Netherlands)
SPTS	Learning to use the SPTS “Pegasus” DRIE etching tool
IBE/RIBE	Learning to use the Oxford Instruments Ionfab 300Plus RIBE (Abingdon, United Kingdom)
SEM1	Learning to use the Jeol JSM 5610 SEM (Tokyo, Japan)
SEM2	Learning to use the FEI Sirion HR-SEM (Hillsboro, OR, United States)
Maximus	Learning to use the SSE Maximus 804 lithography robot (Radolfzell, Germany)
Plasma Tepla1	Learning to use the Tepla PS300 semi-auto plasma cleaner (Kirchheim, Germany)
Plasma Tepla2	Learning to use the Tepla PS300E plasma cleaner (Kirchheim, Germany)
Dicing	Learning to use the Disco DAD 321 (Tokyo, Japan)
Anodic bonding	Learning to use EVG EV-501 anodic bonder (St. Florian am Inn, Austria)
Evening permission	Learning the safety rules and protocols for the evening access of the clean room

L.2 Presentations

Date	Location	Title
10-Dec-2013	Saxion, Deventer (NL)	Persoonlijke loopbaan
10-Dec-2013	Saxion, Deventer (NL)	Nanotechnologie en lab-on-a-chips
24-Jun-2014	AkzoNobel, Deventer (NL)	Microreactors and lab-on-a-chip devices
16-Jul-2014	University of Twente, Enschede (NL)	A plug based micro solid phase extraction (μSPE) microfluidic chip for the isolation and purification of DNA